INVESTIGATIONS OF STAR FORMATION AND IONIZING RADIATION ACROSS TIME AND SPATIAL SCALES

by

Brian Welch

A dissertation submitted to Johns Hopkins University

in conformity with the requirements for the degree of

Doctor of Philosophy

Baltimore, Maryland

May, 2022

Abstract

This thesis explores a broad range of spatial scales across a broad range of times throughout the history of the universe, with the goal of improving our understanding of star formation and the origin of ionizing radiation across these broad scales. In the nearby universe, we can examine star formation on galactic scales and at the level of individual stars. However, in the distant universe, we are often limited to only the larger galactic scales due to finite telescope resolution. However, with gravitational lensing, we can reveal similarly small scales in distant galaxies. In my work, I examined lensed galaxy substructure at redshifts $z > 6$ down to parsec scales, and in one case I determined that an individual star is observed at $z = 6$. These observations allow for detailed study of the structures of these distant galaxies, as well as the composition of a star within the first billion years of the universe. On the larger scales, galaxy clusters typically contain little active star formation. However, I examined diffuse ultraviolet radiation around massive clusters and found an excess, which could be explained by ongoing star formation in the intracluster medium. Together, these studies contribute to our understanding of star formation on multiple scales. Additionally, young, UV-bright stars are key contributors to the ionizing radiation that drove the transition from neutral

to ionized hydrogen in the early universe, and contributes to continuing that ionized state today. The studies presented herein again offer a multi-scale perspective on the sources of ionizing UV light. The small scale star formation in distant galaxies can help determine how ionizing photons are created and escape from these galaxies into the intergalactic medium, where they contribute to reionization. Meanwhile, studying the UV emission from galaxy clusters provides an additional source to help make sense of the UV background light, which, at higher energies, contributes to maintaining the ionized state of the intergalactic medium.

Thesis Committee

Primary Readers

Stephan McCandliss (Co-Advisor)
Research Professor
Department of Physics and Astronomy
Johns Hopkins Krieger School of Arts and Sciences

Dan Coe (Co-Advisor)
Astronomer
Space Telescope Science Institute

Petar Maksimovic
Professor
Department of Physics and Astronomy
Johns Hopkins Krieger School of Arts and Sciences

Sarah Hörst
Associate Professor
Department of Earth and Planetary Sciences
Johns Hopkins Krieger School of Arts and Sciences

A. Shoji Hall
Assistant Professor
Department of Materials Science and Engineering
Johns Hopkins Whiting School of Engineering

Acknowledgments

Thanks in particular to my wife April, for supporting me through this whole process.

Table of Contents

List of Tables

List of Figures

Chapter 1

Introduction

"An astrophysicist is a collection of cosmic dust that woke up and starting thinking about itself" – Anonymous

1.1 The Beginning

The commonly accepted theory for the formation of our Universe is the Big Bang, in which Things As We Know Them went from being packed into an incomprehensibly small space to a incomprehensibly large one all in an incomprehensibly small amount of time. The exact mechanism for this sudden expansion (known generally as inflation) is somewhat debated, but luckily it does not make too much of a difference in our case. What matters here is that the Universe began. This nascent universe was a hot place, so hot that matter was dissolved into its most fundamental particles, including quarks, electrons, and neutrinos. As the universe continued expanding after the inflationary epoch, it cooled, and these fundamental particles began to coalesce, first into protons and neutrons, and eventually into light elements. These elements

were mostly hydrogen and helium, though some lithium formed as well. At the time hydrogen first formed, the Universe was still quite hot and dense. The newly formed hydrogen therefore kept running into high energy photons, which knocked electrons away from the proton of the hydrogen nucleus and kept it as ionized hydrogen (HII). As the universe kept expanding, eventually the matter was able to spread out enough to allow the remnant photons from the Big Bang to move freely, without continually bumping into the hydrogen and ionizing it. The light would become the Cosmic Microwave Background (CMB). The result of the CMB freezing out was that ionized HII was able to finally hang on to its long-lost electron buddies and recombine to form neutral hydrogen (HI).

On the largest scales, this neutral hydrogen universe is pretty boring. It is homogeneous and isotropic, so each large patch is almost identical to every other large patch. At smaller scales however, there are more fluctuations. At first, they are relatively small differences, slight increases in matter density at some points, and slight decreases in density at others. Over time, gravity pulls more and more hydrogen gas towards these overdensities, making them even more dense and even more gravitationally attractive. Eventually, these increasingly dense clouds of hydrogen begin to collapse - the force of gravity overwhelms the increasing pressure that comes with increased density, and crushes more and more hydrogen into a smaller and smaller space. This leads to massive amounts of heat being generated. Once the collapsing ball of gas gets hot enough, it ignites, setting off an explosive chain reaction of hydrogen atoms fusing together into helium. While this atomic fusion reaction tries to

blow the ball of hydrogen apart, the force of gravity remains strong enough to squeeze the ball together, sustaining even more hydrogen fusion. This giant ball of burning gas is one of the first stars, lighting up the universe with its glow.

From here, the universe begins to evolve into its familiar form, full of beautiful spiral galaxies, each filled with nigh uncountable stars, and planets like the one we are clinging to currently. As this evolution occurs, the universe continues to expand, constantly increasing the separations between distant galaxies. This continual expansion provides a convenient way of measuring distances today, as the light from more distant galaxies is stretched along its journey to our telescopes. As light travels through expanding space, its wavelength is stretched, resulting in redder, longer-wavelength light. This process, known as cosmological redshift, is directly related to the distance light from an object has traveled, providing an easily measurable proxy for vast distances. The higher the redshift, the more distant the object in question.

In the remainder of this introduction chapter, I will discuss our current understanding of the formation of galaxies, and what properties they tend to have within the first billion years of the evolution of the Universe. I will then examine the contribution of young, UV bright stars in these galaxies to the reionization of the universe. I next discuss the growth of clusters of galaxies, and the effects the dense cluster environment has on galaxies and their ability to form stars. Finally, I conclude with a brief discussion of gravitational lensing and the power it has to reveal distant objects that would otherwise remain out of reach of our most powerful telescopes.

1.2 And then there was light: formation of the first stars and galaxies

As mentioned above, the first stars formed when clouds of hydrogen gas collapse under their own gravitational pull (see Bromm and Larson, 2004, for a comprehensive review). This process mirrors the way stars form in the local universe, however there is one critical difference: the existence (or lack thereof) of metals. Astronomers refer to anything heavier than Hydrogen and Helium as metals, and of these astro-metals, only small amounts of lithium were produced in the Big Bang. The first generation of stars, known as Population III stars, therefore formed out of pristine hydrogen gas. The largest side effect of this composition is that hydrogen is not particularly efficient at cooling. As a cloud of gas collapses, it tends to heat up. In local star formation, the presence of metals and dust can efficiently draw this heat away from the center of the cloud, which has the effect of fragmenting the cloud. This results in the formation of smaller stars, with typical masses similar to that of our Sun. In the early universe, the lack of these metals and dust have the effect of producing much larger stars. Typical masses for Population III stars are estimated to be anywhere from a few $\times 10 M_\odot$ to as high as $1000 M_\odot$ (Hosokawa et al., 2016). Meanwhile, some models suggest supermassive Pop III stars can form via accretion from their surrounding gas cloud, resulting in stars as massive as $\sim 10^4 M_\odot$ (Haemmerlé et al., 2018). The high masses of these stars result in their having short lifetimes, as more massive stars tend to extinguish themselves sooner than smaller stars. The exact fate of the Pop III stars depends on their initial mass. Stars with masses below $\sim 140 M_\odot$

will eventually explode as core-collapse supernovae, spreading some of their newly formed metals across the universe while capturing others in a remnant black hole. However, for more massive stars in the range $140 \leq M/M_{\odot} \leq 230$, a pair-instability supernova will occur, completely disrupting the original star and spreading all of its newly formed metals out across space. These explosions are predicted to trigger the second generation of star formation, with slightly enriched stars known as Population II stars forming out of the ashes of these primordial explosions (Chiaki, Susa, and Hirano, 2018). Most stars above $\sim 230 M_{\odot}$ are expected to collapse directly into black holes (Heger et al., 2003), however recent simulations predict that supermassive stars may again be able to explode in supernovae (Nagele et al., 2020).

Thus far, no conclusive observational evidence of Population III stars has been presented. Several studies have reported candidate Pop III stellar populations in distant galaxies (e.g., Vanzella et al., 2020; Pelliccia et al., 2021). However, these candidates have yet to be confirmed. The James Webb Space Telescope (JWST) is expected to shed additional light on the first generation of stars. Besides searching for evidence of Pop III stellar populations in galaxies, it has been suggested that JWST may be able to discover individual Pop III stars with the help of gravitational lensing, in which massive foreground objects (lenses) magnify distant background objects (sources). If the lens and source are properly aligned, extreme magnifications can be reached that could reveal individual Pop III stars in the early universe (Windhorst et al., 2018).

In our modern universe, stars are not the only structures we see. Most stars reside within larger galaxies, such as our home galaxy the Milky Way. How

exactly the first galaxies formed is an active area of research. Models of Pop III stars suggest that they tend to form as individual stars within their halos (Bromm and Larson, 2004). Taking the definition of a galaxy as a collection of stars and gas held together by a dark matter potential well, these first stars do not simultaneously qualify as the first galaxies. However, simulations of second-generation, slightly enriched Population II stars have suggested that this enrichment leads to fragmentation of larger gas clouds, and thus the formation of clusters of stars within early dark matter halos (Chiaki, Susa, and Hirano, 2018). These then become the first objects to meet our definition of the first galaxies.

The exact formation mechanism is still debated in part due to the lack of observations of these first galaxies. Thus far, we have observed out to redshift $z \sim 11$ (Coe et al., 2013; Oesch et al., 2016), with two additional candidates recently discovered at $z \sim 12 - 13$ (Harikane et al., 2021). While these are quite distant, it is expected that these records will be eclipsed with JWST, as deeper observations in the infrared are expected to discover galaxies out to higher redshifts. While the highest observable redshift may be a moving target, the observations of galaxies at $z > 6$, within the first billion years following the Big Bang, can give us some insight into the structures of these earliest galaxies. Simulations have shown that the dark matter halos of high redshift galaxies tend to be less massive than galaxies at lower redshift (e.g., Pillepich et al., 2018). Additionally, analysis of luminosity functions, which measure the number of galaxies at a given luminosity, have shown that characteristic luminosities (L^*) tend to decrease with increasing redshift, and the faint-end

slope α tends to decrease as well (Finkelstein, 2016). These trends indicate that the typical galaxy at high redshift is smaller than the galaxies seen in the local universe, and there is a greater abundance of dwarf galaxies in the early stages of galaxy formation. Additionally, observations at $z \sim 2$ revealed that these galaxies have clumpy structures (Elmegreen and Elmegreen, 2005; Elmegreen et al., 2007; Elmegreen et al., 2009), and observations of gravitationally lensed galaxies found that these clumps reach down to the scale of local star clusters (Livermore et al., 2015; Johnson et al., 2017; Zick et al., 2020). Other studies have found small clump structures in galaxies as far back as $z \sim 6$ (Vanzella et al., 2019). Besides exhibiting clumpier morphologies, high redshift galaxies tend to have greater star formation rates (SFR) per unit stellar mass (specific star formation rate, sSFR) (Salmon et al., 2015). This implies that these galaxies are more efficient at forming stars than local galaxies. However, the overall star formation activity in galaxies peaks later, at $z \sim 2$ (Behroozi, Wechsler, and Conroy, 2013).

1.3 The End of Neutrality

As these early galaxies form and grow, they continue forming stars as more gas falls on to the galaxy from the surrounding medium. These stars then flood the surrounding space with their light. More massive stars, which tend to be short lived and thus only visible in galaxies that have recently undergone periods of star formation, shine brightest in the ultraviolet (UV). As a result of the large population of UV-bright stars in galaxies, the previously neutral hydrogen is once again bombarded by photons with enough energy to kick

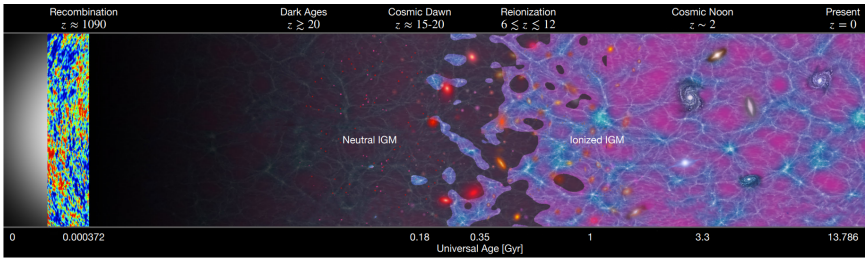

Figure 1.1: Depiction of the evolution of the Universe, from the Big Bang to the modern day. As the universe expanded and cooled after the Big Bang, ionized hydrogen recombined with electrons to form neutral hydrogen gas, which persisted until the first stars began to form. Light from these stars began to photoionize the hydrogen gas. As galaxies began to form and stars continued shining, their light once again separated electrons from hydrogen nuclei, a process that lasted until about one billion years after the Big Bang in a time known as the Epoch of Reionization. Figure reprinted from Robertson, 2021.

out the single electron, re-ionizing the hydrogen gas. The time period where this occurs is know by the descriptive (albeit unimaginative) moniker of the Epoch of Reionization (EoR).

The exact beginning of the EoR is not precisely known. While the formation of the first stars at $z \sim 30$ leads to the first ionizing radiation to be seen since recombination, it is generally thought that the reionization era did not begin in earnest until later ($z \sim 12 - 15$). Measurements of the CMB can provide an estimate of the midpoint of the reionization process, which is currently measured at $z = 7.7 \pm 0.7$ (Planck Collaboration et al., 2020). While establishing the beginning of the EoR has proven difficult, the end of the era has been well established at $z \sim 6$. At lower redshift, observations of galaxies show minimal intergalactic hydrogen absorption, indicating that the hydrogen gas is ionized (Ouchi et al., 2010).

The reionization process is not homogeneous and isotropic, but rather proceeds in a clumpy manner. Early on, UV-bright starlight tends to encounter

optically thick clouds of neutral hydrogen quickly. As more starlight illuminates these hydrogen clouds, more and more of the gas becomes ionized. Bubbles of ionized gas begin to form around individual stars, and as these bubbles grow they merge with neighboring bubbles. Eventually, the starlight creates ionized bubbles large enough to allow photons to escape from the galaxy and into the neutral intergalactic medium (IGM). As enough light escapes from the largest, brightest galaxies, it carves out larger ionized bubbles in the IGM, through which ionizing photons can travel freely. As time passes, these bubbles grow larger until they eventually encounter the bubbles of neighboring galaxies. Eventually, as enough bubbles begin to overlap, the Epoch of Reionization comes to a close as most of the hydrogen in the intergalactic medium is once again ionized.

The reionization scenario presented above assumes that the UV light from stars is the dominant contributor to the ionizing radiation. This assumption has been largely supported in recent studies, which find that the number of galaxies at high redshifts are capable of largely reionizing the universe on their own (see recent reviews by Finkelstein, 2016; Robertson, 2021). However, there are other potential sources of ionizing radiation that could play an important role in this process. For example, active galactic nuclei (AGN) powered by accreting supermassive black holes at the centers of galaxies have been proposed as alternative sources of ionizing radiation. However, studies of the number of AGN at high-z have found that they are subdominant, likely contributing $< 10\%$ of the ionizing photons at $z \sim 6$ (Kulkarni, Worseck, and Hennawi, 2019).

1.4 On to bigger and bigger things

The first galaxies continue to grow over time, accumulating matter via accretion as nearby gas falls into the gravitational potential well and via mergers with neighboring structures. In the early stages, the galaxies remain clumpy and irregular as their turbulent growth continues. Eventually, these galaxies will settle into the familiar disks that we see in nearby galaxies, as well as in our own Milky Way. In some cases, galaxies reside in even larger scale overdensities, and they begin to drift toward each other. As more and more galaxies, gas, and dark matter come together in these overdensities, they form structures known (again unimaginatively) as galaxy clusters. These galaxy clusters make up the largest, most massive gravitationally bound objects in the known universe (e.g. review by Kravtsov and Borgani, 2012).

The dense environments of galaxy clusters have significant impacts on their resident galaxies. The increased frequency of interactions disrupts the spiral structures of newly infalling galaxies, giving them an elliptical shape, while also disrupting the galaxies gas reserves and quenching star formation (Ellis et al., 1997; Stanford, Eisenhardt, and Dickinson, 1998). Additionally, as galaxies move through the dense intracluster medium, ram-pressure tends to siphon star-forming gas out of the galaxy (Gunn and Gott, 1972). These effects shut down further star formation, leading to galaxies that are full of old, red stars. In particular, this can be seen in older, nearer clusters, which tend to have older, redder stellar populations than younger, distant clusters (Butcher and Oemler, 1978; Butcher and Oemler, 1984).

Despite generally being "red and dead", clusters can sometimes still house

ongoing star formation. This is most evident in so-called cool-core clusters, which have relaxed enough to allow gas at their center to cool, fueling new star formation. This is generally observed most prominently in the brightest cluster galaxy (BCG), which resides in the center of the cluster (e.g., Hicks, Mushotzky, and Donahue, 2010). Finally, infalling galaxies can continue forming new stars for a time, and even begin periods of intense star formation as they first enter a cluster. These jellyfish galaxies, so named for the bright tendrils of stars that trail out behind them, have their gas reservoirs disrupted by Ram-pressure as they fall into the cluster, leading to short but intense starburst phases (Ebeling, Stephenson, and Edge, 2014).

1.5 Finding Wonderland through the looking glass

Astronomers see the universe through telescopes. Generally, the push to observe the universe in greater detail is facilitated by the building of ever larger and more technically impressive telescopes (often with terribly unimaginative names, such as the Very Large Telescope and its successor the Extremely Large Telescope). In some cases, these powerful telescopes can be supplemented with naturally occurring gravitational telescopes, giving us a more detailed look into the hearts of certain galaxies.

In General Relativity, the generally accepted theory of gravity (Einstein, 1916), massive objects warp the fabric of spacetime that surrounds them. Light then moves through this warped space on straight paths. However, a straight path through a curved space appears to an outside observer like a curved path. Thus, massive objects appear to bend light that passes within

their gravitational field. This process is referred to as gravitational lensing. Similar to light passing through a glass lens in a magnifying glass or refracting telescope, gravitational lensing has the effect of magnifying the lensed objects. However, unlike smooth glass lenses, gravitational lenses also distort and shear the lensed images.

There are three important ways in which this effect is observed. The first is weak gravitational lensing, in which the light from background objects passes through the lensing gravitational field where said field is weak. In this case, the lensed object is only slightly magnified and sheared. Weak lensing is not discussed further in this thesis.

The second case, which will be dealt with extensively herein, is strong gravitational lensing. In this case, light from the background object passes through the strong gravitational field of the lensing object. This requires proper alignment of the lensing object and lensed object, and the more precise the alignment the greater the amplitude of the lensing effect. In the limit of perfect alignment, where a background source is directly behind a spherically symmetric lens object, the background source can be stretched into a ring that appears to encircle the lens. This is known as an Einstein Ring, and its radius, known as the Einstein radius, is proportional to the mass of the lensing object. When background galaxies are less perfectly aligned, or when the lens is elliptical, they tend to form multiple images. As the name implies, the background object can be seen in multiple places on the sky. If you imagine moving a lensed source relative to the lens, as the source moves behind the lens, it first moves from being weakly lensed to appearing as multiple images.

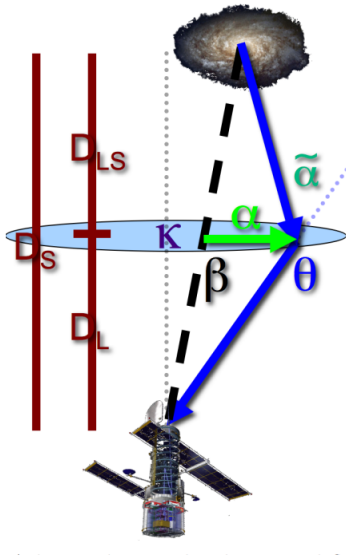

Figure 1.2: Illustration of the geometry of a strong lensing system. The angle by which light is deflected as it moves through the gravitational potential of the foreground lensing object can allow determinations of the lens object's mass. The lens also magnifies the background objects, which allows us to study distant objects in greater detail than would otherwise be possible. Figure reproduced from Coe et al., 2008.

As the source further aligns with the lens, the multiple images become more highly magnified, and thus more highly sheared. These begin to form arcs, where the image of the lensed object is stretched into a crescent shape. As the alignment further improves, these arcs get longer and more highly sheared, eventually merging in places.

Strong lensing allows astronomers to model the mass of the lensing object, typically either a single galaxy or a cluster of galaxies. The amount that a gravitational lens deflects light from background sources can be described by the lens equation, where the deflection angle is given by

$$\vec{\alpha}(\vec{\theta}) = \vec{\theta} - \vec{\beta} \tag{1.1}$$

where $\vec{\theta}$ is the observed position, and $\vec{\beta}$ is the true position on the sky. From the deflection angle, the surface mass density κ and the shear γ (the amount by which background objects appear elongated) can be calculated via the Jacobian of the lens equation. The magnification μ is then given as

$$1/\mu = (1-\kappa)^2 - \gamma^2. \tag{1.2}$$

In modern lensing analysis, we utilize computer codes to solve the lens equation given the observed positions of multiply-imaged lensed objects. In general, the more multiple image constraints that can be found, and the better their redshifts are known, the more accurate the lens model can be.

The third subcategory of gravitational lensing is known as microlensing. Microlensing occurs when two (astronomically) small objects align, and the observed brightness of the background object (typically a star) is temporarily boosted by the foreground object. This technique has many applications, including the the discovery of dark, massive objects such as black holes. When combined with strong lensing, microlensing can also assist in the detection of individual stars in distant lensed galaxies. For example, in Kelly et al., 2018 the authors observed a transient event in a strongly lensed galaxy which formed multiple merging images. This event turned out to be a single star in the background galaxy, which was temporarily boosted to an extreme magnification by microlensing when a star in the lensing cluster passed in front of the lensed image of the background star. This technique has also been used to discover lensed stars in Rodney et al., 2018; Chen et al., 2019; Kaurov et al., 2019. These discoveries have led some researchers to propose

that similar techniques can be used to observed much more distant stars, including potentially directly observing Pop III stars with JWST (Windhorst et al., 2018).

References

Bromm, Volker and Richard B. Larson (2004). "The First Stars". In: *ARA&A* 42.1, pp. 79–118. DOI: 10.1146/annurev.astro.42.053102.134034. arXiv: astro-ph/0311019 [astro-ph].

Hosokawa, Takashi, Shingo Hirano, Rolf Kuiper, Harold W. Yorke, Kazuyuki Omukai, and Naoki Yoshida (2016). "Formation of Massive Primordial Stars: Intermittent UV Feedback with Episodic Mass Accretion". In: *ApJ* 824.2, 119, p. 119. DOI: 10.3847/0004-637X/824/2/119. arXiv: 1510.01407 [astro-ph.GA].

Haemmerlé, Lionel, Tyrone E. Woods, Ralf S. Klessen, Alexander Heger, and Daniel J. Whalen (2018). "On the Rotation of Supermassive Stars". In: *ApJL* 853.1, L3, p. L3. DOI: 10.3847/2041-8213/aaa462. arXiv: 1711.09916 [astro-ph.SR].

Chiaki, Gen, Hajime Susa, and Shingo Hirano (2018). "Metal-poor star formation triggered by the feedback effects from Pop III stars". In: *MNRAS* 475.4, pp. 4378–4395. DOI: 10.1093/mnras/sty040. arXiv: 1801.01583 [astro-ph.GA].

Heger, A., C. L. Fryer, S. E. Woosley, N. Langer, and D. H. Hartmann (2003). "How Massive Single Stars End Their Life". In: *ApJ* 591.1, pp. 288–300. DOI: 10.1086/375341. arXiv: astro-ph/0212469 [astro-ph].

Nagele, Chris, Hideyuki Umeda, Koh Takahashi, Takashi Yoshida, and Kohsuke Sumiyoshi (2020). "The final fate of supermassive M $\sim 5 \times 10^4$ $M_\odot$ Pop III stars: explosion or collapse?" In: *MNRAS* 496.2, pp. 1224–1231. DOI: 10.1093/mnras/staa1636. arXiv: 2006.08834 [astro-ph.HE].

Vanzella, E., M. Meneghetti, G. B. Caminha, M. Castellano, F. Calura, P. Rosati, C. Grillo, M. Dijkstra, M. Gronke, E. Sani, A. Mercurio, P. Tozzi, M. Nonino, S. Cristiani, M. Mignoli, L. Pentericci, R. Gilli, T. Treu, K. Caputi, G. Cupani, A. Fontana, A. Grazian, and I. Balestra (2020). "Candidate Population III stellar complex at z = 6.629 in the MUSE Deep Lensed Field". In: *MNRAS*

494.1, pp. L81–L85. DOI: 10.1093/mnrasl/slaa041. arXiv: 2001.03619 [astro-ph.GA].

Pelliccia, Debora, Victoria Strait, Brian C. Lemaux, Maruša Bradač, Dan Coe, Patricia Bolan, Larry D. Bradley, Brenda Frye, Pratik J. Gandhi, Ramesh Mainali, Charlotte Mason, Masami Ouchi, Keren Sharon, Michele Trenti, and Adi Zitrin (2021). "RELICS-DP7: Spectroscopic Confirmation of a Dichromatic Primeval Galaxy at z $\sim$ 7". In: *ApJL* 908.2, L30, p. L30. DOI: 10.3847/2041-8213/abdf56. arXiv: 2011.08857 [astro-ph.GA].

Windhorst, Rogier A., F. X. Timmes, J. Stuart B. Wyithe, Mehmet Alpaslan, Stephen K. Andrews, Daniel Coe, Jose M. Diego, Mark Dijkstra, Simon P. Driver, Patrick L. Kelly, and Duho Kim (2018). "On the Observability of Individual Population III Stars and Their Stellar-mass Black Hole Accretion Disks through Cluster Caustic Transits". In: *ApJS* 234.2, 41, p. 41. DOI: 10.3847/1538-4365/aaa760. arXiv: 1801.03584 [astro-ph.GA].

Coe, Dan, Adi Zitrin, Mauricio Carrasco, Xinwen Shu, Wei Zheng, Marc Postman, Larry Bradley, Anton Koekemoer, Rychard Bouwens, Tom Broadhurst, Anna Monna, Ole Host, Leonidas A. Moustakas, Holland Ford, John Moustakas, Arjen van der Wel, Megan Donahue, Steven A. Rodney, Narciso Benítez, Stephanie Jouvel, Stella Seitz, Daniel D. Kelson, and Piero Rosati (2013). "CLASH: Three Strongly Lensed Images of a Candidate z $\approx$ 11 Galaxy". In: *ApJ* 762.1, 32, p. 32. DOI: 10.1088/0004-637X/762/1/32. arXiv: 1211.3663 [astro-ph.CO].

Oesch, P. A., G. Brammer, P. G. van Dokkum, G. D. Illingworth, R. J. Bouwens, I. Labbé, M. Franx, I. Momcheva, M. L. N. Ashby, G. G. Fazio, V. Gonzalez, B. Holden, D. Magee, R. E. Skelton, R. Smit, L. R. Spitler, M. Trenti, and S. P. Willner (2016). "A Remarkably Luminous Galaxy at z=11.1 Measured with Hubble Space Telescope Grism Spectroscopy". In: *ApJ* 819.2, 129, p. 129. DOI: 10.3847/0004-637X/819/2/129. arXiv: 1603.00461 [astro-ph.GA].

Harikane, Yuichi, Akio K. Inoue, Ken Mawatari, Takuya Hashimoto, Satoshi Yamanaka, Yoshinobu Fudamoto, Hiroshi Matsuo, Yoichi Tamura, Pratika Dayal, L. Y. Aaron Yung, Anne Hutter, Fabio Pacucci, Yuma Sugahara, and Anton M. Koekemoer (2021). "A Search for H-Dropout Lyman Break Galaxies at z$\sim$12-16". In: *arXiv e-prints*, arXiv:2112.09141, arXiv:2112.09141. arXiv: 2112.09141 [astro-ph.GA].

Pillepich, Annalisa, Volker Springel, Dylan Nelson, Shy Genel, Jill Naiman, Rüdiger Pakmor, Lars Hernquist, Paul Torrey, Mark Vogelsberger, Rainer Weinberger, and Federico Marinacci (2018). "Simulating galaxy formation

with the IllustrisTNG model". In: *MNRAS* 473.3, pp. 4077–4106. DOI: 10.1093/mnras/stx2656. arXiv: 1703.02970 [astro-ph.GA].

Finkelstein, Steven L. (2016). "Observational Searches for Star-Forming Galaxies at z > 6". In: *PASA* 33, e037, e037. DOI: 10.1017/pasa.2016.26. arXiv: 1511.05558 [astro-ph.GA].

Elmegreen, Bruce G. and Debra Meloy Elmegreen (2005). "Stellar Populations in 10 Clump-Cluster Galaxies of the Hubble Ultra Deep Field". In: *ApJ* 627.2, pp. 632–646. DOI: 10.1086/430514. arXiv: astro-ph/0504032 [astro-ph].

Elmegreen, Debra Meloy, Bruce G. Elmegreen, Swara Ravindranath, and Daniel A. Coe (2007). "Resolved Galaxies in the Hubble Ultra Deep Field: Star Formation in Disks at High Redshift". In: *ApJ* 658.2, pp. 763–777. DOI: 10.1086/511667. arXiv: astro-ph/0701121 [astro-ph].

Elmegreen, Bruce G., Debra Meloy Elmegreen, Maria Ximena Fernandez, and Jenna Jo Lemonias (2009). "Bulge and Clump Evolution in Hubble Ultra Deep Field Clump Clusters, Chains and Spiral Galaxies". In: *ApJ* 692.1, pp. 12–31. DOI: 10.1088/0004-637X/692/1/12. arXiv: 0810.5404 [astro-ph].

Livermore, R. C., T. A. Jones, J. Richard, R. G. Bower, A. M. Swinbank, T. T. Yuan, A. C. Edge, R. S. Ellis, L. J. Kewley, Ian Smail, K. E. K. Coppin, and H. Ebeling (2015). "Resolved spectroscopy of gravitationally lensed galaxies: global dynamics and star-forming clumps on ∼100 pc scales at 1 < z < 4". In: *MNRAS* 450.2, pp. 1812–1835. DOI: 10.1093/mnras/stv686. arXiv: 1503.07873 [astro-ph.GA].

Johnson, Traci L., Jane R. Rigby, Keren Sharon, Michael D. Gladders, Michael Florian, Matthew B. Bayliss, Eva Wuyts, Katherine E. Whitaker, Rachael Livermore, and Katherine T. Murray (2017). "Star Formation at z = 2.481 in the Lensed Galaxy SDSS J1110+6459: Star Formation Down to 30 pc Scales". In: *ApJL* 843.2, L21, p. L21. DOI: 10.3847/2041-8213/aa7516. arXiv: 1707.00706 [astro-ph.GA].

Zick, Tom O., Daniel R. Weisz, Bruno Ribeiro, Mariska T. Kriek, Benjamin D. Johnson, Xiangcheng Ma, and Rychard Bouwens (2020). "Towards studying hierarchical assembly in real time: a Milky Way progenitor galaxy at z = 2.36 under the microscope". In: *MNRAS* 493.4, pp. 5653–5661. DOI: 10.1093/mnras/staa543. arXiv: 2002.07822 [astro-ph.GA].

Vanzella, E., F. Calura, M. Meneghetti, M. Castellano, G. B. Caminha, A. Mercurio, G. Cupani, P. Rosati, C. Grillo, R. Gilli, M. Mignoli, G. Fiorentino, C. Arcidiacono, M. Lombini, and F. Cortecchia (2019). "Massive star cluster

formation under the microscope at z = 6". In: *MNRAS* 483.3, pp. 3618–3635. DOI: 10.1093/mnras/sty3311. arXiv: 1809.02617 [astro-ph.GA].

Salmon, Brett, Casey Papovich, Steven L. Finkelstein, Vithal Tilvi, Kristian Finlator, Peter Behroozi, Tomas Dahlen, Romeel Davé, Avishai Dekel, Mark Dickinson, Henry C. Ferguson, Mauro Giavalisco, James Long, Yu Lu, Bahram Mobasher, Naveen Reddy, Rachel S. Somerville, and Risa H. Wechsler (2015). "The Relation between Star Formation Rate and Stellar Mass for Galaxies at 3.5 <= z <= 6.5 in CANDELS". In: *ApJ* 799.2, 183, p. 183. DOI: 10.1088/0004-637X/799/2/183. arXiv: 1407.6012 [astro-ph.GA].

Behroozi, Peter S., Risa H. Wechsler, and Charlie Conroy (2013). "The Average Star Formation Histories of Galaxies in Dark Matter Halos from z = 0-8". In: *ApJ* 770.1, 57, p. 57. DOI: 10.1088/0004-637X/770/1/57. arXiv: 1207.6105 [astro-ph.CO].

Robertson, Brant E. (2021). "Galaxy Formation and Reionization: Key Unknowns and Expected Breakthroughs by the James Webb Space Telescope". In: *arXiv e-prints*, arXiv:2110.13160, arXiv:2110.13160. arXiv: 2110.13160 [astro-ph.CO].

Planck Collaboration et al. (2020). "Planck 2018 results. VI. Cosmological parameters". In: *A&A* 641, A6, A6. DOI: 10.1051/0004-6361/201833910. arXiv: 1807.06209 [astro-ph.CO].

Ouchi, Masami, Kazuhiro Shimasaku, Hisanori Furusawa, Tomoki Saito, Makiko Yoshida, Masayuki Akiyama, Yoshiaki Ono, Toru Yamada, Kazuaki Ota, Nobunari Kashikawa, Masanori Iye, Tadayuki Kodama, Sadanori Okamura, Chris Simpson, and Michitoshi Yoshida (2010). "Statistics of 207 Lyα Emitters at a Redshift Near 7: Constraints on Reionization and Galaxy Formation Models". In: *ApJ* 723.1, pp. 869–894. DOI: 10.1088/0004-637X/723/1/869. arXiv: 1007.2961 [astro-ph.CO].

Kulkarni, Girish, Gábor Worseck, and Joseph F. Hennawi (2019). "Evolution of the AGN UV luminosity function from redshift 7.5". In: *MNRAS* 488.1, pp. 1035–1065. DOI: 10.1093/mnras/stz1493. arXiv: 1807.09774 [astro-ph.GA].

Kravtsov, Andrey V. and Stefano Borgani (2012). "Formation of Galaxy Clusters". In: *ARA&A* 50, pp. 353–409. DOI: 10.1146/annurev-astro-081811-125502. arXiv: 1205.5556 [astro-ph.CO].

Ellis, Richard S., Ian Smail, Alan Dressler, Warrick J. Couch, Jr. Oemler Augustus, Harvey Butcher, and Ray M. Sharples (1997). "The Homogeneity of Spheroidal Populations in Distant Clusters". In: *ApJ* 483.2, pp. 582–596. DOI: 10.1086/304261. arXiv: astro-ph/9607154 [astro-ph].

Stanford, S. A., Peter R. Eisenhardt, and Mark Dickinson (1998). "The Evolution of Early-Type Galaxies in Distant Clusters". In: *ApJ* 492.2, pp. 461–479. DOI: 10.1086/305050. arXiv: astro-ph/9708037 [astro-ph].

Gunn, James E. and III Gott J. Richard (1972). "On the Infall of Matter Into Clusters of Galaxies and Some Effects on Their Evolution". In: *ApJ* 176, p. 1. DOI: 10.1086/151605.

Butcher, H. and Jr. Oemler A. (1978). "The evolution of galaxies in clusters. I. ISIT photometry of Cl 0024+1654 and 3C 295." In: *ApJ* 219, pp. 18–30. DOI: 10.1086/155751.

Butcher, H. and Jr. Oemler A. (1984). "The evolution of galaxies in clusters. V. A study of populations since Z 0.5." In: *ApJ* 285, pp. 426–438. DOI: 10.1086/162519.

Hicks, A. K., R. Mushotzky, and M. Donahue (2010). "Detecting Star Formation in Brightest Cluster Galaxies with GALEX". In: *ApJ* 719, pp. 1844–1858. DOI: 10.1088/0004-637X/719/2/1844. arXiv: 1006.3074.

Ebeling, H., L. N. Stephenson, and A. C. Edge (2014). "Jellyfish: Evidence of Extreme Ram-pressure Stripping in Massive Galaxy Clusters". In: *ApJL* 781.2, L40, p. L40. DOI: 10.1088/2041-8205/781/2/L40. arXiv: 1312.6135 [astro-ph.GA].

Einstein, A. (1916). "Die Grundlage der allgemeinen Relativitätstheorie". In: *Annalen der Physik* 354.7, pp. 769–822. DOI: 10.1002/andp.19163540702.

Coe, D., E. Fuselier, N. Benítez, T. Broadhurst, B. Frye, and H. Ford (2008). "LensPerfect: Gravitational Lens Mass Map Reconstructions Yielding Exact Reproduction of All Multiple Images". In: *ApJ* 681.2, pp. 814–830. DOI: 10.1086/588250. arXiv: 0803.1199 [astro-ph].

Kelly, Patrick L., Jose M. Diego, Steven Rodney, Nick Kaiser, Tom Broadhurst, Adi Zitrin, Tommaso Treu, Pablo G. Pérez-González, Takahiro Morishita, Mathilde Jauzac, Jonatan Selsing, Masamune Oguri, Laurent Pueyo, Timothy W. Ross, Alexei V. Filippenko, Nathan Smith, Jens Hjorth, S. Bradley Cenko, Xin Wang, D. Andrew Howell, Johan Richard, Brenda L. Frye, Saurabh W. Jha, Ryan J. Foley, Colin Norman, Marusa Bradac, Weikang Zheng, Gabriel Brammer, Alberto Molino Benito, Antonio Cava, Lise Christensen, Selma E. de Mink, Or Graur, Claudio Grillo, Ryota Kawamata, Jean-Paul Kneib, Thomas Matheson, Curtis McCully, Mario Nonino, Ismael Pérez-Fournon, Adam G. Riess, Piero Rosati, Kasper Borello Schmidt, Keren Sharon, and Benjamin J. Weiner (2018). "Extreme magnification of

an individual star at redshift 1.5 by a galaxy-cluster lens". In: *Nature Astronomy* 2, pp. 334–342. DOI: 10.1038/s41550-018-0430-3. arXiv: 1706.10279 [astro-ph.GA].

Rodney, S. A., I. Balestra, M. Bradac, G. Brammer, T. Broadhurst, G. B. Caminha, G. Chirivì, J. M. Diego, A. V. Filippenko, R. J. Foley, O. Graur, C. Grillo, S. Hemmati, J. Hjorth, A. Hoag, M. Jauzac, S. W. Jha, R. Kawamata, P. L. Kelly, C. McCully, B. Mobasher, A. Molino, M. Oguri, J. Richard, A. G. Riess, P. Rosati, K. B. Schmidt, J. Selsing, K. Sharon, L. G. Strolger, S. H. Suyu, T. Treu, B. J. Weiner, L. L. R. Williams, and A. Zitrin (2018). "Two peculiar fast transients in a strongly lensed host galaxy". In: *Nature Astronomy* 2, pp. 324–333. DOI: 10.1038/s41550-018-0405-4. arXiv: 1707.02434 [astro-ph.GA].

Chen, Wenlei, Patrick L. Kelly, Jose M. Diego, Masamune Oguri, Liliya L. R. Williams, Adi Zitrin, Tommaso L. Treu, Nathan Smith, Thomas J. Broadhurst, Nick Kaiser, Ryan J. Foley, Alexei V. Filippenko, Laura Salo, Jens Hjorth, and Jonatan Selsing (2019). "Searching for Highly Magnified Stars at Cosmological Distances: Discovery of a Redshift 0.94 Blue Supergiant in Archival Images of the Galaxy Cluster MACS J0416.1-2403". In: *ApJ* 881.1, 8, p. 8. DOI: 10.3847/1538-4357/ab297d. arXiv: 1902.05510 [astro-ph.GA].

Kaurov, Alexander A., Liang Dai, Tejaswi Venumadhav, Jordi Miralda-Escudé, and Brenda Frye (2019). "Highly Magnified Stars in Lensing Clusters: New Evidence in a Galaxy Lensed by MACS J0416.1-2403". In: *ApJ* 880.1, 58, p. 58. DOI: 10.3847/1538-4357/ab2888. arXiv: 1902.10090 [astro-ph.GA].

Chapter 2

Galaxy Cluster Contribution to the Diffuse Extragalactic Ultraviolet Background

2.1 Introduction

Diffuse background radiation can be observed across the entire electromagnetic spectrum, from the Cosmic Microwave Background (CMB) radiation (Penzias and Wilson, 1965) to the highest energy gamma rays (Inoue, 2014). In the ultraviolet (UV), the largest contributor to the background is of Galactic origin. Previous studies have seen clear correlations between diffuse UV excesses and tracers of interstellar gas and dust, indicating that the primary contributor is scattered starlight (Bowyer, 1991; Murthy, Henry, and Sujatha, 2010). However, there is a notable non-scattered component to this background, observable as a ~ 300 photon cm^{-2} s-1 sr^{-1} Å^{-1} (continuum units, CU) background observed in low column density regions near the Galactic poles (Henry, 1991; Hamden, Schiminovich, and Seibert, 2013; Murthy, 2016). While there is some debate as to the origin of this portion of the background,

some component is likely extragalactic. Murthy, 2016 calculated that of the $\sim$ 300 CU background observed at the Galactic poles, around 100 CU is unexplained by galactic processes, and is therefore likely extragalactic in origin. Recently, Chiang, Ménard, and Schiminovich, 2019 used a combination of *GALEX* and SDSS data to calculate that the total extragalactic background of 89^{+28}_{-16} CU, while Akshaya et al., 2018 used *GALEX* data at the Galactic poles to calculate a total extragalactic background of 114 ± 18 CU.

The sources of extragalactic ultraviolet background radiation are generally assumed to be active galactic nuclei and star-forming galaxies (Upton Sanderbeck et al., 2018; Becker and Bolton, 2013). These appear to be the dominant sources of metagalactic ultraviolet radiation, and they are believed to be the primary sources of ionizing ultraviolet radiation in the Epoch of Reionization. However, precise measurements of the UV background are difficult, and recent measurements of the relative contribution of star-forming galaxies and AGN indicate there may be other extragalactic sources. Using number counts of galaxies detected in the FUV band of the *GALEX* survey, Xu et al., 2005 calculated a total contribution from galaxies (in units of λF_λ) of 1.03 ± 0.15 nW m^{-2} sr^{-1}, or 51.5 ± 7.5 CU. Voyer et al., 2011 performed a similar calculation with HST data. They used number counts of field galaxies from the GOODS fields, the Deep Field North, and the Ultra-Deep Field with FUV magnitudes between 21 and 29 AB in the ACS Solar Blind Channel, and calculated a contribution to the UV background of 65.9 to 82.6 CU. More recently, Chiang, Ménard, and Schiminovich, 2019 used a broadband intensity tomography method with a combination of *GALEX* and SDSS data to calculate

the combined contribution from galaxies and AGN to be 73 ± 8 CU. While it is clear from these measurements that star-forming galaxies and AGN are the dominant contributors to the extragalactic background, they each leave room for additional sources. Additionally, Akshaya et al., 2018; Akshaya et al., 2019 used *GALEX* data to tabulate the contributions to the UV background from dust-scattered starlight and known extragalactic sources near the Galactic poles. They found an unexplained offset of $\sim$ 200 CU at zero dust column density ($E(B-V) = 0$) in the FUV band. While they do not identify the source of this offset, they speculate that hitherto unknown extragalactic sources could be contributing to this offset.

In this paper, we explore another possible source contributing to the diffuse ultraviolet background: massive clusters of galaxies. While not traditionally associated with high ultraviolet luminosities, the high density of galaxies and hot gas in massive galaxy clusters suggests them as candidate sources of excess diffuse light. Utilizing UV background data from the *GALEX* survey (Murthy, 2014) and massive galaxy clusters from the *Planck* survey (Planck Collaboration et al., 2016), we measure the correlation between galaxy clusters and diffuse UV background light.

This paper is organized as follows. Section 2 describes the data from the *GALEX* and *Planck* surveys. Section 3 details the analysis methods used to investigate the correlation between clusters of galaxies and diffuse UV background light. Section 4 presents and discusses the results of our analysis, and Section 5 presents our summary and conclusions.

2.2 Data

2.2.1 Galex FUV Background Catalogs

GALEX was an orbiting ultraviolet observatory that made use of a 50 cm Ritchey-Chretien telescope to image a 1.2° circular field of view onto two detectors (Martin et al., 2005). The detectors operate in two different bandpasses, one in the far-UV from 1350 - 1750 Å, and the other in the near-UV from 1750 - 2750 Å.

Our analysis focuses on the FUV bandpass data from the GR6/GR7 data release, which was further processed by Murthy, 2014 into a map of diffuse background FUV flux. Briefly, this map was made by masking all point sources found in the standard *GALEX* data reduction pipeline (Morrissey et al., 2007) in the raw images, then binning the image data into 2′ pixels. Masked pixels were ignored in the binning, thus replacing them with an average from the full 2′ binned pixel.

We restrict our analysis to Galactic latitudes $|b| > 60°$. This allows us to avoid the most significant Galactic contributions to the diffuse UV background light, and focus on the extragalactic component. Restricting our sample this way ensures that our results are not significantly biased by Galactic scattered stellar light.

2.2.2 Planck SZ Cluster Sample

For this work, we analyze a subsample of clusters from the second *Planck* catalog of Sunyaev-Zeldovich sources (Planck Collaboration et al., 2016). These

clusters are detected via their thermal Sunyaev-Zeldovich effect signal (Sunyaev and Zeldovich, 1970), wherein hot gas in the intracluster medium inverse Compton scatters photons from the CMB to higher energies. This effect causes a decreased intensity at lower frequencies and an increased intensity at higher frequencies.

For our investigations, we select only clusters which have a measured redshift and SZ mass. We further select only clusters which lie in the Galactic cap region, with latitudes $|b| > 60°$. We then visually inspected the sample and discarded any clusters with incomplete or irregular *GALEX* background data, for example those near large holes in the background map or with partial data near the edges of our window. This left a sample of 185 clusters. A final cut was applied after matching the cluster positions to the *GALEX* data. Clusters with no UV background data present within the central region, as described in Section 2.3, were excluded from our analysis. This left a final sample of 142 clusters. The masses and redshifts of these clusters are shown in Figure 2.1.

2.3 Methods

To analyze the level of UV background light around our sample of galaxy clusters, we created radial UV brightness profiles. These were made by matching all *GALEX* data within 10 Mpc of the cluster centers, binned into annuli sized to accommodate the 2′ background map resolution. Any clusters with no *GALEX* data matched within the central region are removed from the final sample to ensure all fully analyzed clusters have complete data. To overcome

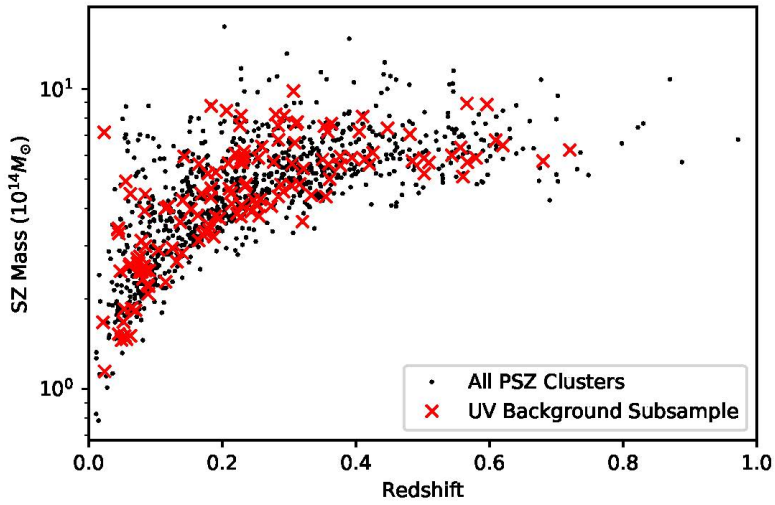

Figure 2.1: Distribution of *Planck* SZ cluster masses (in units of $10^{14} M_\odot$) and redshifts. Clusters within our sample are highlighted with a red X.

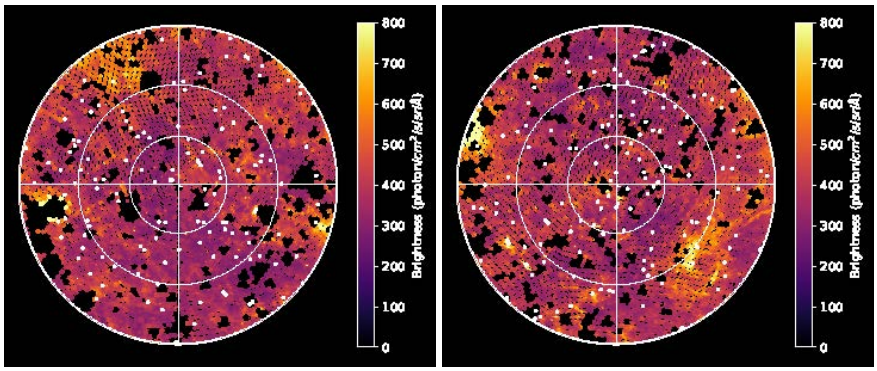

Figure 2.2: Northern (left) and southern (right) Galactic cap *GALEX* FUV background map, down to $|b| = 60°$. Locations of the *Planck* clusters used in this study are marked with white circles.

Redshift Bin	Number of Clusters	Annulus Size (Mpc)
$0.02 < z \leq 0.1$	37	0.25
$0.1 < z \leq 0.2$	27	0.4
$0.2 < z \leq 0.3$	35	0.5
$z > 0.3$	43	1.0

Table 2.1: Summary of our cluster sample binned by redshift.

the high variability between individual clusters, we stacked our sample to create a median cluster radial brightness profile. Uncertainties on this profile were estimated by randomly resampling UV background fluxes with replacement at each radius. Murthy, 2014 calculates a photon count uncertainty of 18 CU per 2 $'$ pixel. To account for this uncertainty, we add Gaussian noise with standard deviation $\sigma = 18\text{CU}/\sqrt{N_{pix}}$ to each sample drawn, where N_{pix} is the number of 2$'$ pixels included in the given annular bin. We used the standard deviation of the mean of 1000 random resampling iterations as the flux uncertainty at a given radius.

We divided our cluster sample into four redshift bins to maximize the resolution of our radial profile measurements at lower redshifts while still being able to analyze the full redshift range. The redshift bins and associated annular sizes are summarized in Table 2.1. The annulus sizes were chosen to match the 2$'$ pixel scale at the high end of each redshift bin, thus ensuring that at least one pixel will be included within the central region.

We found evidence of a central excess in each of our redshift bins below $z = 0.3$, discussed further in Section 2.4. This led us to stack our full sample of $z \leq 0.3$ clusters in an attempt to maximize our signal-to-noise, giving us a sample of 99 clusters. We stacked these clusters with annular bin sizes of 0.5

Mpc, corresponding to the maximum spatial resolution possible at $z = 0.3$.

The shape of the stacked cluster profile is informative on its own; However comparison with a blank field profile provides a useful context for this measurement. The blank field profile is constructed by randomly selecting 185 locations on the sky, subject to the same $|b| > 60°$ restriction as our cluster sample. These locations are matched to the *GALEX* data in the same way as the cluster sample. The same cut on points with no central data are applied, leaving a final random field sample of $\sim 120 - 150$ points per iteration, similar in number to our final cut cluster sample of 142 clusters. Blank fields obviously do not have an associated redshift, so we randomly select a redshift for each field within the range $[0.01, 0.3]$, encompassing the redshift range of our primary stacked sample. A stacked radial profile is then computed for this set of random blank fields, with the same stacking procedure as in the cluster sample. To account for cosmic variance and variations in the UV background radiation field, we repeat this random field measurement 1000 times. The uncertainty values for the blank field radial profile measurements are calculated as the standard deviation of the mean of the 1000 iterations, mimicking the randomly resampled uncertainty calculation of the cluster sample.

2.4 Results and Discussion

Our stacked radial profile of all clusters with $z \leq 0.3$ (Figure 2.3) shows a clear excess of UV background radiation at the locations of Planck SZ-selected clusters. The peak excess of 12 ± 2.3 CU (a 5.0σ detection) is coincident with

the cluster center.

The cluster signal decays rapidly further from the cluster center. The UV background brightness in the cluster fields drops back to be consistent with the random fields within 1 Mpc, roughly consistent with the virial radii of massive clusters. The coarse binning of the UV background map prevents more detailed analysis of the shape of the brightness profile for the full $z \leq 0.3$ sample.

Dividing the sample into smaller redshift bins allows us to look in more detail at the central region of nearer clusters (Figure 2.4). In our lowest redshift subsample ($z \leq 0.1$) our 0.25 Mpc annuli give us the greatest chance to probe the centers of our clusters. In this sample we see that the two innermost points ($r < 0.25$ Mpc and $0.25 < r < 0.5$ Mpc) are both elevated above the background level, indicating that the background emission source extends over the full central 0.5 Mpc. Beyond $z = 0.1$, our annulus sizes become too large (0.4 Mpc for $0.1 < z \leq 0.2$) to see this innermost detail. We continue to see a clear central excess in the $0.1 < z \leq 0.2$ bin, while the $0.2 < z \leq 0.3$ redshift bin shows mild evidence of a central excess. The highest redshift bin ($z > 0.3$) shows no evidence of central excess. We attribute this lack of signal in the highest redshift bin to the larger annuli required to match the background map resolution. Our lower redshift samples show that the excess has decayed to the background level within 1 Mpc, so annuli of 1 Mpc cannot detect the central peak. Additionally, Murthy, 2014 explains that the $2'$ pixels display the average of all original *GALEX* pixel background values within the region. Thus any signal of central excess will be further washed out in these

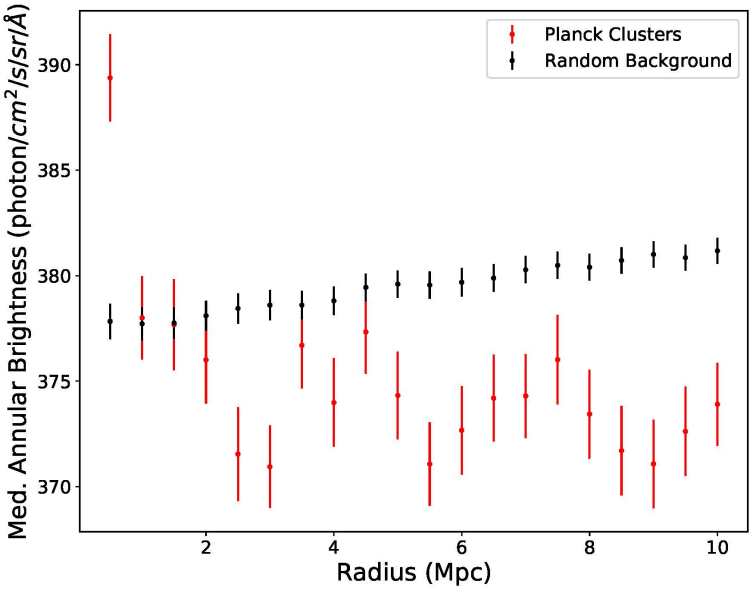

Figure 2.3: FUV background fluxes measured around $z \leq 0.3$ Planck SZ galaxy clusters (red points with errorbars) and around randomly selected points on the sky (black points with errorbars). Uncertainty calculations are discussed in detail in the text. The excess flux around galaxy clusters is clearly visible at $r = 0.5$ Mpc, and rapidly falls off to the background level beyond that point.

higher redshift clusters.

Below we estimate contributions to the cluster excess from various sources.

2.4.1 BCG or Infalling Jellyfish Galaxies

It is possible that this central excess is originating from the brightest cluster galaxy (BCG). Previous studies have found that cluster BCGs can be UV bright, particularly in cases of cool-core clusters where the BCG is actively forming stars (Hicks, Mushotzky, and Donahue, 2010). These galaxies, with star-formation rates $0.01 \leq SFR \leq 10$, would be bright enough to provide the full

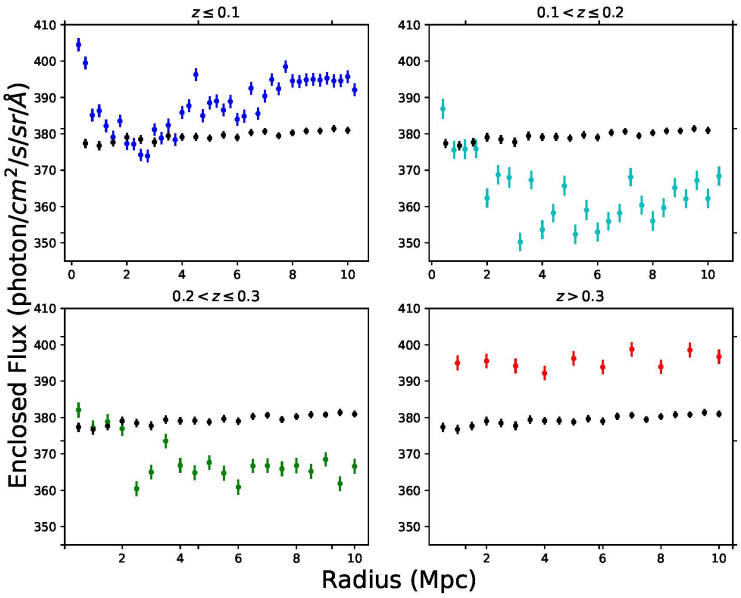

Figure 2.4: UV background radial profiles in each of four redshift bins. Black points in each plot are blank field measurements, as described in the text. Central excesses are visible in each bin below $z = 0.3$.

excess we measure within the central 0.5 Mpc of the cluster. However, these galaxies would be detectable in the *GALEX* survey, with an all-sky survey limiting magnitude of 19.9 in the FUV. Therefore these galaxies would most likely be masked in the background maps. It is possible that incomplete masking could allow UV flux from the BCG to leak into the maps and contribute to our observed signal. It is impossible to determine the exact contribution of incomplete masking on our result without remaking the background maps.

Additionally, BCG star formation studies have focused on much smaller scales ($\sim$ 10 kpc as opposed to Mpc). Finally, our sample includes many clusters that are not known to have active star formation in their central galaxies, indicating alternative sources of UV background light production. Therefore it is unlikely that BCG star formation is the primary contributor to the excess UV flux observed.

Similarly, it is possible that star formation in infalling field galaxies or jellyfish galaxies being pressure stripped as they fall into the cluster could contribute to our signal. While these galaxies would likely have elevated star formation rates, and thus greater emission in the UV, they would likely be bright enough to be detected by GALEX. They would therefore be masked out of our background sample, and unlikely to contribute to the observed excess.

2.4.2 Cluster Gas Emission Estimates: Thermal Brehmsstrahlung and Inverse Compton Scattering

Clusters are full of hot gas, which is known to radiate brightly in X-rays through the combined effects of thermal brehmsstrahlung and inverse Compton scattering of CMB photons off hot electrons. We considered these as possible contributors to our measured signal in the FUV, as these spectra for a typical cluster continue to longer wavelengths.

In our FUV bandpass, the brehmsstrahlung luminosity is $L_\nu \sim 10^{27}$ erg sec^{-1} Hz^{-1} (Sarazin, 1999; Sarazin, 2005). We assume a cluster redshift of $z = 0.3$, because most of our clusters are within this range and changes in assumed redshift do not drastically impact our results. This gives a calculated FUV surface brightness of ~ 0.2 CU over an area of $2'$, matching the resolution of the background map. The fact that this calculated surface brightness is much smaller than our measured excess indicates that brehmsstrahlung radiation from cluster gas is likely not a dominant contributor to our observed signal.

Another possibility is that shocks generated by cluster mergers accelerate relativistic electrons within the cluster, which emit ultraviolet light through the inverse Compton effect. Sarazin, 2005 calculated that these electrons would have lifetimes of order a Hubble time, so the cluster would not have to have been through a recent merger for this effect to be visible. They also calculated a spectrum for the emission, giving a luminosity in the FUV bandpass of $L_\nu \sim 10^{28.5}$ erg sec^{-1} Hz^{-1}. Again assuming a cluster redshift $z = 0.3$, we calculate the FUV surface brightness of this emission to be 8 CU, again over

an area of $2'$. This indicates that emission from shock-accelerated electrons in the intracluster medium is likely a significant contributor to the signal we observe.

2.4.3 Cluster Emission from Stripped Stars

While cluster galaxies generally contain old stellar populations, these galaxies will still emit a small amount of ultraviolet light. Each galaxy would be too faint to be detected individually by *GALEX*, thus all of their light would be incorporated into the UV background. There may be a small additional contribution from the stars that make up the intracluster light. These stars are mostly stripped from cluster member galaxies (DeMaio et al., 2018), thus they would primarily be old, red stars. However, there is some evidence of in-situ star formation in the intracluster medium (Puchwein et al., 2010; Tonnesen and Bryan, 2012), which could enhance the UV contribution of intracluster stars. The sum of the unresolvable UV emission from these stars and the cluster galaxies could account for our measured excess. To test this hypothesis accounting for both cluster member galaxies and intracluster light, we used optical estimates of the cluster mass-to-light ratio, then calculated an UV surface brightness.

We estimated the optical mass-to-light ratio using the best-fit relation in Popesso et al., 2007. This relation gives the luminosity in the SDSS r-band given a cluster mass. We then used 5 early-type SEDs (see Figure 4 of Coe et al., 2019) exhibiting a range of UV upturn strengths (flux below 1600 Å rest-frame) to calculate the luminosity in the *GALEX* FUV bandpass. This

Mass ($10^{14} M_{\odot}$)	S.B. High (CU)	S.B. Low (CU)
2.0	3.65	1.24
4.0	4.82	1.64
6.0	5.67	1.92
8.0	6.36	2.16
10.0	6.95	2.36

Table 2.2: Surface brightnesses calculated from a range of cluster masses, as described in 2.4.3. Two surface brightnesses are quoted for each mass, one for the highest strength UV upturn and one for the lowest strength UV upturn.

FUV luminosity then allowed us to calculate the expected surface brightness of the unresolved cluster light. For reference, Table 2.2 shows a selection of surface brightness results for a range of cluster masses. We show both the high end surface brightness numbers, calculated assuming an SED with the strongest UV upturn and thus highest UV flux, and the low end surface brightness numbers calculated assuming the weakest UV upturn and lowest UV flux. Our final numbers quoted below are calculated from the median surface brightness of our entire cluster sample.

It is important to note that there is a sizeable uncertainty associated with the conversion between optical and ultraviolet luminosities. However, as a diagnostic tool to inform future studies, this uncertain calculation is useful.

We applied our mass-to-light calculations to our full sample of *Planck* clusters. To compare with our stacked analysis, we took the median of the calculated cluster UV brightnesses. This resulted in median UV brightness measurements of 1.6 CU to 4.7 CU, depending on the SED used for the luminosity conversion. While this is somewhat lower than our measured background excess, we believe it is likely a significant contributor.

2.5 Conclusions

Using *GALEX* data, we measured a 12 ± 2.3 CU excess (5.0σ) of ultraviolet background light associated with $z \leq 0.3$ *Planck* clusters at high Galactic latitudes ($|b| > 60$). We conclude that the excess we measure is extragalactic in nature and directly related to the galaxy clusters. Based on our approximate calculations, we find the two most probable contributors to our measured UV excess are unresolved emission from quiescient cluster members, as well as emission from relativistic electrons in the intracluster medium. With the available data, we cannot accurately measure the relative contributions of each emission mechanism.

Future work could improve upon this analysis by utilizing a more detailed background map. The improved resolution would create a more detailed radial profile which could be compared to cluster mass-to-light profiles and x-ray gas profiles to further test the relative contributions of each proposed emission mechanism. Enhanced resolution would also allow for the inclusion of higher redshift clusters. Including a larger cluster sample, for example an optically-selected sample with a greater mass and redshift range, could further improve constraints on the source of the UV excess.

References

Penzias, A. A. and R. W. Wilson (1965). "A Measurement of Excess Antenna Temperature at 4080 Mc/s." In: *ApJ* 142, pp. 419–421. DOI: 10.1086/148307.

Inoue, Yoshiyuki (2014). "Cosmic Gamma-ray Background Radiation". In: *arXiv e-prints*, arXiv:1412.3886, arXiv:1412.3886. arXiv: 1412.3886 [astro-ph.HE].

Bowyer, S. (1991). "The cosmic far ultraviolet background". In: *ARA&A* 29, pp. 59–88. DOI: 10.1146/annurev.aa.29.090191.000423.

Murthy, Jayant, R. C. Henry, and N. V. Sujatha (2010). "Mapping the Diffuse Ultraviolet Sky with the Galaxy Evolution Explorer". In: *ApJ* 724.2, pp. 1389–1395. DOI: 10.1088/0004-637X/724/2/1389. arXiv: 1009.4530 [astro-ph.GA].

Henry, R. C. (1991). "Ultraviolet background radiation". In: *ARA&A* 29, pp. 89–127. DOI: 10.1146/annurev.aa.29.090191.000513.

Hamden, Erika T., David Schiminovich, and Mark Seibert (2013). "The Diffuse Galactic Far-ultraviolet Sky". In: *ApJ* 779.2, 180, p. 180. DOI: 10.1088/0004-637X/779/2/180. arXiv: 1311.0875 [astro-ph.GA].

Murthy, Jayant (2016). "Modelling dust scattering in our Galaxy". In: *MNRAS* 459.2, pp. 1710–1720. DOI: 10.1093/mnras/stw755. arXiv: 1601.00430 [astro-ph.GA].

Chiang, Yi-Kuan, Brice Ménard, and David Schiminovich (2019). "Broadband Intensity Tomography: Spectral Tagging of the Cosmic UV Background". In: *ApJ* 877.2, 150, p. 150. DOI: 10.3847/1538-4357/ab1b35. arXiv: 1810.00885 [astro-ph.CO].

Akshaya, M. S., Jayant Murthy, S. Ravichandran, R. C. Henry, and James Overduin (2018). "The Diffuse Radiation Field at High Galactic Latitudes". In: *ApJ* 858.2, p. 101. DOI: 10.3847/1538-4357/aabcb9. URL: https://doi.org/10.3847%2F1538-4357%2Faabcb9.

Upton Sanderbeck, P. R., M. McQuinn, A. D'Aloisio, and J. K. Werk (2018). "The Sources of Extreme Ultraviolet and Soft X-Ray Backgrounds". In: *ApJ* 869, 159, p. 159. DOI: 10.3847/1538-4357/aaeff2. arXiv: 1710.07295.

Becker, G. D. and J. S. Bolton (2013). "New measurements of the ionizing ultraviolet background over 2 < z < 5 and implications for hydrogen reionization". In: *MNRAS* 436, pp. 1023–1039. DOI: 10.1093/mnras/stt1610. arXiv: 1307.2259.

Xu, C. Kevin, Jose Donas, Stephane Arnouts, Ted K. Wyder, Mark Seibert, Jorge Iglesias-Páramo, Jeremy Blaizot, Todd Small, Bruno Milliard, David Schiminovich, D. Christopher Martin, Tom A. Barlow, Luciana Bianchi, Yong-Ik Byun, Karl Forster, Peter G. Friedman, Timothy M. Heckman, Patrick N. Jelinsky, Young-Wook Lee, Barry F. Madore, Roger F. Malina, Patrick Morrissey, Susan G. Neff, R. Michael Rich, Oswald H. W. Siegmund, Alex S. Szalay, and Barry Y. Welsh (2005). "Number Counts of GALEX Sources in Far-Ultraviolet (1530 Å) and Near-Ultraviolet (2310 Å) Bands". In: *ApJ* 619.1, pp. L11–L14. DOI: 10.1086/425252. arXiv: astro-ph/0411317 [astro-ph].

Voyer, Elysse N., Jonathan P. Gardner, Harry I. Teplitz, Brian D. Siana, and Duilia F. de Mello (2011). "Far-ultraviolet Number Counts of Field Galaxies". In: *ApJ* 736.2, 80, p. 80. DOI: 10.1088/0004-637X/736/2/80. arXiv: 1105.1398 [astro-ph.CO].

Akshaya, M. S., Jayant Murthy, S. Ravichandran, R. C. Henry, and James Overduin (2019). "Components of the diffuse ultraviolet radiation at high latitudes". In: *MNRAS* 489.1, pp. 1120–1126. DOI: 10.1093/mnras/stz2186. arXiv: 1908.02260 [astro-ph.GA].

Murthy, J. (2014). "GALEX Diffuse Observations of the Sky: The Data". In: *ApJS* 213, 32, p. 32. DOI: 10.1088/0067-0049/213/2/32. arXiv: 1406.5680.

Planck Collaboration, P. A. R. Ade, N. Aghanim, M. Arnaud, M. Ashdown, J. Aumont, C. Baccigalupi, A. J. Banday, R. B. Barreiro, R. Barrena, and et al. (2016). "Planck 2015 results. XXVII. The second Planck catalogue of Sunyaev-Zeldovich sources". In: *A&A* 594, A27, A27. DOI: 10.1051/0004-6361/201525823. arXiv: 1502.01598.

Martin, D. C., J. Fanson, D. Schiminovich, P. Morrissey, P. G. Friedman, T. A. Barlow, T. Conrow, R. Grange, P. N. Jelinsky, B. Milliard, O. H. W. Siegmund, L. Bianchi, Y.-I. Byun, J. Donas, K. Forster, T. M. Heckman, Y.-W. Lee, B. F. Madore, R. F. Malina, S. G. Neff, R. M. Rich, T. Small, F. Surber, A. S. Szalay, B. Welsh, and T. K. Wyder (2005). "The Galaxy Evolution Explorer: A Space Ultraviolet Survey Mission". In: *ApJL* 619, pp. L1–L6. DOI: 10.1086/426387. eprint: astro-ph/0411302.

Morrissey, P., T. Conrow, T. A. Barlow, T. Small, M. Seibert, T. K. Wyder, T. Budavári, S. Arnouts, P. G. Friedman, K. Forster, D. C. Martin, S. G. Neff, D.

Schiminovich, L. Bianchi, J. Donas, T. M. Heckman, Y.-W. Lee, B. F. Madore, B. Milliard, R. M. Rich, A. S. Szalay, B. Y. Welsh, and S. K. Yi (2007). "The Calibration and Data Products of GALEX". In: *ApJS* 173, pp. 682–697. DOI: 10.1086/520512.

Sunyaev, R. A. and Ya. B. Zeldovich (1970). "Small-Scale Fluctuations of Relic Radiation". In: *Ap&SS* 7.1, pp. 3–19. DOI: 10.1007/BF00653471.

Hicks, A. K., R. Mushotzky, and M. Donahue (2010). "Detecting Star Formation in Brightest Cluster Galaxies with GALEX". In: *ApJ* 719, pp. 1844–1858. DOI: 10.1088/0004-637X/719/2/1844. arXiv: 1006.3074.

Sarazin, Craig L. (1999). "The Energy Spectrum of Primary Cosmic-Ray Electrons in Clusters of Galaxies and Inverse Compton Emission". In: *ApJ* 520.2, pp. 529–547. DOI: 10.1086/307501. arXiv: astro-ph/9901061 [astro-ph].

Sarazin, C. L. (2005). "Mergers and Non-Thermal Processes in Clusters of Galaxies". In: *X-Ray and Radio Connections*. Ed. by L. O. Sjouwerman and K. K. Dyer, 8.01, p. 8.01. arXiv: astro-ph/0406181 [astro-ph].

DeMaio, Tahlia, Anthony H. Gonzalez, Ann Zabludoff, Dennis Zaritsky, Thomas Connor, Megan Donahue, and John S. Mulchaey (2018). "Lost but not forgotten: intracluster light in galaxy groups and clusters". In: *MNRAS* 474.3, pp. 3009–3031. DOI: 10.1093/mnras/stx2946. arXiv: 1710.11313 [astro-ph.GA].

Puchwein, Ewald, Volker Springel, Debora Sijacki, and Klaus Dolag (2010). "Intracluster stars in simulations with active galactic nucleus feedback". In: *MNRAS* 406.2, pp. 936–951. DOI: 10.1111/j.1365-2966.2010.16786.x. arXiv: 1001.3018 [astro-ph.CO].

Tonnesen, Stephanie and Greg L. Bryan (2012). "Star formation in ram pressure stripped galactic tails". In: *MNRAS* 422.2, pp. 1609–1624. DOI: 10.1111/j.1365-2966.2012.20737.x. arXiv: 1203.0308 [astro-ph.CO].

Popesso, P., A. Biviano, H. Böhringer, and M. Romaniello (2007). "RASS-SDSS galaxy cluster survey. VII. On the cluster mass-to-light ratio and the halo occupation distribution". In: *A&A* 464.2, pp. 451–464. DOI: 10.1051/0004-6361:20054708. arXiv: astro-ph/0606260 [astro-ph].

Coe, Dan, Brett Salmon, Maruša Bradač, Larry D. Bradley, Keren Sharon, Adi Zitrin, Ana Acebron, Catherine Cerny, Nathália Cibirka, Victoria Strait, Rachel Paterno-Mahler, Guillaume Mahler, Roberto J. Avila, Sara Ogaz, Kuang-Han Huang, Debora Pelliccia, Daniel P. Stark, Ramesh Mainali, Pascal A. Oesch, Michele Trenti, Daniela Carrasco, William A. Dawson, Steven A. Rodney, Louis-Gregory Strolger, Adam G. Riess, Christine Jones, Brenda L. Frye, Nicole G. Czakon, Keiichi Umetsu, Benedetta Vulcani, Or Graur,

Saurabh W. Jha, Melissa L. Graham, Alberto Molino, Mario Nonino, Jens Hjorth, Jonatan Selsing, Lise Christensen, Shotaro Kikuchihara, Masami Ouchi, Masamune Oguri, Brian Welch, Brian C. Lemaux, Felipe Andrade-Santos, Austin T. Hoag, Traci L. Johnson, Avery Peterson, Matthew Past, Carter Fox, Irene Agulli, Rachael Livermore, Russell E. Ryan, Daniel Lam, Irene Sendra-Server, Sune Toft, Lorenzo Lovisari, and Yuanyuan Su (2019). "RELICS: Reionization Lensing Cluster Survey". In: *ApJ* 884.1, 85, p. 85. DOI: 10.3847/1538-4357/ab412b. arXiv: 1903.02002 [astro-ph.GA].

Chapter 3

A Highly Magnified Star at Redshift 6.2

Galaxy clusters magnify background objects through strong gravitational lensing. Typical magnifications for lensed galaxies are factors of a few but can also be as high as tens or hundreds, stretching galaxies into giant arcs (Rivera-Thorsen et al., 2017; Johnson et al., 2017a). Individual stars can attain even higher magnifications given fortuitous alignment with the lensing cluster. Recently, several individual stars at redshift $z \sim 1 - 1.5$ have been discovered, magnified by factors of thousands, temporarily boosted by microlensing (Kelly et al., 2018; Rodney et al., 2018; Chen et al., 2019; Kaurov et al., 2019). Here we report observations of a more distant and persistent magnified star at redshift $z_{\rm phot} = 6.2 \pm 0.1$, 900 Myr after the Big Bang. This star is magnified by a factor of thousands by the foreground galaxy cluster lens WHL0137–08 ($z = 0.566$), as estimated by four independent lens models. Unlike previous lensed stars, the magnification and observed brightness (AB mag 27.2) have remained roughly constant over 3.5 years of imaging and follow-up. The delensed absolute UV magnitude $M_{UV} = -10 \pm 2$ is consistent with a star of

mass $M > 50 M_{\odot}$. Confirmation and spectral classification are forthcoming from approved observations with the *James Webb Space Telescope*.

3.1 A Single Star in the First Billion Years

The Reionization Lensing Cluster Survey (RELICS, Coe et al., 2019) Hubble Space Telescope (*HST*) Treasury Program obtained *HST* Advanced Camera for Surveys (ACS) optical imaging and Wide Field Camera 3 infrared (WFC3/IR) imaging of a total of 41 lensing clusters. Included in these observations was a 15″–long lensed arc of a galaxy at $z_{\rm phot} = 6.2 \pm 0.1$ (Salmon et al., 2020), designated WHL0137-zD1 and nicknamed the "Sunrise Arc" (see Extended Data Table 3.2 and Extended Data Figure 3.4 for photometry and redshift estimate details). Its length rivals the "Sunburst Arc" at $z = 2.4$, the brightest strongly lensed galaxy known (Rivera-Thorsen et al., 2017; Rivera-Thorsen et al., 2019). Within this $z > 6$ galaxy, we have identified a highly magnified star sitting atop the lensing critical curve at RA, Dec = 01:37:23.232, –8:27:52.20 (J2000). This object is designated WHL0137-LS, and we nickname the star "Earendel" from the Old English word meaning "morning star", or "rising light". Follow-up *HST* imaging revealed Earendel is not a transient caustic crossing event; its high magnification has persisted for 3.5 years (see Extended Data Figure 3.5).

We can deduce qualitatively that the magnification of this object must be high given its position within the arc. Multiple images of lensed objects appear on opposite sides of the lensing critical curve, with the critical curve bisecting the two images. Earendel appears at the midpoint between two

images of a star cluster (1.1a/1.1b in Figure 3.1). We only see one image of Earendel, indicating that its two lensed images are unresolved. Thus, the critical curve must fall near the image of the star, indicating that it will have a high magnification.

Our detailed lens modeling supports this interpretation. We model the cluster using four independent techniques: Light-Traces-Mass (LTM, Zitrin et al., 2015; Zitrin et al., 2009; Broadhurst et al., 2005), Lenstool (Jullo and Kneib, 2009; Jullo et al., 2007), Glafic (Oguri, 2010), and WSLAP+ (Diego et al., 2007; Diego et al., 2005). To constrain these models, we identify two triply-lensed clumps 1.1a/b/c and 1.7a/b/c within the Sunrise Arc and one triply-lensed clump within a $z \sim 3$ galaxy to the north (see Extended Data Figure 3.6). Given these modest constraints, our lens models retain a significant degree of freedom. Yet all our models put Earendel within $D_{\rm crit} < 0.1''$ of the critical curve.

Each lens model includes some uncertainty on the model parameters. To understand the effect of these uncertainties, we sampled the posterior distribution generated by the LTM lens model, and generated critical curves from each resultant parameter set. These critical curves are shown in Figure 3.2. We find the star to be within $0.1''$ in $\sim 80\%$ of models, while the maximum distance reaches $0.4''$.

We then derived tighter constraints on the distance to the critical curve based on the fact that we observe only a single unresolved object. If Earendel were farther from the critical curve, we would see two multiple images, as with clumps 1.1a and 1.1b. The single image means either that its two images

are spatially unresolved or that microlensing is suppressing the flux of one image. We deem the latter unlikely given that this cluster has an optically thick microlensing network at the location of the star (see §3.2.6.2 for details). In this configuration, there are no pockets of low magnification which could hide one of the images, as the microcaustics all overlap. Therefore we conclude the two lensed images are unresolved in the current HST WFC3/IR imaging. This is consistent with our original lens model-independent interpretation suggesting it is directly on the critical curve.

We then use the fact that the two images of the star are unresolved to determine the maximum allowed distance to the critical curve. We analyze super-sampled drizzled images and find that two lensed images would be spatially resolved if they were separated by $0.11''$ along the arc (see Extended Data Figure 3.7). Moving each image $0.055''$ along the arc puts them $< 0.036''$ from the critical curve, given the angle between the arc and critical curve in the various lens models (see §3.2.5 for details). Maximum distances to the critical curve ($D_{\rm crit}$) for each lens model are tabulated in Table 3.1. This is a more precise determination than is possible with the weakly constrained lens models alone.

Using the maximum allowed separation, we can calculate the minimum magnification of the lensed star. In the vicinity of the critical curve, magnifications are inversely proportional to the distance to the critical curve:

$$\mu = \mu_0 / D_{\rm crit} \tag{3.1}$$

where $D_{\rm crit}$ is expressed in arcseconds, and μ_0 is a constant that varies between

lens models (Diego, 2019). The value of μ_0 depends on the slope of the lens potential, with flatter potentials yielding higher values of μ_0 and thus higher magnifications for a given distance (i.e. LTM), while steeper potentials give lower magnifications (i.e. Lenstool). Due to the paucity of lensing constraints, we can only determine the slope of the potential to within a factor of 6. However, using multiple lens models, including two Glafic models with one flatter (lower concentration $c = 1$) and one steeper ($c = 7$) potential, we are able to cover the full range of possible outcomes.

Based on this analysis, we derive magnification estimates summarized in Table 3.1. Note the magnification calculated from Equation 3.1 accounts for only one of the two unresolved images. We therefore double this value to get the total magnification from the source to the unresolved image. At the nominal estimated distances $D_{\rm crit}$, the magnification estimates range from $2\mu \sim 1400$ (Lenstool) to $\sim$8400 (LTM). Given the uncertainty on $D_{\rm crit}$, these values may be 0.7 – 5.0 times smaller or larger (68% confidence). Thus the full range of likely magnifications is $2\mu = 1000$ – 40000. This factor of 40 uncertainty is much larger than found for lensed galaxies with typical magnifications of a few(Meneghetti et al., 2017), due to the rapid changes in magnification that occur in the vicinity of lensing critical curves. Future observations will significantly shrink these error bars.

Lower magnifications (at larger $D_{\rm crit}$) are excluded because Earendel is unresolved. Higher magnifications are allowed as the star approaches the caustic. However, based on the cluster stellar mass density in the vicinity of the arc (Extended Data Figure 3.8, Extended Data Table 3.3, §3.2.6.1) we find

that the network of microlensing caustics in the star's vicinity is optically thick (see §3.2.5). Given this microlensing configuration we estimate the maximum magnification to be of order $\mu \lesssim 10^5$, even for a transient caustic crossing (Venumadhav, Dai, and Miralda-Escudé, 2017; Diego et al., 2018; Diego, 2019; Dai, 2021). Microlensing also has the effect of causing fluctuations in observed brightness as the lensed star traverses the microcaustic network. However, due to the optically thick microlensing network we find a 65% probability of the observed brightness staying within a factor of 2 over the 3.5 year span of our observations (Extended Data Figure 3.9). This is consistent with our observed factor ~ 1.4 variation (see §3.2.6.2 for details).

Our strongest evidence that Earendel is an individual star or binary rather than a star cluster comes from our derived 1σ upper limit on its radius. This limit ranges from $r < 0.09$ pc to $r < 0.36$ pc, depending on the lens model. We derive these limits by comparing sheared Gaussian images of various widths to the super-sampled images to determine what sizes are consistent with our observations of a spatially unresolved object (§3.2.5).

All of the lens models yield a radius limit that is smaller than any known star cluster, indicating that this object is more likely an individual star system. The smallest compact star clusters known have typical radii of order ~ 1 pc, with the smallest single example known having a virial radius of 0.7 pc (Portegies Zwart, McMillan, and Gieles, 2010; Figer, McLean, and Morris, 1999). Our largest radius constraint is a factor of two smaller than this star cluster, while our tightest constraint is nearly an order of magnitude smaller. Objects at high redshift may differ from those seen in the local universe, so

we also consider observations and simulations of other high-redshift objects. Bouwens et al., 2017 have measured radii as small as tens of pc for very low luminosity galaxies at $6 < z < 8$, and Vanzella et al., 2019 report $r < 13$ pc star clusters in a a $z = 6.143$ galaxy that is strongly lensed though not on the lensing critical curve. Recent simulations(Behrendt, Schartmann, and Burkert, 2019) resolve star-forming clumps on scales of tens of pc in $z \sim 2$ disks. Our constraints of $r < 0.09 - 0.36$ pc probe significantly smaller scales than these state-of-the-art high-redshift studies. We expect future spectroscopic observations with JWST to conclusively determine that Earendel is one or more individual stars rather than a star cluster.

Most stars of mass $M > 15M_{\odot}$ are observed in binary systems, with a companion at a separation of < 10 AU (Sana et al., 2012; Sana et al., 2014). This is well within our observational radius constraint, suggesting that Earendel is likely composed of multiple stars. However, the mass ratio of these binaries is generally small, ~ 0.5 or less (Moe and Di Stefano, 2017). In such systems, the light from the more massive (and thus brighter) star would dominate our observation. For our primary analysis, we therefore assume that most of the light we observe is coming from a single star. The binary case is discussed further in §3.2.7.

With a magnification between μ = 1000 – 40000, we find Earendel has a delensed flux 1 – 50 pJy (AB mag 38.7 – 34.6) in the F110W filter (0.9 – 1.4 μm), corresponding to an absolute UV (1600Å) magnitude $-8 > M_{AB} > -12$. Based on this, we constrain Earendel's luminosity as a function of temperature in the H-R diagram (Figure 3.3), using a combination of blackbody stellar

spectra at high temperatures ($T_{\rm eff} > 40000$ K) and stellar atmosphere models at lower temperatures (details can be found in §3.2.7).

We compare these constraints to stellar evolution models from Bonn Optimized Stellar Tracks BoOST, Szécsi et al., 2020. We find Earendel's derived luminosity is consistent with a single massive star with initial mass $\sim 40 - 500 M_\odot$ at Zero Age Main Sequence (ZAMS). Note Figure 3.3 shows a fiducial low metallicity ($0.1 Z_\odot$), as might be expected for a $z \sim 6$ galaxy (Shimizu et al., 2016), but we explore other metallicities in §3.2.7 and Extended Data Figure 3.10, finding this does not significantly change our mass estimates given the currently large uncertainties. This single star would either be a massive O-type star on the main sequence with effective temperature ∼60000 K and mass $> 100 M_\odot$ or an evolved O, B, or A-type star with mass $> 40 M_\odot$ and temperature anywhere from ∼8000 – 60000 K. Folding in the times spent at Earendel's derived luminosity for each track and the greater relative abundances of less massive stars, we find masses between 50 – 100 $M_\odot$ and temperatures above 20000K are most likely (see §3.2.7, Extended Data Figure 3.11).

We estimate the probability of observing a star of mass $M \gtrsim 100 M_\odot$ in a caustic-crossing galaxy like the Sunrise Arc to be up to a few percent, making this a fortunate yet reasonable discovery given tens of such galaxies have been observed (see §3.2.8 for details).

The spectral type, temperature, and mass of the star remain uncertain. Future spectroscopic observations with our approved JWST program (GO 2282; PI Coe) will determine these properties for Earendel and place it on the H-R diagram.

Lens Model	μ_0	$D_{\rm crit}$ $''$	magnification 2μ	flux nJy	mag AB	M_{UV}	axis ratio	radius pc
LTM	113	0.027	8400^{+33600}_{-2400}	6^{+2}_{-5}	$37.0^{+1.7}_{-0.4}$	$-9.8^{+1.7}_{-0.4}$	1500	< 0.09
Glafic ($c = 1$)	69	0.020	6800^{+27100}_{-2000}	7^{+3}_{-6}	$36.8^{+1.7}_{-0.4}$	$-10.0^{+1.7}_{-0.4}$	760	< 0.14
Glafic ($c = 7$)	23	0.020	2200^{+9000}_{-600}	22^{+9}_{-18}	$35.6^{+1.7}_{-0.4}$	$-11.2^{+1.7}_{-0.4}$	930	< 0.21
WSLAP	28	0.036	1500^{+6100}_{-500}	32^{+13}_{-26}	$35.1^{+1.8}_{-0.3}$	$-11.7^{+1.8}_{-0.3}$	580	< 0.33
Lenstool	18	0.026	1400^{+5500}_{-400}	36^{+14}_{-29}	$35.0^{+1.8}_{-0.3}$	$-11.8^{+1.8}_{-0.3}$	560	< 0.36

Table 3.1: Earendel results from each lens model: magnification normalization μ_0, nominal distance D from critical curve, resulting magnification 2μ (sum of two lensed images), delensed flux in HST F110W filter (0.9 – 1.4 μm), delensed F110W magnitude, absolute UV magnitude (1600Å), model axis ratio of lensed image, radius upper limit. 68% confidence limit uncertainties are shown for all quantities.

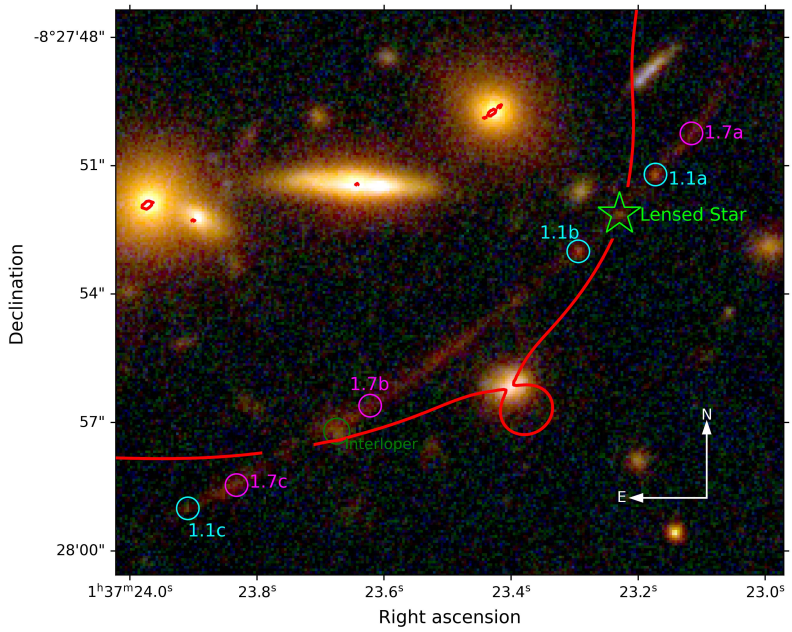

Figure 3.1: The Sunrise Arc at $z = 6.2$ is the longest lensed arc of a galaxy at $z > 6$, with an angular size on the sky exceeding 15 arcseconds. The arc is triply-imaged and contains a total of seven star-forming clumps; the two systems used in lens modeling are circled, with system 1.1 in cyan and system 1.7 in magenta. The highly magnified star Earendel is labeled in green. The best-fit lensing cluster critical curve from the Light-Traces-Mass (LTM) model is shown in red, broken where it crosses the arc for clarity. The color composite image shows the F435W filter image in blue, F606W + F814W in green, and the full WFC3/IR stack (F105W + F110W + F125W + F140W + F160W) in red.

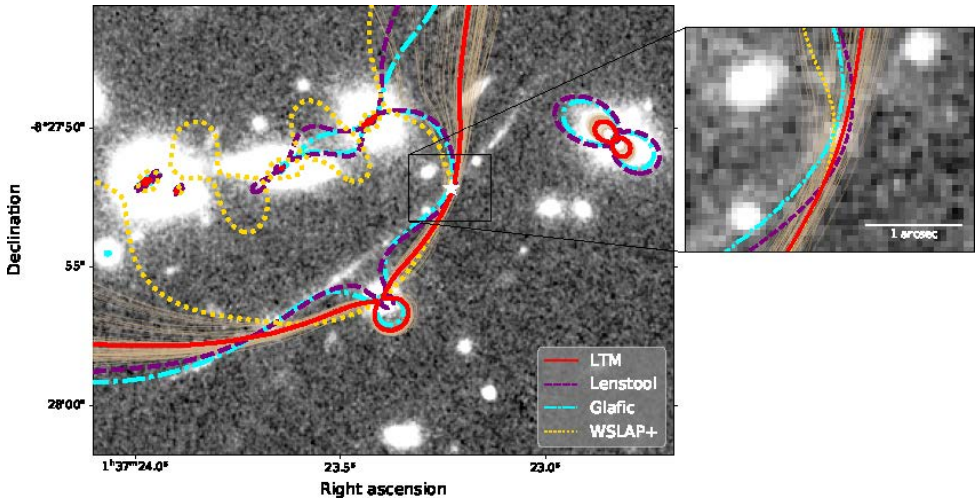

Figure 3.2: Our best-fit lens models all produce critical curves that cross the lensed star Earendel within 0.1″. Additionally, 100 iterations of our LTM model drawn from the MCMC (thin tan lines) are similarly consistent, albeit with greater variance, all crossing the arc within 0.4″ of the lensed star. Critical curves are shown for LTM (red solid), Lenstool (purple dashed), Glafic (cyan dash-dot), and WSLAP+ (yellow dotted).

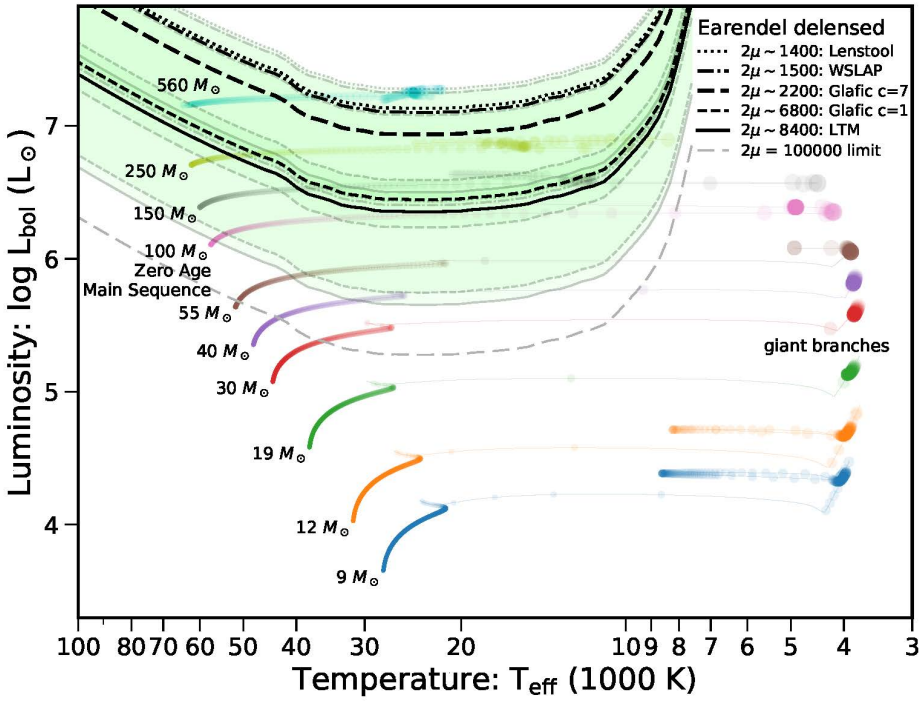

Figure 3.3: Constraints on Earendel's luminosity and effective temperature from *HST* photometry and lensing magnification estimates, shown on an HR diagram alongside BoOST stellar evolution models (colored tracks) for stars with low metallicity ($0.1Z_{\odot}$) (Szécsi et al., 2020). The green shaded region covers the 68% confidence interval of our models. All five lens models are shown, including both Glafic models with concentration $c = 1$ and $c = 7$. The theoretical upper limit magnification $\mu \sim 10^5$ is also shown; it is similar to the 95% limit for LTM. Each stellar model evolution track shows points in time steps of 10,000 years with radii scaling with stellar radius. Our luminosity constraints favor a very massive star.

3.2 Methods

3.2.1 Data

The galaxy cluster WHL0137−08 (RA = 01:37:25, Dec = –8:27:25 [J2000]) was originally discovered as an overdensity of red luminous galaxies in SDSS images (Wen, Han, and Liu, 2012), later confirmed at $z = 0.566$ (Wen and Han, 2015) based on SDSS DR12 spectroscopy (Alam et al., 2015). WHL0137−08 was also ranked as the 31st most massive cluster ($M_{500} \sim 9 \times 10^{14} M_{\odot}$) identified in the Planck all-sky survey PSZ2 catalog (Planck Collaboration et al., 2016) that detected clusters via the Sunyaev-Zel'dovich (SZ) effect on the CMB, or Cosmic Microwave Background (Sunyaev and Zeldovich, 1970).

WHL0137−08 was observed with *HST* as part of the RELICS Treasury program (*HST* GO 14096)(Coe et al., 2019). RELICS obtained shallow imaging of 41 lensing clusters, with single-orbit depth in the ACS F435W, F606W, and F814W optical filters, and a total of two orbits divided between four WFC3/IR filters (F105W, F125W, F140W, and F160W). These observations were split over two epochs separated by 40 days for most clusters, including WHL0137−08 observed 2016-06-07 and 2016-07-17.

Salmon et al., 2020 performed a search for high-redshift galaxies within the RELICS data, and among that sample found the 15″ long arc at $z_{\rm phot} = 6.2 \pm 0.1$, here dubbed the Sunrise Arc. This impressive arc warranted followup imaging with *HST*, which was obtained 2019-11-04 and 2019-11-27 (PI Coe; *HST* GO–15842). This follow-up included an additional 5 orbits of ACS F814W imaging, along with 2 orbits each of ACS F475W and WFC3/IR F110W. These

images were again split over two epochs, this time separated by 23 days. The final image was obtained 3.5 years after the first. These data were co-added to produce a full-depth image, while single epoch images were also produced to allow study of the variability of the star. Images were processed the same way as the original RELICS data (Coe et al., 2019). Total exposure times and limiting magnitudes in each bandpass for our co-added images are listed in Extended Data Table 3.2.

We note that this cluster has also been observed with Spitzer as part of the Spitzer-RELICS program (PI Bradač). An attempt was made to extract IR fluxes from these observations (Strait et al., 2021), however reliable photometry could not be obtained due to blending with brighter cluster member galaxies nearby.

3.2.2 Photometry, Redshift, and SED Fitting

We measured photometry using Source Extractor v2.19.5 (Bertin and Arnouts, 1996) following procedures detailed in Coe et al., 2019. The Sunrise Arc was detected as 18 source segments. We summed the flux measured in all segments, and summed the flux uncertainties in quadrature. Extended Data Table 3.2 provides this total photometry for the Sunrise Arc, along with photometry for Earendel, which we identified as one of the 18 segments.

We discarded the foreground interloper circled in Figure 3.1 from our analysis, based on its slight positional offset, extended size, and colors consistent with a cluster member. Removing the interloper only increases the resulting photometric redshift by 0.1.

We measure the Sunrise Arc's photometric redshift using two methods: BPZ (Benítez, 2000; Coe et al., 2006) and BAGPIPES (Carnall et al., 2018). BPZ uses 11 spectral models (plus interpolations yielding 101 templates) spanning ranges of metallicities, dust extinctions, and star formation histories observed for the vast majority of real galaxies (Coe et al., 2019). BPZ also includes a Bayesian prior on the template and redshift given an observed magnitude in F814W. We allowed redshifts up to $z < 13$. BPZ yields a photometric redshift of $z_{\rm phot} = 6.20 \pm 0.05$ (68% CL) without any significant likelihood below $z < 5.9$ (Extended Data Figure 3.4).

BAGPIPES generates model spectra based on physical parameters, then efficiently searches a large multidimensional parameter space to measure best-fitting parameters along with uncertainties. We ran BAGPIPES fitting simultaneously to redshift and physical parameters as detailed in Strait et al., 2021. Our choices do not significantly affect the photometric redshift, but we summarize them here. We used synthetic stellar populations from BPASS v2.2.1 (Eldridge et al., 2017) with nebular reprocessing and emission lines added by the photoionization code CLOUDY (Ferland et al., 2017). We used a delayed star formation history that initially rises then falls via $SFR(t) \propto t\, e^{-t/\tau}$. We use the BPASS IMF "imf135_300": Salpeter, 1955 slope $\alpha = -2.35$ for $0.5 < M/M_{\odot} < 300$, and a shallower slope of $\alpha = -1.3$ for lower mass stars $0.1 < M/M_{\odot} < 0.5$. In our BAGPIPES modeling of the Sunrise Arc, we left redshift as a free parameter ($z < 13$), along with dust (up to $A_V = 3$ mag), stellar mass ($10^6 - 10^{14} M_{\odot}$), metallicity ($0.005 - 5\ Z_{\odot}$), ionization parameter ($2 < log(U) < 4$), age (from 1 Myr up to the age of the universe), and SFR

exponential decay time τ (100 Myr – 10 Gyr). Dust extinction is implemented with the Calzetti et al., 2000 law, and we assume twice as much dust around all HII regions in their first 10 Myr.

The resulting best fit and redshift likelihood distribution are shown in Extended Data Figure 3.4. BAGPIPES yields a redshift estimate $z = 6.24 \pm 0.10$, similar to the BPZ result without any significant likelihood at lower redshifts. We tried explicitly exploring lower redshift $z < 4$ solutions, including old and/or dusty galaxies with intrinsically red spectra that can result in photometric redshift degeneracies for some high-redshift galaxies. But in our case, none of those red spectra can reproduce the flat photometry observed for the Sunrise Arc in the near infrared (1.0 – 1.6 μm).

BAGPIPES further yields estimates of the dust $A_V = 0.15 \pm 0.10$ mag and mass-weighted age 135 ± 60 Myr, but no strong constraints on metallicity or ionization parameter. Any estimates of stellar mass and SFR include uncertainties due to the lensing magnification. But simply adopting a fiducial magnification of 300 for the full arc from the LTM model, we estimate a stellar mass $\sim 10^{7.5 \pm 0.2} M_\odot$ and current SFR $\sim 0.3 \pm 0.1\ M_\odot\ \mathrm{yr}^{-1}$, not including magnification uncertainties.

3.2.3 Variability

Microlensing simulations suggest that the magnification, and thus observed flux, of Earendel should remain relatively constant over time. However, some variation is expected as the star traverses the microlensing caustic network. A factor of 1–3 difference in observed flux would be expected given these

simulations (see §3.2.6.2).

To assess the variability of the star, we study the four available epochs of *HST* imaging separately. Images from each epoch are shown on the left in Extended Data Figure 3.5, where Earendel is circled in green. Each image shows 1 orbit of WFC3/IR imaging: for RELICS, this is a WFC3/IR stack F105W+F125W+F140W+F160W, while the follow-up imaging consists of F110W. Our analysis is complicated by the fact that RELICS and the follow-up imaging did not use the same WFC3/IR filters. We measure 49 ± 4 nJy in the F110W imaging (sum of epochs 3 and 4) and derive a single value 35 ± 9 nJy in RELICS (epochs 1 and 2) from a weighted average of the fluxes measured in the four WFC3/IR filters. The results are shown as horizontal bands in Extended Data Figure 3.5, along with the fluxes measured in each filter individually. Note summing only the RELICS filters F105W+F125W (closest to F110W) yields 34 ± 15 nJy, similar to the result from the full stack with larger uncertainty.

We find that the IR flux may have varied by a factor of ~ 1.4 across the epochs. However, the large uncertainties on our measured flux values mean that this number is consistent with no variation. Thus we conclude that we see no significant variation across our observations. This low level of variation is consistent with our microlensing simulation results. Future observations with *HST* and *JWST* will further explore the variability of this highly magnified object.

3.2.4 Lens Modeling

The Sunrise Arc is a highly magnified system, and the lensed star Earendel was identified by the large magnification given by our best fit lens models. Strong lensing magnifications have steep gradients in the vicinity of lensing critical curves, so to evaluate the validity of our interpretation of the arc and lensed star we have taken great care in modeling the lensing cluster. We have constructed a total of five lens models using four independent modeling programs, LTM (Zitrin et al., 2009; Zitrin et al., 2015; Broadhurst et al., 2005), Lenstool (Jullo et al., 2007; Jullo and Kneib, 2009), Glafic (Oguri, 2010), and WSLAP+ (Diego et al., 2005; Diego et al., 2007).

We utilized a total of three sets of multiple images in our lens model optimization. The multiple image systems are highlighted in Extended Data Figure 3.6, with each arc shown in detail within that figure. System 1 is the Sunrise Arc at $z_{\rm phot} = 6.2$, and system 2 consists of three images of a bright blue knot at $z_{\rm phot} = 3.1$. Within the Sunrise Arc, we use two sets of multiple images, labeled 1.1 and 1.7. Positions of multiple images 1.1 and 1.7 are defined using the F110W data, as this filter has the strongest detections for each component of the arc (SNR ranges from 7 for the faintest feature to over 20 for the brightest). 1.1 is a compact star-forming clump within the galaxy. Two of the images of 1.1 bracket the star, and are themselves highly magnified. The third image appears much fainter at the southeastern end of the arc. The apparent difference in surface brightness between these clumps is due to the fact that all three are unresolved. This fainter third image was not included in the Glafic models, while it was included in the LTM, Lenstool,

and WSLAP+ models. Comparisons with LTM and Lenstool models made without including this third image show insignificant deviation from models including the third image, indicating that it may not be critical to include when our other constraints are used. The images of 1.7 consist of a clump near the opposite end of the arc. This clump is closer to the center of the host galaxy, and so it is harder to pick out among the flux of the host galaxy. However, our lens models support its positioning, and it allows us to include the full length of the arc in the lens model optimization by including a positional constraint at each end. No additional counter-images of the arc are predicted by our lens models.

Cluster member galaxies were selected via the cluster red sequence (Ellis et al., 1997; Stanford, Eisenhardt, and Dickinson, 1998). We selected galaxies along the cluster red sequence in two colors, (F435W – F606W) and (F606W – F814W). We also included a redshift selection, only including galaxies in the range $0.35 \leq z_{\text{phot}} \leq 0.8$, bracketing the cluster redshift of $z_{cluster} = 0.566$. After selecting galaxies that fit these criteria, we performed a visual inspection to confirm or remove cluster members based on morphology. Finally, we chose to include two small galaxies near the Sunrise Arc which are more questionable cluster members. These small galaxies, marked as C and D in Extended Data Figure 3.6, may be small cluster members or background galaxies, and would normally have been too faint to include in our lens models. They are only included here due to their proximity to the arc, and thus their increased potential to impact the lens magnification in this region. Their questionable status as cluster members led us to leave them to be freely

optimized in the LTM and `Lenstool` models, while galaxy C was excluded from the WSLAP+ model. This galaxy is given low mass in other models (downweighted relative to its observed magnitude), so its exclusion from the WSLAP+ model causes only minor changes in the shape of the critical curve.

3.2.4.1 Light-Traces-Mass Lens Model

The primary lens model used for this analysis was created using the Light-Traces-Mass (LTM) method (Zitrin et al., 2009; Zitrin et al., 2015; Broadhurst et al., 2005). As the name suggests, the LTM method assumes that light approximately traces mass within the lensing cluster. Each cluster member is assigned a power-law mass density distribution, with the overall scaling proportional to the measured flux of the galaxy. The sum of these galaxy-scale masses is then smoothed with a Gaussian kernel of variable width to represent the cluster-scale dark matter distribution. This simple description of the lens allows a rudimentary lens model to be created without multiple image constraints set, as mass is assigned based on cluster member positions and fluxes. Multiple image candidates can then be checked against the initial lens models, which in turn are iteratively refined.

In this case, we began with the a priori assumption that the Sunrise Arc consisted of two images of a single source galaxy, reflected once across the critical curve. However, initial models disfavored this interpretation, and some exploration revealed that a triply imaged galaxy was the only way to reproduce the full length of the arc. The other multiply imaged system at $z \sim 3$ was initially assumed to be triply imaged, with three clear knots showing

similar photometry and morphology. These knots were confirmed by the exploratory LTM models.

After the initial explorations solidified our interpretation of the multiple image constraints, we optimized the model using the standard LTM minimization algorithm. Briefly, the distances between true multiple image locations and model-predicted positions are minimized using a χ^2 function. The minimization is done with a Monte-Carlo Markov Chain (MCMC) using a Metropolis-Hastings algorithm (Hastings, 1970).

During optimization, we allowed the relative weights of six galaxies (circled in Extended Data Figure 3.6) to be freely optimized. This allows the model additional freedom where needed. Each free galaxy is allowed to vary individually in brightness (and thus mass) by a factor ranging from 0.5 to 3 with a flat prior. The brightest cluster galaxy (BCG) is left free as standard. Beyond that, we allow the two bright cluster members near system 1 (labeled A and B in Extended Data Figure 3.6) to vary due to their proximity to our multiple image constraint. Similarly, the relative weights of the galaxies labeled C and D were left free due to their proximity to the Sunrise Arc. Additionally, the membership status of these galaxies is uncertain, as described above. Allowing their weights to vary effectively covers the range of possibilities, from these being true cluster members to unrelated background galaxies. Finally, galaxy E appears to be a spiral disk galaxy viewed edge-on. Such galaxies follow a different mass-to-light ratio than elliptical galaxies, so allowing it to vary accounts for this difference. Relative galaxy weights in the best fit model range from 0.8 to 2.2.

In addition to the multiple image constraints described above, we added flux constraints from the bright knots bracketing the star, and added parity constraints to all image systems. The flux constraint helps to pinpoint the location of the critical curve crossing, which is of critical importance to our analysis of this object. The parity constraints serve to counteract the proximity of our multiple images. Since our images are separated by as little as $1''$, the MCMC optimization often found solutions with a single image appearing near the midpoint of the arc. While this does provide a low χ^2, it is clear that the relensed images do not look anything like the true arc. The parity constraint requires that the critical curves pass between multiple images, giving them opposite parity. If this constraint is not met, a penalty is added to the χ^2 function, allowing the model to avoid these local minima and find the true solution.

The LTM model provides the most accurate reconstruction of the full length of the Sunrise Arc, thus it is the one we take as our overall best fit model.

3.2.4.2 `Lenstool` Lens Model

The accuracy of the cluster lens model is of critical importance to our analysis of this object. Therefore, in order to confirm that our lensing interpretation is correct, we modeled the cluster lens using additional independent software packages. The secondary package used in this analysis was the Lenstool lens modeling software (Jullo et al., 2007; Jullo and Kneib, 2009).

Lenstool is a parametric model that utilizes a MCMC method to sample the model parameter space. The model assigns pseudo-isothermal elliptical

mass distributions (PIEMD) (Limousin, Kneib, and Natarajan, 2005) to both the cluster-scale dark matter halo as well as to individual cluster member galaxies. The total mass distribution is a superposition of the cluster-scale mass distribution and the smaller galaxy-scale masses. Each PIEMD model has seven free parameters: the position (x, y), ellipticity, position angle, core radius r_{core}, truncation radius r_{cut}, and the effective velocity dispersion σ_0. Note σ_0 is not precisely the observed velocity dispersion; see Elíasdóttir et al., 2007 for details.

Six of the seven parameters of the PIEMD model are left free to be optimized, with the exception being the cut radius as this is not well constrained by strong lensing data alone. To keep the total number of parameters from getting too large, the parameters for the galaxy-scale masses are determined by their photometric properties, assuming a constant mass-to-light ratio. This is done using scaling relations for the velocity dispersion $\sigma_0 \propto L^{1/4}$ and truncation radius $r_{cut} \propto L^{1/2}$. The constants of proportionality are optimized freely, while the positions, ellipticities, and position angles are all fixed to what is measured photometrically using Source Extractor (Bertin and Arnouts, 1996).

In our modeling, we choose to leave several key galaxies free to have their velocity dispersions and radii freely optimized. These free galaxies are highlighted in Extended Data Figure 3.6. As mentioned above, the spiral galaxy (E) does not follow the same M/L relation as cluster elliptical galaxies, and is therefore left free. We again leave the two small, white galaxies near the arc (C, D) free both because of their proximity to the arc, and because of their questionable status as cluster members. If these are not part of the cluster,

their effect on the lensing of the arc will be much less, so we account for that by allowing their masses to vary. Finally, two galaxies are left free near the $z \sim 3$ system (A, B). Each free parameter is assigned a Gaussian prior centered on the parameter value given by the above scaling relations. The velocity dispersion priors are given a width of 15 km/s, and priors on radius are given a width of 5 kpc. Best fit values all fall within $\sim 2.5\sigma$ of the original value.

3.2.4.3 Glafic Lens Model

The Glafic model used here was made using the publicly available Glafic lens modeling code (Oguri, 2010). Glafic adopts a parametric lens modeling approach in which the lensing mass is built of multiple components, each defined by a small number of parameters (position, mass, ellipticity, and position angle). Cluster member galaxies are modeled with PIEMD mass models, while the larger cluster-scale potential is modeled with two NFW halos (Navarro, Frenk, and White, 1996) placed at the positions of the brightest and second brightest cluster member galaxies. To reduce the total number of parameters in this model, the member galaxies are assumed to scale with luminosity, such that the velocity dispersion $\sigma \propto L^{1/4}$, and the truncation radius $r_{cut} \propto L^{\eta}$ with η being fixed to 1 for simplicity. The normalizations of these scaling relations are left as free parameters. The ellipticities and position angles of the member galaxies are fixed to values measured from the images using Source-Extractor (Bertin and Arnouts, 1996). The parameters of the lens model are optimized using a MCMC.

3.2.4.4 WSLAP+ Lens Model

The final lens modeling package used in our analysis is the hybrid parametric/non-parametric WSLAP+ code (Diego et al., 2005; Diego et al., 2007). This modeling program divides the cluster mass distribution into a compact component associated with cluster member galaxies, and a diffuse component representative of the cluster dark matter halo. The compact component assigns mass to cluster galaxies based on their luminosity via a mass-to-light (M/L) scaling ratio. This scaling is fit to a single value for the ensemble of cluster members during the optimization process.

The diffuse mass component is defined as the superposition of Gaussians on a grid. These grid cells map the mass at any given point in the cluster, and are optimized in conjunction with the compact galaxy masses. This non-parametric aspect of WSLAP+ gives it more freedom to assign mass where a parametric model (such as LTM or Lenstool) might not.

Such non-parametric models probe a broader range of solutions, often allowing larger uncertainties for measured quantities (Meneghetti et al., 2017). However, the increased freedom of this type of lens model can more readily fit atypical mass distributions, meaning it is more likely to span the true solution, particularly when the underlying mass distribution deviates from our typical mass-to-light assumptions. In this case, the increased freedom can determine if such an atypical mass distribution could explain our observations as a moderately magnified cluster of stars rather than a single star.

Instead, we find that the WSLAP+ model agrees with our parametric models, with the $z = 6.2$ critical curve crossing within $0.1''$ of Earendel in

all models. This supports our interpretation of Earendel as an extremely magnified single star.

3.2.5 Magnification and Size Constraints

Using the various lens models, we constrain Earendel's magnification and delensed properties as summarized in the main text. Based on observing a single unresolved image, we place upper limits on Earendel's radius and distance from the critical curve as illustrated in Extended Data Figure 3.7.

First, we model the source as a Gaussian light profile with a width σ that we refer to as the radius r (e.g., 0.1 pc). Then we stretch this Gaussian along the arc for a given model magnification $\mu = \mu_{\parallel}\mu_{\perp}$ and axis ratio $\mu_{\parallel}/\mu_{\perp}$ where the tangential magnification $\mu_{\parallel} = 1/(1-\kappa-\gamma)$ and perpendicular magnification $\mu_{\perp} = 1/(1-\kappa+\gamma)$ for a lens model mass κ and shear γ at a given position (note this is normally referred to as radial magnification as defined with respect to the BCG. However that would be confusing in this context where Earendel's radius is magnified most significantly by the tangential magnification $\mu_{\parallel} \sim 1000$, and much less so by the perpendicular or radial magnification $\mu_{\perp} \sim 1.1 - 2.1$). In practice, for each model we measure $\mu_{\perp}$ near Earendel (it varies slowly) and μ_0 from fitting $\mu = \mu_0/D('')$. Then the observed lensed radius along the arc would be $R = \mu_{\parallel} r = \mu_0 r/D('')\mu_{\perp}$. We convert the magnified radius to image pixels via $1'' = 5.6$ kpc (at $z = 6.2$). Note the resulting lensed image is approximately a 1D Gaussian line (stretched almost entirely tangentially along the arc) convolved with the HST WFC3/IR F110W PSF (point spread function).

Then by analyzing the HST images, we determine that a 1D Gaussian with a width of $\gtrsim 0.055''$ would begin to appear spatially resolved. This width is roughly 0.4 native WFC3/IR pixels (each $0.13''$), or ~ 1 drizzled pixel ($0.06''$) in our standard data products. We perform this analysis on a $10\times$ super-sampled image (drizzled to $0.013''$ / pixel) combining the 8 F110W exposures. Given a model of the HST F110W PSF, we first confirm that the image of Earendel is unresolved: consistent with and not measurably wider than the PSF. Then we stretch the PSF diagonally along the arc, finding that it appears unresolved when convolved with a 1D Gaussian with $\sigma = 0.055''$. Combining this upper limit on R with the lens model estimates of μ_0 and $\mu_\perp$, and upper limits on $D('')$ derived below, we determine that Earendel's intrinsic delensed radius is $r < 0.09$ – 0.36 pc, depending on the lens model.

Additionally, the radius upper limit assumes that a hypothetical star cluster would sit centered on the lensing caustic. This configuration would imply that our unresolved object is a merged pair of images, each showing the same half of the source cluster. This specific geometry would require precise alignment of the star cluster with the lens, making it less likely. A more likely geometry would be a hypothetical star cluster appearing entirely on the visible side of the caustic, now creating a merging pair of images of the full cluster. This setup would decrease our radius limits by a factor of two (to $r < 0.045$ pc for LTM through $r < 0.18$ pc for Lenstool), further straining the possibility that this is a star cluster. There is a possibility that we are seeing a small fraction of a larger star cluster, and that the rest of the cluster is hidden behind the caustic. This is also somewhat unlikely, but we cannot rule it out.

Given this radius smaller than known star clusters, we determine Earendel is more likely an individual star or star system. Such systems are significantly smaller and would certainly appear as unresolved. Thus going forward, we assume Earendel's light can be modeled as a point source.

Next we model Earendel as two lensed point sources separated by a distance 2ξ. By analyzing the HST images, we find a similar result: the two images (convolved with the PSF) can be spatially resolved when separated by a distance $2\xi \sim 0.11''$, with $\xi \sim 0.055''$. These lensed images would appear separated along the arc. The lensing critical curve intersects the arc at an angle θ that varies between 22° and 41°, depending on the lens model. The distance from each lensed image to the critical curve is $D = \xi \sin\theta$. Thus, the maximum distance to the critical curve is $D < 0.055'' \sin\theta$, which varies from $D < 0.02''$ to $D < 0.036''$, depending on the lens model.

Given D, we determine the magnification estimate μ from each model and constraints on radius r described above, all summarized in Table 3.1. We note that given the strong lens model constraints (observed multiple image locations), the critical curve can be at any small distance $D < 0.1''$ from Earendel with roughly equal likelihood. This translates to a magnification likelihood $P(\mu) \propto 1/\mu$. We confirm this likelihood distribution in the LTM MCMC posterior range of models. We note microlensing introduces additional scatter and uncertainty, but this is subdominant.

Our upper limits on D (68% confidence) translate to lower limits on μ, given $\mu \propto 1/D$. Here rather than upper limits $D < D_1$, we are more interested in the 68% central confidence range, which is $0.2D_1 < D < 1.4D_1$ assuming

a Gaussian likelihood. Given $\mu \propto 1/D$ and lower limits $\mu > \mu_1$, the corresponding central confidence range is $0.7\mu_1 < \mu < 5.0\mu_1$. For example, at 68% confidence LTM yields either $2\mu > 8400$, or $6000 < 2\mu < 42000$. This statistical uncertainty (a factor of 7) is comparable to the large systematic uncertainty spanned by the various lens models (a factor of 6). LTM yields the highest magnification estimates, while Lenstool yields the lowest: $1000 < 2\mu < 6900$ (see Table 3.1). Thus, rounding slightly, we quote the full uncertainty range as $1000 < 2\mu < 40000$ for Earendel's magnification.

We note we also attempted to measure constraints on radius and separation using a forward modeling technique as in Johnson et al., 2017b. However, this method is limited to the few allowed lens models that each put Earendel at a discrete distance D from the critical curve. In order to determine limits on D, r, and μ, we needed to vary D and R smoothly. Forward model results for each model fell within the allowed ranges derived above.

3.2.6 Microlensing Effects

Previous lensed star discoveries were identified when the magnification, and thus observed brightness, temporarily increased (Kelly et al., 2018; Rodney et al., 2018; Chen et al., 2019; Kaurov et al., 2019). These transients have relied on microlensing, wherein stars bound to the lensing cluster temporarily align with the lensed image(s) of the star, creating a brief boost to the magnification. The relative transverse motions of lensing stars with respect to the lensed star impact the microlensing alignment and lead to the fluctuations observed in previous lensed stars. It is possible to decrease the amplitude of these

microlensing fluctuations if the optical depth of microlenses increases. In situations where the magnification is extreme, microcaustics overlap in the source plane resulting in relatively small fluctuations in the flux every time a microcaustic crossing happens. The more microcaustics overlap, the less effect they have on the observed flux. This “more is less" microlensing effect is observed when the effective optical depth of microlensing is greater than 1 (that is, microcaustics are overlapping each other (Dai, 2021)). In this situation, the observed flux is the sum of the fluxes from all microimages. Since the number of microimages scales with the number of overlapping microcaustics, crossing one microcaustic results in a smaller relative change in the total flux for a larger number of overlapping microcaustics (Dai and Pascale, 2021).

3.2.6.1 Diffuse Light Calculation

Our microlensing simulations depend on the number density of stars in the line of sight to Earendel. These can be a combination of stars or stellar remnants in the wings of cluster member galaxies, and stars or stellar remnants not bound to any galaxy that make up the ICL. To facilitate our microlensing analysis, we measured the cluster stellar mass density in the region around the Sunrise Arc, combining both the ICL and faint wings of cluster galaxies. From the stellar mass density, we can then calculate the number density of stars using an assumed initial mass function.

The full cluster light and ICL modeling analysis of WHL0137−08 is performed by Jiménez-Teja et al., 2021. Here we mostly care about the stellar mass density in the region around the arc, and more specifically around the lensed

star. Thus we focus our measurement on two rectangular regions parallel to the arc, one on each side, extending between the two images of the brightest knot, as shown in Extended Data Figure 3.8. The arc, knots, and star are all masked from the image prior to measurement, but cluster member galaxies are kept as we are interested in the wings of these galaxies as well as the ICL contribution to stellar density in this region. The extent of the arc is defined in the F110W band, as that is the band in which the arc appears brightest.

The fluxes within these apertures are used to fit a stellar energy distribution (SED). The SED fitting is done using the Fitting and Assessment of Synthetic Templates (FAST) code (Kriek et al., 2009). We used stellar population models from Bruzual and Charlot, 2003, along with initial mass functions from both Chabrier, 2003 and Salpeter, 1955 to explore the full range of possible solutions. With this technique, we find a stellar surface mass density of $\Sigma_* \sim 10\ M_\odot \mathrm{pc}^{-2}$, however the uncertainties allow for values as low as $\sim 1\ M_\odot \mathrm{pc}^{-2}$ (see Extended Data Table 3.3). Since low stellar surface mass densities introduce more variability in the flux, we explore two regimes with $\Sigma_* \sim 1\ M_\odot \mathrm{pc}^{-2}$ and $\Sigma_* \sim 10\ M_\odot \mathrm{pc}^{-2}$. Outside this regime, smaller values of Σ_* are unlikely given the observational constraints, and larger values of Σ_* would result in even smaller fluctuations (over time) in the observed flux.

3.2.6.2 Microlensing Simulations

To cover the range of possible diffuse light stellar surface mass densities in our microlensing analysis, we ran two simulations of the effects of microlensing on our observed magnification. One simulation assumed a value

of $\Sigma_* = 10\ M_\odot \mathrm{pc}^{-2}$, while the other assumed a value of $\Sigma_* = 1\ M_\odot \mathrm{pc}^{-2}$. With these two values, we can explore both the high end density estimate, which would produce a denser microlensing caustic network and thus increase the probability that the star would appear at extreme magnification, and the low end estimate which would produce greater variability in the magnification, and a non-negligible probability that one of the two counter-images is unobserved.

Our simulations follow Diego et al., 2018; Diego, 2019 Since we are assuming the two counter-images form a single unresolved image, in order to compute the total flux, we perform two simulations, one with negative parity and one with positive parity. In both cases, the magnification (in absolute value $|\mu|$) is the same and equal to half the total magnification of the pair of counter-images of the star (2μ). We force the two magnifications to be the same (but opposite sign) by changing slightly the values of κ and/or γ. The total flux at a given moment is given by the superposition of two tracks, one for the simulation with positive parity and one for the simulation with negative parity. Both tracks are forced to have the same orientation with respect to the cluster caustic. The very small scale fluctuations observed in the tracks are due to shot noise in the ray-tracing process.

In the simulation, microlenses are assumed to be point-like, with masses drawn from the mass functions of Spera, Mapelli, and Bressan, 2015 The mass function is normalized to match our stellar surface mass density measurements around the star. These microlenses are then distributed randomly across a circular region of radius 10 mas, in a lens plane that has a resolution of 20

nas per pixel. For the smooth component, or macromodel, we impose the constraint that the total convergence and shear from the macromodel and the stellar component is consistent with our lens models. The convergence from the smooth component is such that the total magnification is $2\mu \approx 9000$, when the flux from both counter-images is combined into a single unresolved source. In particular, the convergence in the smooth model is determined after fixing the total magnification of each counter-image as $\mu = \mu_{\parallel}\mu_{\perp}$, where $\mu_{\parallel}$ and $\mu_{\perp}$ are the tangential and perpendicular magnifications, respectively. This results in a total average magnification (when integrating over long periods of time) of $2\mu = 8960$, close to the desired fiducial value $2\mu = 9000$.

The magnification in the source plane is then built through a standard ray-tracing method. The resulting pattern is shown in Extended Data Figure 3.9.

To measure the fluctuations over time, we assume the star is moving at a velocity $v = 1000$ km s^{-1} ~ 0.001 pc/yr relative to the caustic network(Kelly et al., 2018; Oguri et al., 2018). This velocity estimate accounts for rotation of the lensed galaxy, motions of stars and galaxies within the cluster lens, and relative transverse velocities between the cluster lens, lensed galaxy, and Earth with respect to the Hubble flow. Windhorst et al., 2018 test whether 1000 km s^{-1} is reasonable by adding random space motions of up to several thousand km s^{-1} to well-studied clusters and measuring the effect on the cluster redshift space distributions, finding velocities of $\sim$ 1000 km s^{-1} do not distort the observed cluster properties. Thus we infer that this velocity is reasonable in our case. Ultimately, the exact velocity assumed will impact only the duration and frequency of microlensing events, with little to no effect on

their amplitude. The direction the star moves relative to the caustic network also impacts the expected variability in magnification. If the star were moving perpendicular to the cluster caustic, we would expect the greatest variation in time, whereas if the star were to move parallel to the cluster caustic we expect much less variation. For our analysis, we assume the star is moving at an angle of 45° relative to the cluster caustic. This will produce moderate fluctuations in time, with the star typically staying within a factor of two of our measured brightness. As with the velocity, the direction will only impact the duration and frequency of magnification fluctuations. Because we are in a microlensing regime with a larger effective optical depth (> 1), microcaustics will overlap and limit the amplitude of variations as the star traverses this caustic network. Thus no matter what velocity and direction we assume, the star will most likely stay within a factor of two of its current magnification, matching our observations.

Extended Data Figure 3.9 shows simulated light curves and likelihoods for both microlensing stellar densities $\Sigma_* = 1$ and 10 $M_\odot \mathrm{pc}^{-2}$. The higher stellar density reduces the variability in flux as the microlensing caustic network saturates, yielding a consistently high magnification $2\mu \sim 9000$. In this case, we can expect with $\sim$65% confidence that magnifications measured 3.5 years apart will be within a factor of 1.4, as observed. If the stellar density is lower (1 $M_\odot \mathrm{pc}^{-2}$), this likelihood decreases to $\sim$40%, which is still fairly likely. Therefore, both of these predictions are consistent with our observations.

We also tested a third "critical" scenario with maximal time variations and found these very similar to the results for $\Sigma_* = 1 M_\odot \mathrm{pc}^{-2}$. The degree

of variability depends on the product $\mu\Sigma_*$. Our simulations had $\mu\Sigma_* =$ 44800, 4480, and finally 1600 for the critical case. Tighter constraints on *both* parameters μ and Σ_* are required to improve variability predictions. Future observations will better constrain these parameters while providing better data on variability or lack thereof. An approved upcoming *HST* program (GO 16668; PI Coe) will add time monitoring observations to test these predictions and more precisely constrain the baseline flux.

3.2.7 Luminosity and Stellar Constraints

From our magnification measurements of $\mu = 1000$ – 40000 derived above, and Earendel's observed flux 49 ± 4 nJy in the *HST* F110W filter (0.9 – 1.4 μm), we calculate a delensed flux of 1 – 50 pJy, corresponding to an AB magnitude of 38.7 – 34.7. This then gives an absolute UV (1600Å) magnitude of $-8 < M_{AB} < -12$, given the distance modulus 48.9 at $z = 6.2$ and flux per unit frequency dimming by $1 + z$ (2.1 mag). We can then calculate the intrinsic stellar luminosity, assuming blackbody spectra for hot stars with effective temperatures $T_{\rm eff} > 40000$ K. For cooler stars, we used the lowest surface gravity models available from the grid of empirically-corrected [M/H] $= -1$ stellar atmosphere spectra compiled by Lejeune, Cuisinier, and Buser, 1997. This yields the black tracks in Figure 3.3 for a given magnification and delensed flux. Green shaded regions show magnification uncertainties (factor of 7 for each individual lens model); the photometric uncertainties are 10% (insignificant and thus not included). We also explored the effects of different metallicity stellar atmosphere models (from [M/H] = 0 to -5 using Lejeune,

Cuisinier, and Buser, 1997), and found $\Delta \log L < 0.1$ for $T_{\rm eff} > 10000$ K, and $\Delta \log L \sim 0.2$ for $T_{\rm eff} < 10000$ K, which is insignificant compared to our other uncertainties. The redshifted spectrum of a B-type star with temperature $\sim$20000–30000 K maximizes the flux in the F110W filter, whereas spectra of hotter / cooler stars require a higher total bolometric luminosity to produce the same F110W flux.

For our calculations of the stellar luminosity, we assume zero extinction due to interstellar dust. With current data, we cannot robustly estimate the extinction around the star. While BAGPIPES yields an estimate of $A_V = 0.15 \pm 0.1$ mag for the full galaxy, we would expect less dust in the ISM near the outskirts of the galaxy where we see the star. On the other hand, we would expect this massive star to still be associated with a star forming region, which would increase the expected dust extinction. To get a rough estimate of the effect of dust, we can assume we have $E(B-V) \sim 0.1$ mag in the region surrounding the star (reasonable for a star cluster in a low-metallicity galaxy(Calzetti et al., 2015)), and an SMC-like extinction law with $R_V \sim 2.93$. With these assumptions, we would expect a factor ~ 2 reduction in flux. This would lead to an equivalent increase in the inferred luminosity. While this is significant, it is still far less than the large magnification uncertainty.

In Figure 3.3, we show low-metallicity ($0.1 Z_\odot$) dwarf galaxy predictions from BoOST, as may roughly be expected at $z \sim 6$ based on simulations (Shimizu et al., 2016). There is considerable scatter in galaxy metallicities in both observations and simulations. Additionally, the star is not necessarily

at the same metallicity as the galaxy overall. To probe the effects of metallicity on our interpretation of the mass of Earendel, we consider a range of stellar tracks from BoOST with varying metallicities. These range from solar metallicity $Z_\odot$ down to $0.004Z_\odot$, the full range available from BoOST models. These tracks, along with a green shaded band showing our full luminosity uncertainty across all lens models, is shown in Extended Data Figure 3.10. The differences between various low-metallicity tracks are small relative to our current uncertainties, so the exact choice of metallicity does not impact our conclusions; we still find massive stars best match our constraints. A more important uncertainty is in the stellar modeling of massive stars, which radiate near the Eddington limit. In such stars, the expansion of their outer layers is poorly understood, leading to increased uncertainty on predictions of stellar radii and effective temperatures (Sanyal et al., 2015). The luminosity of the star is not impacted by this uncertainty, so these models still provide a useful estimate of the mass of the star.

In Extended Data Figure 3.11, we show the BoOST $0.1Z_\odot$ stellar evolution tracks vs. time. We see that very massive stars of $100M_\odot$ or more spend the greatest time ($\sim$ 2 Myr) with a luminosity matching Earendel within the uncertainties. The next less massive track $\sim 55M_\odot$ would only match our luminosity constraint for $\sim$ 0.5 Myr. This shorter time would decrease the probability of observing such a star by $\sim 1/4$. On the other hand, lower mass $55M_\odot$ stars may be roughly 4 times as numerous as $100M_\odot$ stars, depending on the IMF. From this simple analysis, we estimate that Earendel's light may be most likely generated by a star with $\sim 50 - 100M_\odot$. More massive stars

are less likely because they are less numerous, while a less massive star would not be bright enough. Given the large uncertainties on our observational constraints, we leave more detailed analysis of lifetimes, formation rates, and magnification probabilities for future work.

Such massive stars are rarely single (Sana et al., 2012; Sana et al., 2014). Multiple less massive stars could also combine to produce the observed luminosity. While it is most likely that a single star will dominate the light in such a system, there is a possibility of finding tightly bound multiple systems of similar masses, and thus similar brightnesses. El-Badry et al., 2019 find a sharp excess of "twin" systems, with a mass ratio $\gtrsim 0.95$ indicating that the stars are roughly equal masses. This analysis was restricted to lower mass stars, but Moe and Di Stefano, 2017 find a similar (although more modest) excess for more massive systems. Additionally, Moe and Di Stefano, 2017 find that the fraction of stars in triple and quadruple systems increases as the primary star's mass increases, up to a quadruple fraction of $\sim 50\%$ for stars of mass $\sim 25 M_{\odot}$. In any case of a twin/triple/quadruple star, the contribution from companion stars becomes non-negligible. This would effectively reduce the inferred mass of the primary star, potentially down to $\sim 20 M_{\odot}$ in the case of a quadruple system of equal mass main sequence stars. We note that multiple bright stars would also dampen microlensing variations, as one star may be crossing a microcaustic while others are not, further supporting our observation of relatively stable flux.

With the *HST* photometry available, we cannot reliably distinguish between different stellar types and effective temperatures, and thus stellar mass.

We have multi-band imaging, but only the F110W band has a reliable ($> 5\sigma$ significance) detection. Other WFC3-IR bands do detect the star, but at much lower significance, the highest being F160W with a $\sim 3\sigma$ detection. Additionally, these other IR bands were taken in the original RELICS imaging. The 3.5 year gap between observations provides ample time for the magnification to vary considerably. Our microlensing analysis suggests that the magnification will stay high ($\mu \geq 1000$) for many years, but fluctuations of a factor of 2 are expected.

ACS/F814W imaging was obtained in every epoch of observations, however the stacked detection in this band is still only at 4.4σ confidence. Additionally, this bandpass spans the Lyman-α break at $z \sim 6$, so the F814W flux is primarily a function of redshift: more flux drops out as redshift increases up to $z = 7$. Any SED constraint from *HST* photometry would be weak. Future spectroscopic observations with our approved JWST program (GO 2282; PI Coe) will determine the type and temperature of this star, placing it on the H-R diagram.

3.2.8 Probability of Observing a Massive Star

In the following, we assess the probability of observing a lensed star with $M_* \gtrsim 100 M_\odot$ at sufficiently high magnification to be detected in our data. To do so, we use our model of the Sunrise Arc to estimate the total star formation rate (SFR) of the host galaxy within a region close to the lensing caustic, and use assumptions on the stellar IMF to convert this into an estimate on the number of high-mass stars within this area. Using the formalism presented

by Diego, 2019, and fitting for necessary constants using our LTM lens model, we calculate a source plane area of ~ 500 pc^2 (~ 0.5 pc perpendicular to the caustic times ~ 1000 pc along the caustic) that intersects the host galaxy at a magnification of $2\mu \gtrsim 4200$ (set by the minimum magnification to detect a $M_* \sim 100\ M_\odot$ star in our data). We next estimate the surface brightness of the arc close to the location of the star, finding $I \sim 6 \times 10^{-6}$ nJy pc^{-2}. By assuming that the surface brightness of the host galaxy remains approximately constant along the caustic, we may then convert surface brightness to total SFR within the $2\mu > 4200$ region that intersects the host galaxy. Using Starburst99 v.7.0.1 (Leitherer et al., 1999) under the assumption of a Kroupa, 2001 IMF throughout the 0.01–120 $M_\odot$ interval and a constant-SFR stellar population with $Z = 0.001$ at age 100 Myr, we find a total $SFR \sim 2 \times 10^{-4}\ M_\odot$ yr^{-1} in the host galaxy region magnified by $2\mu > 4200$.

We next calculate the probability of observing a star of mass $\geq 100\ M_\odot$ at this SFR. This is done with two star formation prescriptions, one assuming clustered star formation wherein stars are distributed into star clusters with a cluster mass function $\mathrm{d}N_{\mathrm{cluster}}/\mathrm{d}M_{\mathrm{cluster}} \propto M_{\mathrm{cluster}}^{-2}$ between $20 - 10^7\ M_\odot$, then randomly sampled from the IMF with the limit $M_* < M_{\mathrm{cluster}}$ using the SLUG v2.0 code (da Silva, Fumagalli, and Krumholz, 2012; Krumholz et al., 2015). This tends to result in fewer high mass stars. The other possibility is unclustered star formation, in which stars are randomly sampled from the IMF without first being split into clusters. This method results in a greater proportion of massive stars. From this calculation, we find a probability $P(\geq 100 M_\odot) \sim 2\%$ in the clustered scenario, and $\sim 4\%$ in the unclustered

scenario.

From this calculation, we conclude that one might expect to find such a massive, lensed star in about 1 in 25–50 such caustic crossing galaxies. Tens of galaxies like this have been observed in *HST* images from various programs. Therefore, the probability of such a discovery is reasonable.

We note that a different choice of IMF over the stated mass range could impact the calculated SFR, up to a factor ~ 1.5 if we were to use the Salpeter, 1955 IMF (Madau and Dickinson, 2014). However, this change will be largely canceled out by the lower probability per unit stellar mass of forming $> 100 M_{\odot}$ stars using the Salpeter IMF. The difference if we were to use a Chabrier, 2003 IMF would be even smaller, as that is more similar to the Kroupa IMF over our mass range. Ultimately, any uncertainty introduced by the choice of IMF will be sub-dominant compared to other assumptions, such as the assumed metallicity. However, if the stellar IMF would be more top-heavy than the Kroupa IMF (i.e., contain a larger fraction of massive stars), as has been argued to be the case for star formation in low-metallicity environments (Kehrig et al., 2018), then the probability for detecting a $\geq$ 100 $M_{\odot}$ star could be significantly higher. The probability would also increase in scenarios where the host galaxy, despite being metal-enriched, contains a fraction of Pop III stars, as in the simulations by Sarmento, Scannapieco, and Cohen, 2018; Sarmento, Scannapieco, and Côté, 2019. From the MESA mass-luminosity relation of such stars, Windhorst et al., 2018 showed that most of their light comes from $20 - 200$ $M_{\odot}$ stars, so that finding a single ~ 100 $M_{\odot}$ star during a significant caustic magnification is possible.

3.2.9 Alternative Possibilities

There are a few alternative possibilities we consider for this object. One such possibility is that Earendel is a Population III star with zero metallicity. Calculations of observable properties of Pop III stars from MESA stellar evolution models show that a $> 50 M_{\odot}$ in a hydrogen-depleted phase would match our delensed flux constraint, as would a ZAMS star of $> 300 M_{\odot}$ (Windhorst et al., 2018).

The lifetime of a massive Pop III star would be short relative to its host galaxy. It would therefore require a pristine zero-metallicity environment within the host galaxy to form. Such regions become less common as more early generation stars explode and enrich their surroundings with heavier elements. Our SED fitting of the Sunrise Arc gives a stellar mass of $M_{*} \sim 3 \times 10^{7} M_{\odot}$, from which we might expect a metallicity on the order of $0.01 Z_{\odot}$ or $0.1 Z_{\odot}$ (Shimizu et al., 2016). This non-zero metallicity would indicate that some enrichment has taken place. Even if we assume the galaxy overall has been enriched, finding a Pop III stellar population is not ruled out. Some models predict that pockets of zero-metallicity gas (from which Pop III stars can form) may still exist at $z \sim 6$, particularly near the outskirts of galaxies (Trenti, Stiavelli, and Shull, 2009). Observationally, Vanzella et al., 2020 report a strongly lensed star cluster consistent with being a complex of Pop III stars at $z = 6.6$. In this case, pockets of zero-metallicity stars may exist in otherwise metal enriched galaxies. Spectroscopic follow-up will be required to assess the possibility of Earendel being a Pop III star.

Although the probability of Earendel being a zero-metallicity Pop III star

is low, if it turns out to be such an object it would be the first such star observed. This would provide important confirmation that such stars formed, and would offer an incredible opportunity to study one in detail. Furthermore, such a star is a possible progenitor for the recently observed binary black hole merger GW190521, which is too massive to be explained by standard stellar remnants (Abbott et al., 2020). Recent studies (Farrell et al., 2020; Kinugawa, Nakamura, and Nakano, 2020) have proposed that extremely metal poor or zero metallicity stars are viable progenitors for this event. Finding such a star would offer a chance to study it in detail and refine models of how these stars collapse into black holes.

Another possibility is that this object is an accreting stellar mass black hole. If the black hole were persistently fed by a lower mass star overfilling its Roche lobe, it could continue to shine up to 60 Myr (Windhorst et al., 2018). Note we assume this would be a persistent source. A transient outburst, which would shine for weeks to months (Zdziarski and Gierliński, 2004), would be ruled out by the lack of variation observed (see §3.2.3). A stellar mass black hole accretion disk would have strong X-ray emission, whereas a star would not. Following the multicolor accretion disk model in Windhorst et al., 2018, a $200 M_{\odot}$ black hole formed from a $\sim 300 M_{\odot}$ Pop III star would have an inner accretion disk with $T_{max} \sim 7.7$ keV $\sim 3 \times 10^7$ K. Most of the X-ray emission would originate near the center of the disk, from radii around a few times the Schwarzschild radius ($\gtrsim$ 900–1800 km). The maximum possible magnification of the tiny X-ray emitting region could then be substantially (perhaps 100×) larger than that for the rest-frame UV stellar light, or $\mu \gtrsim 10^6$.

Most of the remainder of the accretion disk would shine in the rest-frame UV at the Eddington limit with very similar size, luminosity, and surface brightness as a massive star. Hence, a stellar mass black hole accretion disk would appear very similar in the HST images to a massive star. Analysis of archival X-ray data from XMM-Newton showed no clear signal near this position, supporting the stellar interpretation. We note, however, that the $6''$ spatial resolution of XMM-Newton would dilute the signal from such a black hole accretion disk. Deeper, higher-resolution X-ray images with the Chandra X-ray Observatory (resolution $\sim 0.5''$) or the upcoming Athena mission could conclusively determine if this source is a black hole.

We also consider the possibility that this object is not associated with the Sunrise Arc, and thus not a lensed star at $z \sim 6$. The first possibility would be a local star which happens to align with the background arc. While possible, this is unlikely given the exact alignment of the object with the background arc. Holwerda et al., 2014 found $\sim$ 1.2 M-type dwarfs per arcmin^2 out to magnitude 24 in their analysis of multiple fields observed with HST. Rescaling to 27th magnitude, we estimate we might observe of order $\sim$ 100 such stars per arcmin^2 in our observations. Given the small solid angle surrounding the critical curve crossings in the Sunrise Arc (constrained to within $0.1''$), the probability of one of these local dwarfs aligning with both the arc and critical curve by chance is of order 0.01%. If Earendel were a local brown dwarf, we might see some evidence of proper motion over the 3.5 year observation window. We see no evidence of motion, strengthening the interpretation that this star is associated with the Sunrise Arc. We note that we cannot

conclusively rule out a brown dwarf based on existing *HST* photometry. We fit the SED of Earendel alone to brown dwarf spectra from the SpeX Prism Library (Burgasser and Splat Development Team, 2017), and find that a 3000 K local star could reproduce our observations. We expect upcoming *JWST* photometry and spectroscopy to rule out a brown dwarf conclusively. For now, we rely on the unlikely chance alignment and lack of proper motion to disfavor a local brown dwarf.

Other possibilities to consider for this object are distinct galaxies in the foreground, cluster, or lensed background. But even analyzed independently, Earendel's photometric redshift is the same as the full galaxy: $z = 6.2 \pm 0.1$ (95% CL) with negligible likelihood at lower redshifts according to BPZ given the Lyman break, which is clear even in this faint object. Furthermore, any foreground / lensed background galaxy would most likely appear larger and spatially resolved in the *HST* images. Note a $z < 6$ background galaxy, say at $z \sim 2$, would not be on the lensing critical curve for that redshift, but it would still be magnified by a factor of a few to perhaps tens, requiring a small galaxy to not appear spatially resolved when magnified. A quasar would still appear point-like when lensed, but of course quasars are less numerous and we would expect a redder rest-frame ultraviolet continuum slope (Hainline et al., 2011). Again, we expect upcoming to *JWST* observations to spectroscopically confirm Earendel is a star at $z \sim 6.2$ within the Sunrise Arc galaxy.

Camera	Filter	HST-1 (s)	HST-2 (s)	Depth 5σ (AB mag)	Sunrise Arc Flux (nJy)	Earendel Flux (nJy)
ACS	F435W	2072		27.2	-69 ± 56	-8 ± 12
ACS	F475W		3988	27.9	16 ± 27	9 ± 6
ACS	F606W	2072		27.6	-51 ± 33	-2 ± 7
ACS	F814W	2243	11083	28.0	312 ± 21	19 ± 4
WFC3/IR	F105W	1411		26.7	1321 ± 74	30 ± 14
WFC3/IR	F110W		5123	27.7	1187 ± 21	49 ± 4
WFC3/IR	F125W	711		26.0	1351 ± 137	37 ± 26
WFC3/IR	F140W	711		26.2	1197 ± 109	21 ± 21
WFC3/IR	F160W	1961		26.5	1088 ± 74	46 ± 15

Table 3.2: Hubble imaging of WHL0137-08 in nine filters and photometry measured for the Sunrise Arc and Earendel. Imaging was obtained by RELICS (HST-1: GO 14096) and follow-up imaging 3.5 years later (HST-2: GO 15842). Final 5σ depths for point sources are given in column 5. Fluxes used in SED fitting and plotted in Figures 3.4 & 3.5 are given in column 6 (full arc) and column 7 (Earendel individually), along with 68% confidence uncertainties.

IMF	Stellar Mass Density ($M_\odot$ pc^{-2})
Chabrier	$8\,^{17}_{0.7}$
Salpeter	$15\,^{30}_{1.0}$

Table 3.3: These values include both ICL and the wings of cluster member galaxies. Most likely values are followed by 68% confidence ranges in brackets.

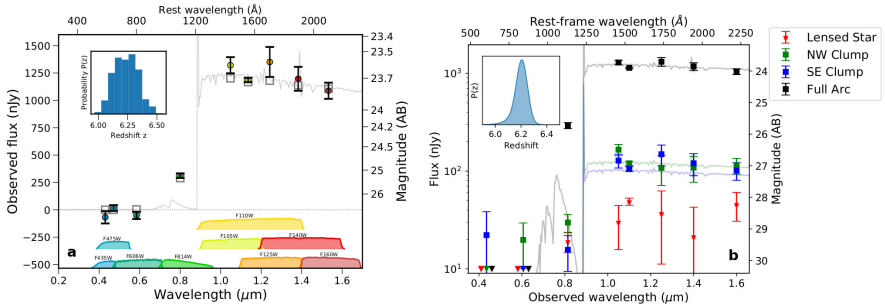

Figure 3.4: a, *HST* photometry with 1σ error bars, SED fit, and redshift probability distribution for the Sunrise Arc using the photometric fitting code BAGPIPES. The arc shows a clear Lyman break feature, and has a photometric redshift $z = 6.24 \pm 0.10$ (68% CL). **b,** *HST* photometry for the full arc (black), clumps 1.1a/b (green/blue), and Earendel (red), with associated 1σ error bars. BPZ yields a photometric redshift of $z_{\rm phot} = 6.20 \pm 0.05$ (inset; 68% CL), similar to the BAGPIPES result. Clumps 1.1a/b have similar photometry, strengthening the conclusion that they are multiple images. Note both BPZ and BAGPIPES find significant likelihood only between $5.95 < z < 6.55$ for the Sunrise Arc.

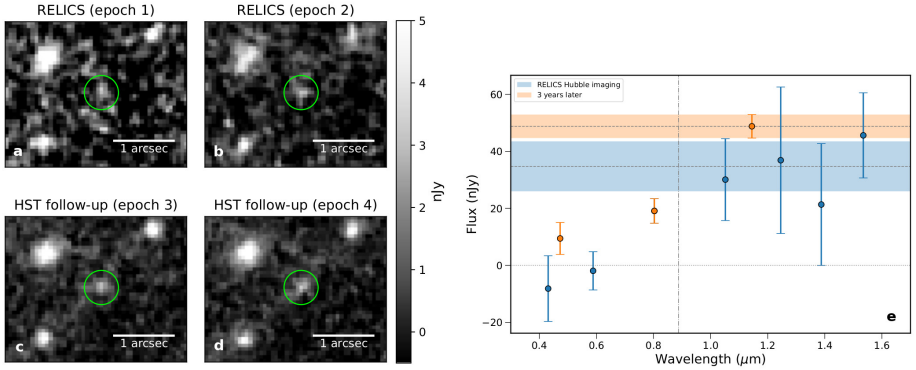

Figure 3.5: Earendel has remained consistently bright across 3.5 years of *HST* imaging. Panels **a-d** show WFC3/IR images of the lensed star (circled in green) across four epochs. Panels **a** and **b** show epochs 1 and 2 respectively, taken as part of RELICS, and are a sum of the IR imaging in 4 filters F105W+F125W+F140W+F160W from each epoch (one orbit each). Panels **c** and **d** show follow-up F110W imaging taken in epochs 3 and 4 respectively (one orbit each, in a more efficient filter). Panel **e** shows a plot of the original RELICS photometry (blue) compared to the follow-up photometry (orange), each with 1σ error bars. The blue band is the weighted average of the original RELICS IR fluxes (35 ± 9 nJy, 68% CL), while the orange band is the new F110W flux (49 ± 4 nJy, 68% CL).

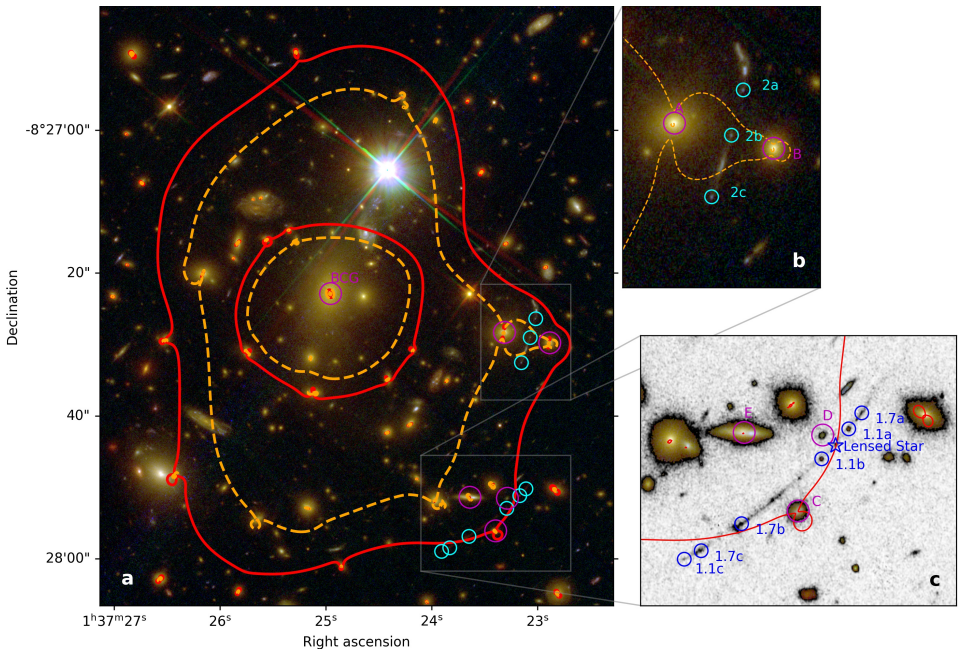

Figure 3.6: a, *HST* composite image of WHL0137−08, a massive galaxy cluster at $z = 0.566$ which lenses the Sunrise Arc. Multiple images of the two lensed galaxies used in the lens modeling are marked in cyan and labeled in zoomed outsets. Cluster member galaxies circled in magenta are those freely optimized in both the LTM and Lenstool lens models. Critical curves are shown for the best-fit LTM model. The dashed orange curve is at $z = 3.1$, the same photometric redshift as multiple image system 2 (shown in **b**), while the solid red curve is at $z = 6.2$, the photometric redshift of the Sunrise Arc (system 1, shown in **c**). The lensed star Earendel lies directly between 1.1a and 1.1b. Note that 1.1c appears fainter than its counter-images 1.1a/b due to its lower magnification and all of these images being unresolved.

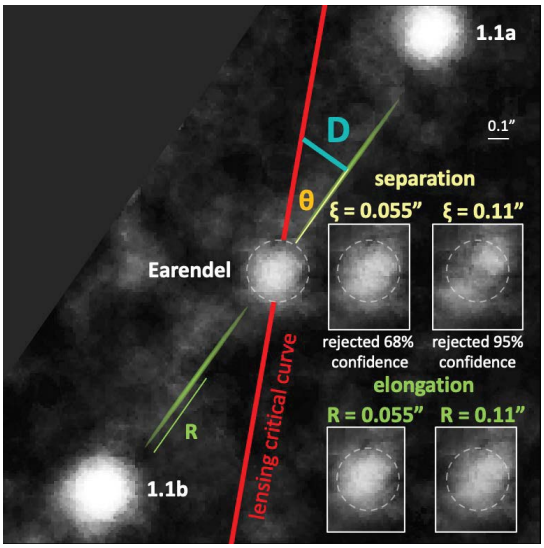

Figure 3.7: Earendel's image is spatially unresolved. We manipulate this image, separating it in two or stretching it in place to put upper limits on its magnified radius $R < 0.055''$ and distance $2\xi < 0.11''$ between two unresolved images. These constraints allow us to calculate constraints on the intrinsic radius r, distance D to the critical curve, and magnification μ for each lens model. Here we show a zoomed region of the arc around Earendel in a 10x super-sampled reconstruction of our HST WFC3/IR F110W image based on 8 drizzled exposures. The distances and radius labeled in the diagram are exaggerated for visibility.

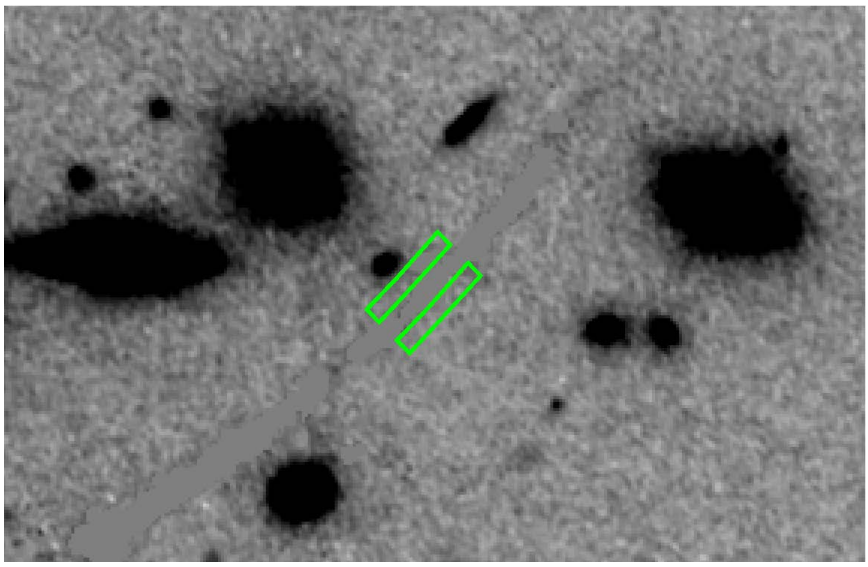

Figure 3.8: Stellar surface mass density calculations are performed in the vicinity of the lensed star, within the green boxes shown. The arc and star are masked to avoid contamination, but nearby cluster galaxies are included. This figure shows the *HST* F110W band image, which is used to define the extent of the lensed arc.

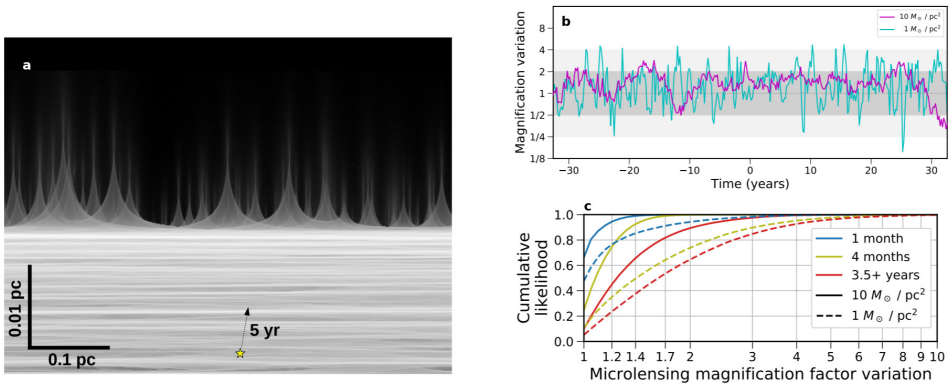

Figure 3.9: Microlensing is only expected to vary the total magnification by a factor of 2 – 3 over time, consistent with the observed steady flux over 3.5 years. Panel **a** shows the simulated microcaustic network arising from stars and stellar remnants within the lensing cluster. The cluster caustic is the extreme magnification horizontal region near the middle of the image, with individual cusps from microlenses still visible beyond the cluster caustic. We estimate Earendel will move relative to the microlens network at $\sim$ 1000 km s^{-1} in some unknown direction. Panel **b** shows predicted magnification fluctuations over time arising from this motion in the 1 $M_\odot$ pc^{-2} case (blue) and the 10 $M_\odot$ pc^{-2} case (purple), assuming that the relative motion is at an angle of 45°. Grey bands highlight a factor of 2 (dark) and a factor of 4 (light) change in magnification. Panel **c** shows the likelihood of magnification variations between two observations separated by different times, again for both the 1 and 10 $M_\odot$ pc^{-2} cases. Note the *more is less* microlensing effect that reduces variability in the observed images when the density of microlenses increases.

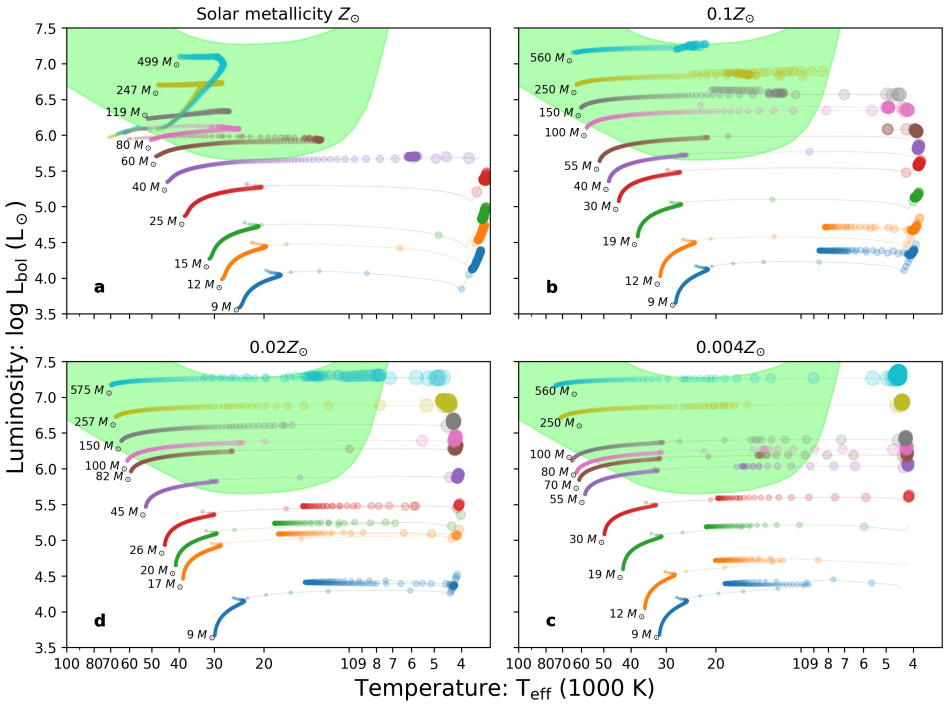

Figure 3.10: A star's metallicity will impact its evolution, so to probe this effect we show here our luminosity constraints compared to stellar tracks from BoOST at metallicities of 1, 0.1, 0.02, and $0.004Z_\odot$ (panels **a, b, c, d** respectively). The $0.1Z_\odot$ case is also shown in Figure 3.3, and these plots are similar, including the green region allowed by our analysis. While the tracks do exhibit some notable differences, the resulting mass estimates do not change significantly given the current large uncertainties.

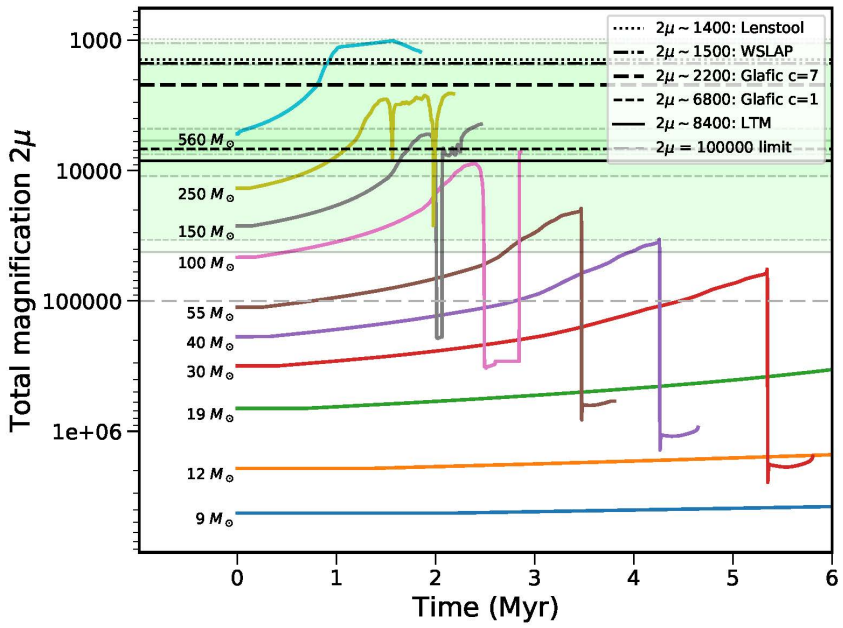

Figure 3.11: Here we show the total magnification required to lens stars to Earendel's apparent magnitude as a function of time on stellar evolution tracks (BoOST $0.1Z_{\odot}$, as plotted in the HR diagram Figure 3.3). This required magnification changes over the lifetime of each star as it varies in luminosity or temperature, changing the flux observed in the F110W filter. We find that stars at $\sim 100M_{\odot}$ and above spend the most time ($\sim$2 Myr) in the green region reproducing Earendel's observed flux, given our magnification estimates. But considering that lower mass stars are more numerous, we conclude that masses of roughly $\sim 50 - 100M_{\odot}$ are most likely if Earendel is a single star.

References

Rivera-Thorsen, T. E., H. Dahle, M. Gronke, M. Bayliss, J. R. Rigby, R. Simcoe, R. Bordoloi, M. Turner, and G. Furesz (2017). "The Sunburst Arc: Direct Lyman α escape observed in the brightest known lensed galaxy". In: *A&A* 608, L4, p. L4. DOI: 10.1051/0004-6361/201732173. arXiv: 1710.09482 [astro-ph.GA].

Johnson, Traci L., Jane R. Rigby, Keren Sharon, Michael D. Gladders, Michael Florian, Matthew B. Bayliss, Eva Wuyts, Katherine E. Whitaker, Rachael Livermore, and Katherine T. Murray (2017a). "Star Formation at z = 2.481 in the Lensed Galaxy SDSS J1110+6459: Star Formation Down to 30 pc Scales". In: *ApJL* 843.2, L21, p. L21. DOI: 10.3847/2041-8213/aa7516. arXiv: 1707.00706 [astro-ph.GA].

Kelly, Patrick L., Jose M. Diego, Steven Rodney, Nick Kaiser, Tom Broadhurst, Adi Zitrin, Tommaso Treu, Pablo G. Pérez-González, Takahiro Morishita, Mathilde Jauzac, Jonatan Selsing, Masamune Oguri, Laurent Pueyo, Timothy W. Ross, Alexei V. Filippenko, Nathan Smith, Jens Hjorth, S. Bradley Cenko, Xin Wang, D. Andrew Howell, Johan Richard, Brenda L. Frye, Saurabh W. Jha, Ryan J. Foley, Colin Norman, Marusa Bradac, Weikang Zheng, Gabriel Brammer, Alberto Molino Benito, Antonio Cava, Lise Christensen, Selma E. de Mink, Or Graur, Claudio Grillo, Ryota Kawamata, Jean-Paul Kneib, Thomas Matheson, Curtis McCully, Mario Nonino, Ismael Pérez-Fournon, Adam G. Riess, Piero Rosati, Kasper Borello Schmidt, Keren Sharon, and Benjamin J. Weiner (2018). "Extreme magnification of an individual star at redshift 1.5 by a galaxy-cluster lens". In: *Nature Astronomy* 2, pp. 334–342. DOI: 10.1038/s41550-018-0430-3. arXiv: 1706.10279 [astro-ph.GA].

Rodney, S. A., I. Balestra, M. Bradac, G. Brammer, T. Broadhurst, G. B. Caminha, G. Chirivì, J. M. Diego, A. V. Filippenko, R. J. Foley, O. Graur, C. Grillo, S. Hemmati, J. Hjorth, A. Hoag, M. Jauzac, S. W. Jha, R. Kawamata, P. L. Kelly, C. McCully, B. Mobasher, A. Molino, M. Oguri, J. Richard, A. G.

Riess, P. Rosati, K. B. Schmidt, J. Selsing, K. Sharon, L. G. Strolger, S. H. Suyu, T. Treu, B. J. Weiner, L. L. R. Williams, and A. Zitrin (2018). "Two peculiar fast transients in a strongly lensed host galaxy". In: *Nature Astronomy* 2, pp. 324–333. DOI: 10.1038/s41550-018-0405-4. arXiv: 1707.02434 [astro-ph.GA].

Chen, Wenlei, Patrick L. Kelly, Jose M. Diego, Masamune Oguri, Liliya L. R. Williams, Adi Zitrin, Tommaso L. Treu, Nathan Smith, Thomas J. Broadhurst, Nick Kaiser, Ryan J. Foley, Alexei V. Filippenko, Laura Salo, Jens Hjorth, and Jonatan Selsing (2019). "Searching for Highly Magnified Stars at Cosmological Distances: Discovery of a Redshift 0.94 Blue Supergiant in Archival Images of the Galaxy Cluster MACS J0416.1-2403". In: *ApJ* 881.1, 8, p. 8. DOI: 10.3847/1538-4357/ab297d. arXiv: 1902.05510 [astro-ph.GA].

Kaurov, Alexander A., Liang Dai, Tejaswi Venumadhav, Jordi Miralda-Escudé, and Brenda Frye (2019). "Highly Magnified Stars in Lensing Clusters: New Evidence in a Galaxy Lensed by MACS J0416.1-2403". In: *ApJ* 880.1, 58, p. 58. DOI: 10.3847/1538-4357/ab2888. arXiv: 1902.10090 [astro-ph.GA].

Coe, Dan, Brett Salmon, Maruša Bradač, Larry D. Bradley, Keren Sharon, Adi Zitrin, Ana Acebron, Catherine Cerny, Nathália Cibirka, Victoria Strait, Rachel Paterno-Mahler, Guillaume Mahler, Roberto J. Avila, Sara Ogaz, Kuang-Han Huang, Debora Pelliccia, Daniel P. Stark, Ramesh Mainali, Pascal A. Oesch, Michele Trenti, Daniela Carrasco, William A. Dawson, Steven A. Rodney, Louis-Gregory Strolger, Adam G. Riess, Christine Jones, Brenda L. Frye, Nicole G. Czakon, Keiichi Umetsu, Benedetta Vulcani, Or Graur, Saurabh W. Jha, Melissa L. Graham, Alberto Molino, Mario Nonino, Jens Hjorth, Jonatan Selsing, Lise Christensen, Shotaro Kikuchihara, Masami Ouchi, Masamune Oguri, Brian Welch, Brian C. Lemaux, Felipe Andrade-Santos, Austin T. Hoag, Traci L. Johnson, Avery Peterson, Matthew Past, Carter Fox, Irene Agulli, Rachael Livermore, Russell E. Ryan, Daniel Lam, Irene Sendra-Server, Sune Toft, Lorenzo Lovisari, and Yuanyuan Su (2019). "RELICS: Reionization Lensing Cluster Survey". In: *ApJ* 884.1, 85, p. 85. DOI: 10.3847/1538-4357/ab412b. arXiv: 1903.02002 [astro-ph.GA].

Salmon, Brett, Dan Coe, Larry Bradley, Rychard Bouwens, Marusa Bradač, Kuang-Han Huang, Pascal A. Oesch, Daniel Stark, Keren Sharon, Michele Trenti, Roberto J. Avila, Sara Ogaz, Felipe Andrade-Santos, Daniela Carrasco, Catherine Cerny, William Dawson, Brenda L. Frye, Austin Hoag, Traci Lin Johnson, Christine Jones, Daniel Lam, Lorenzo Lovisari, Ramesh Mainali, Matt Past, Rachel Paterno-Mahler, Avery Peterson, Adam G. Riess, Steven A. Rodney, Russel E. Ryan, Irene Sendra-Server, Victoria

Strait, Louis-Gregory Strolger, Keiichi Umetsu, Benedetta Vulcani, and Adi Zitrin (2020). "RELICS: The Reionization Lensing Cluster Survey and the Brightest High-z Galaxies". In: *ApJ* 889.2, 189, p. 189. DOI: 10.3847/1538-4357/ab5a8b. arXiv: 1710.08930 [astro-ph.GA].

Rivera-Thorsen, T. Emil, Håkon Dahle, John Chisholm, Michael K. Florian, Max Gronke, Jane R. Rigby, Michael D. Gladders, Guillaume Mahler, Keren Sharon, and Matthew Bayliss (2019). "Gravitational lensing reveals ionizing ultraviolet photons escaping from a distant galaxy". In: *Science* 366.6466, pp. 738–741. DOI: 10.1126/science.aaw0978. arXiv: 1904.08186 [astro-ph.GA].

Zitrin, Adi, Agnese Fabris, Julian Merten, Peter Melchior, Massimo Meneghetti, Anton Koekemoer, Dan Coe, Matteo Maturi, Matthias Bartelmann, Marc Postman, Keiichi Umetsu, Gregor Seidel, Irene Sendra, Tom Broadhurst, Italo Balestra, Andrea Biviano, Claudio Grillo, Amata Mercurio, Mario Nonino, Piero Rosati, Larry Bradley, Mauricio Carrasco, Megan Donahue, Holland Ford, Brenda L. Frye, and John Moustakas (2015). "Hubble Space Telescope Combined Strong and Weak Lensing Analysis of the CLASH Sample: Mass and Magnification Models and Systematic Uncertainties". In: *ApJ* 801.1, 44, p. 44. DOI: 10.1088/0004-637X/801/1/44. arXiv: 1411.1414 [astro-ph.CO].

Zitrin, Adi, Tom Broadhurst, Keiichi Umetsu, Dan Coe, Narciso Benítez, Begoña Ascaso, Larry Bradley, Holland Ford, James Jee, Elinor Medezinski, Yoel Rephaeli, and Wei Zheng (2009). "New multiply-lensed galaxies identified in ACS/NIC3 observations of Cl0024+1654 using an improved mass model". In: *MNRAS* 396.4, pp. 1985–2002. DOI: 10.1111/j.1365-2966.2009.14899.x. arXiv: 0902.3971 [astro-ph.CO].

Broadhurst, Tom, Narciso Benítez, Dan Coe, Keren Sharon, Kerry Zekser, Rick White, Holland Ford, Rychard Bouwens, John Blakeslee, Marc Clampin, Nick Cross, Marijn Franx, Brenda Frye, George Hartig, Garth Illingworth, Leopoldo Infante, Felipe Menanteau, Gerhardt Meurer, Marc Postman, D. R. Ardila, F. Bartko, R. A. Brown, C. J. Burrows, E. S. Cheng, P. D. Feldman, D. A. Golimowski, T. Goto, C. Gronwall, D. Herranz, B. Holden, N. Homeier, J. E. Krist, M. P. Lesser, A. R. Martel, G. K. Miley, P. Rosati, M. Sirianni, W. B. Sparks, S. Steindling, H. D. Tran, Z. I. Tsvetanov, and W. Zheng (2005). "Strong-Lensing Analysis of A1689 from Deep Advanced Camera Images". In: *ApJ* 621.1, pp. 53–88. DOI: 10.1086/426494. arXiv: astro-ph/0409132 [astro-ph].

Jullo, E. and J. P. Kneib (2009). "Multiscale cluster lens mass mapping - I. Strong lensing modelling". In: *MNRAS* 395.3, pp. 1319–1332. DOI: 10.1111/j.1365-2966.2009.14654.x. arXiv: 0901.3792 [astro-ph.CO].

Jullo, E., J. P. Kneib, M. Limousin, Á. Elíasdóttir, P. J. Marshall, and T. Verdugo (2007). "A Bayesian approach to strong lensing modelling of galaxy clusters". In: *New Journal of Physics* 9.12, p. 447. DOI: 10.1088/1367-2630/9/12/447. arXiv: 0706.0048 [astro-ph].

Oguri, Masamune (2010). "The Mass Distribution of SDSS J1004+4112 Revisited". In: *PASJ* 62, p. 1017. DOI: 10.1093/pasj/62.4.1017. arXiv: 1005.3103 [astro-ph.CO].

Diego, J. M., M. Tegmark, P. Protopapas, and H. B. Sandvik (2007). "Combined reconstruction of weak and strong lensing data with WSLAP". In: *MNRAS* 375.3, pp. 958–970. DOI: 10.1111/j.1365-2966.2007.11380.x. arXiv: astro-ph/0509103 [astro-ph].

Diego, J. M., P. Protopapas, H. B. Sandvik, and M. Tegmark (2005). "Non-parametric inversion of strong lensing systems". In: *MNRAS* 360.2, pp. 477–491. DOI: 10.1111/j.1365-2966.2005.09021.x. arXiv: astro-ph/0408418 [astro-ph].

Diego, J. M. (2019). "The Universe at extreme magnification". In: *A&A* 625, A84, A84. DOI: 10.1051/0004-6361/201833670. arXiv: 1806.04668 [astro-ph.GA].

Meneghetti, M., P. Natarajan, D. Coe, E. Contini, G. De Lucia, C. Giocoli, A. Acebron, S. Borgani, M. Bradac, J. M. Diego, A. Hoag, M. Ishigaki, T. L. Johnson, E. Jullo, R. Kawamata, D. Lam, M. Limousin, J. Liesenborgs, M. Oguri, K. Sebesta, K. Sharon, L. L. R. Williams, and A. Zitrin (2017). "The Frontier Fields lens modelling comparison project". In: *MNRAS* 472.3, pp. 3177–3216. DOI: 10.1093/mnras/stx2064. arXiv: 1606.04548 [astro-ph.CO].

Venumadhav, Tejaswi, Liang Dai, and Jordi Miralda-Escudé (2017). "Microlensing of Extremely Magnified Stars near Caustics of Galaxy Clusters". In: *ApJ* 850.1, 49, p. 49. DOI: 10.3847/1538-4357/aa9575. arXiv: 1707.00003 [astro-ph.CO].

Diego, Jose M., Nick Kaiser, Tom Broadhurst, Patrick L. Kelly, Steve Rodney, Takahiro Morishita, Masamune Oguri, Timothy W. Ross, Adi Zitrin, Mathilde Jauzac, Johan Richard, Liliya Williams, Jesus Vega-Ferrero, Brenda Frye, and Alexei V. Filippenko (2018). "Dark Matter under the Microscope: Constraining Compact Dark Matter with Caustic Crossing Events". In: *ApJ* 857.1, 25, p. 25. DOI: 10.3847/1538-4357/aab617. arXiv: 1706.10281 [astro-ph.CO].

Dai, Liang (2021). "Statistical microlensing towards magnified high-redshift star clusters". In: *MNRAS* 501.4, pp. 5538–5553. DOI: 10.1093/mnras/stab017. arXiv: 2007.01301 [astro-ph.GA].

Portegies Zwart, Simon F., Stephen L. W. McMillan, and Mark Gieles (2010). "Young Massive Star Clusters". In: *ARA&A* 48, pp. 431–493. DOI: 10.1146/annurev-astro-081309-130834. arXiv: 1002.1961 [astro-ph.GA].

Figer, Donald F., Ian S. McLean, and Mark Morris (1999). "Massive Stars in the Quintuplet Cluster". In: *ApJ* 514.1, pp. 202–220. DOI: 10.1086/306931. arXiv: astro-ph/9903281 [astro-ph].

Bouwens, R. J., G. D. Illingworth, P. A. Oesch, M. Maseda, B. Ribeiro, M. Stefanon, and D. Lam (2017). "Very low-luminosity galaxies in the early universe have observed sizes similar to single star cluster complexes". In: *arXiv e-prints*, arXiv:1711.02090, arXiv:1711.02090. arXiv: 1711.02090 [astro-ph.GA].

Vanzella, E., F. Calura, M. Meneghetti, M. Castellano, G. B. Caminha, A. Mercurio, G. Cupani, P. Rosati, C. Grillo, R. Gilli, M. Mignoli, G. Fiorentino, C. Arcidiacono, M. Lombini, and F. Cortecchia (2019). "Massive star cluster formation under the microscope at z = 6". In: *MNRAS* 483.3, pp. 3618–3635. DOI: 10.1093/mnras/sty3311. arXiv: 1809.02617 [astro-ph.GA].

Behrendt, M., M. Schartmann, and A. Burkert (2019). "The possible hierarchical scales of observed clumps in high-redshift disc galaxies". In: *MNRAS* 488.1, pp. 306–323. DOI: 10.1093/mnras/stz1717. arXiv: 1906.04182 [astro-ph.GA].

Sana, H., S. E. de Mink, A. de Koter, N. Langer, C. J. Evans, M. Gieles, E. Gosset, R. G. Izzard, J. B. Le Bouquin, and F. R. N. Schneider (2012). "Binary Interaction Dominates the Evolution of Massive Stars". In: *Science* 337.6093, p. 444. DOI: 10.1126/science.1223344. arXiv: 1207.6397 [astro-ph.SR].

Sana, H., J. B. Le Bouquin, S. Lacour, J. P. Berger, G. Duvert, L. Gauchet, B. Norris, J. Olofsson, D. Pickel, G. Zins, O. Absil, A. de Koter, K. Kratter, O. Schnurr, and H. Zinnecker (2014). "Southern Massive Stars at High Angular Resolution: Observational Campaign and Companion Detection". In: *ApJS* 215.1, 15, p. 15. DOI: 10.1088/0067-0049/215/1/15. arXiv: 1409.6304 [astro-ph.SR].

Moe, Maxwell and Rosanne Di Stefano (2017). "Mind Your Ps and Qs: The Interrelation between Period (P) and Mass-ratio (Q) Distributions of Binary Stars". In: *ApJS* 230.2, 15, p. 15. DOI: 10.3847/1538-4365/aa6fb6. arXiv: 1606.05347 [astro-ph.SR].

Szécsi, Dorottya, Richard Wünsch, Poojan Agrawal, and Norbert Langer (2020). "'Bonn' Optimized Stellar Tracks (BoOST). Simulated Populations of Massive and Very Massive Stars for Astrophysical Applications". In: *arXiv e-prints*, arXiv:2004.08203, arXiv:2004.08203. arXiv: 2004.08203 [astro-ph.SR].

Shimizu, Ikkoh, Akio K. Inoue, Takashi Okamoto, and Naoki Yoshida (2016). "Nebular line emission from z $>$ 7 galaxies in a cosmological simulation: rest-frame UV to optical lines". In: *MNRAS* 461.4, pp. 3563–3575. DOI: 10.1093/mnras/stw1423. arXiv: 1509.00800 [astro-ph.GA].

Wen, Z. L., J. L. Han, and F. S. Liu (2012). "A Catalog of 132,684 Clusters of Galaxies Identified from Sloan Digital Sky Survey III". In: *ApJS* 199.2, 34, p. 34. DOI: 10.1088/0067-0049/199/2/34. arXiv: 1202.6424 [astro-ph.CO].

Wen, Z. L. and J. L. Han (2015). "Calibration of the Optical Mass Proxy for Clusters of Galaxies and an Update of the WHL12 Cluster Catalog". In: *ApJ* 807.2, 178, p. 178. DOI: 10.1088/0004-637X/807/2/178. arXiv: 1506.04503 [astro-ph.GA].

Alam, Shadab et al. (2015). "The Eleventh and Twelfth Data Releases of the Sloan Digital Sky Survey: Final Data from SDSS-III". In: *ApJS* 219.1, 12, p. 12. DOI: 10.1088/0067-0049/219/1/12. arXiv: 1501.00963 [astro-ph.IM].

Planck Collaboration et al. (2016). "Planck 2015 results. XXVII. The second Planck catalogue of Sunyaev-Zeldovich sources". In: *A&A* 594, A27, A27. DOI: 10.1051/0004-6361/201525823. arXiv: 1502.01598 [astro-ph.CO].

Sunyaev, R. A. and Ya. B. Zeldovich (1970). "Small-Scale Fluctuations of Relic Radiation". In: *Ap&SS* 7.1, pp. 3–19. DOI: 10.1007/BF00653471.

Strait, Victoria, Maruša Bradač, Dan Coe, Brian C. Lemaux, Adam C. Carnall, Larry Bradley, Debora Pelliccia, Keren Sharon, Adi Zitrin, Ana Acebron, Chloe Neufeld, Felipe Andrade-Santos, Roberto J. Avila, Brenda L. Frye, Guillaume Mahler, Mario Nonino, Sara Ogaz, Masamune Oguri, Masami Ouchi, Rachel Paterno-Mahler, Daniel P. Stark, Ramesh Mainali, Pascal A. Oesch, Michele Trenti, Daniela Carrasco, William A. Dawson, Christine Jones, Keiichi Umetsu, and Benedetta Vulcani (2021). "RELICS: Properties of z $\geq$ 5.5 Galaxies Inferred from Spitzer and Hubble Imaging, Including A Candidate z $\sim$ 6.8 Strong [O III] emitter". In: *ApJ* 910.2, 135, p. 135. DOI: 10.3847/1538-4357/abe533. arXiv: 2009.00020 [astro-ph.GA].

Bertin, E. and S. Arnouts (1996). "SExtractor: Software for source extraction." In: *A&AS* 117, pp. 393–404. DOI: 10.1051/aas:1996164.

Benítez, Narciso (2000). "Bayesian Photometric Redshift Estimation". In: *ApJ* 536.2, pp. 571–583. DOI: 10.1086/308947. arXiv: astro-ph/9811189 [astro-ph].

Coe, Dan, Narciso Benítez, Sebastián F. Sánchez, Myungkook Jee, Rychard Bouwens, and Holland Ford (2006). "Galaxies in the Hubble Ultra Deep Field. I. Detection, Multiband Photometry, Photometric Redshifts, and Morphology". In: *AJ* 132.2, pp. 926–959. DOI: 10.1086/505530. arXiv: astro-ph/0605262 [astro-ph].

Carnall, A. C., R. J. McLure, J. S. Dunlop, and R. Davé (2018). "Inferring the star formation histories of massive quiescent galaxies with BAGPIPES: evidence for multiple quenching mechanisms". In: *MNRAS* 480.4, pp. 4379–4401. DOI: 10.1093/mnras/sty2169. arXiv: 1712.04452 [astro-ph.GA].

Eldridge, J. J., E. R. Stanway, L. Xiao, L. A. S. McClelland, G. Taylor, M. Ng, S. M. L. Greis, and J. C. Bray (2017). "Binary Population and Spectral Synthesis Version 2.1: Construction, Observational Verification, and New Results". In: *PASA* 34, e058, e058. DOI: 10.1017/pasa.2017.51. arXiv: 1710.02154 [astro-ph.SR].

Ferland, G. J., M. Chatzikos, F. Guzmán, M. L. Lykins, P. A. M. van Hoof, R. J. R. Williams, N. P. Abel, N. R. Badnell, F. P. Keenan, R. L. Porter, and P. C. Stancil (2017). "The 2017 Release Cloudy". In: *RMxAA* 53, pp. 385–438. arXiv: 1705.10877 [astro-ph.GA].

Salpeter, Edwin E. (1955). "The Luminosity Function and Stellar Evolution." In: *ApJ* 121, p. 161. DOI: 10.1086/145971.

Calzetti, Daniela, Lee Armus, Ralph C. Bohlin, Anne L. Kinney, Jan Koornneef, and Thaisa Storchi-Bergmann (2000). "The Dust Content and Opacity of Actively Star-forming Galaxies". In: *ApJ* 533.2, pp. 682–695. DOI: 10.1086/308692. arXiv: astro-ph/9911459 [astro-ph].

Ellis, Richard S., Ian Smail, Alan Dressler, Warrick J. Couch, Jr. Oemler Augustus, Harvey Butcher, and Ray M. Sharples (1997). "The Homogeneity of Spheroidal Populations in Distant Clusters". In: *ApJ* 483.2, pp. 582–596. DOI: 10.1086/304261. arXiv: astro-ph/9607154 [astro-ph].

Stanford, S. A., Peter R. Eisenhardt, and Mark Dickinson (1998). "The Evolution of Early-Type Galaxies in Distant Clusters". In: *ApJ* 492.2, pp. 461–479. DOI: 10.1086/305050. arXiv: astro-ph/9708037 [astro-ph].

Hastings, W. K. (1970). "Monte Carlo sampling methods using Markov chains and their applications". In: *Biometrika* 57.1, pp. 97–109. ISSN: 0006-3444. DOI: 10.1093/biomet/57.1.97. eprint: https://academic.oup.com/biomet/article-pdf/57/1/97/23940249/57-1-97.pdf. URL: https://doi.org/10.1093/biomet/57.1.97.

Limousin, Marceau, Jean-Paul Kneib, and Priyamvada Natarajan (2005). "Constraining the mass distribution of galaxies using galaxy-galaxy lensing in

clusters and in the field". In: *MNRAS* 356.1, pp. 309–322. DOI: 10.1111/j.1365-2966.2004.08449.x. arXiv: astro-ph/0405607 [astro-ph].

Elíasdóttir, Árdís, Marceau Limousin, Johan Richard, Jens Hjorth, Jean-Paul Kneib, Priya Natarajan, Kristian Pedersen, Eric Jullo, and Danuta Paraficz (2007). "Where is the matter in the Merging Cluster Abell 2218?" In: *arXiv e-prints*, arXiv:0710.5636, arXiv:0710.5636. arXiv: 0710.5636 [astro-ph].

Navarro, Julio F., Carlos S. Frenk, and Simon D. M. White (1996). "The Structure of Cold Dark Matter Halos". In: *ApJ* 462, p. 563. DOI: 10.1086/177173. arXiv: astro-ph/9508025 [astro-ph].

Johnson, Traci L., Keren Sharon, Michael D. Gladders, Jane R. Rigby, Matthew B. Bayliss, Eva Wuyts, Katherine E. Whitaker, Michael Florian, and Katherine T. Murray (2017b). "Star Formation at z = 2.481 in the Lensed Galaxy SDSS J1110 = 6459. I. Lens Modeling and Source Reconstruction". In: *ApJ* 843.2, 78, p. 78. DOI: 10.3847/1538-4357/aa7756. arXiv: 1707.00707 [astro-ph.GA].

Dai, Liang and Massimo Pascale (2021). "New Approximation of Magnification Statistics for Random Microlensing of Magnified Sources". In: *arXiv e-prints*, arXiv:2104.12009, arXiv:2104.12009. arXiv: 2104.12009 [astro-ph.GA].

Jiménez-Teja, Yolanda, Jose M. Vílchez, Renato A. Dupke, Paulo A. A. Lopes, Nícolas O. L. de Oliveira, and Dan Coe (2021). "RELICS: ICL Analysis of the $z = 0.566$ merging cluster WHL J013719.8-08284". In: *arXiv e-prints*, arXiv:2109.04485, arXiv:2109.04485. arXiv: 2109.04485 [astro-ph.GA].

Kriek, Mariska, Pieter G. van Dokkum, Ivo Labbé, Marijn Franx, Garth D. Illingworth, Danilo Marchesini, and Ryan F. Quadri (2009). "An Ultra-Deep Near-Infrared Spectrum of a Compact Quiescent Galaxy at z = 2.2". In: *ApJ* 700.1, pp. 221–231. DOI: 10.1088/0004-637X/700/1/221. arXiv: 0905.1692 [astro-ph.CO].

Bruzual, G. and S. Charlot (2003). "Stellar population synthesis at the resolution of 2003". In: *MNRAS* 344.4, pp. 1000–1028. DOI: 10.1046/j.1365-8711.2003.06897.x. arXiv: astro-ph/0309134 [astro-ph].

Chabrier, Gilles (2003). "Galactic Stellar and Substellar Initial Mass Function". In: *PASP* 115.809, pp. 763–795. DOI: 10.1086/376392. arXiv: astro-ph/0304382 [astro-ph].

Spera, Mario, Michela Mapelli, and Alessandro Bressan (2015). "The mass spectrum of compact remnants from the PARSEC stellar evolution tracks". In: *MNRAS* 451.4, pp. 4086–4103. DOI: 10.1093/mnras/stv1161. arXiv: 1505.05201 [astro-ph.SR].

Oguri, Masamune, Jose M. Diego, Nick Kaiser, Patrick L. Kelly, and Tom Broadhurst (2018). "Understanding caustic crossings in giant arcs: Characteristic scales, event rates, and constraints on compact dark matter". In: *PhRvD* 97.2, 023518, p. 023518. DOI: 10.1103/PhysRevD.97.023518. arXiv: 1710.00148 [astro-ph.CO].

Windhorst, Rogier A., F. X. Timmes, J. Stuart B. Wyithe, Mehmet Alpaslan, Stephen K. Andrews, Daniel Coe, Jose M. Diego, Mark Dijkstra, Simon P. Driver, Patrick L. Kelly, and Duho Kim (2018). "On the Observability of Individual Population III Stars and Their Stellar-mass Black Hole Accretion Disks through Cluster Caustic Transits". In: *ApJS* 234.2, 41, p. 41. DOI: 10.3847/1538-4365/aaa760. arXiv: 1801.03584 [astro-ph.GA].

Lejeune, Th., F. Cuisinier, and R. Buser (1997). "Standard stellar library for evolutionary synthesis. I. Calibration of theoretical spectra". In: *A&AS* 125, pp. 229–246. DOI: 10.1051/aas:1997373. arXiv: astro-ph/9701019 [astro-ph].

Calzetti, D., K. E. Johnson, A. Adamo, III Gallagher J. S., J. E. Andrews, L. J. Smith, G. C. Clayton, J. C. Lee, E. Sabbi, L. Ubeda, H. Kim, J. E. Ryon, D. Thilker, S. N. Bright, E. Zackrisson, R. C. Kennicutt, S. E. de Mink, B. C. Whitmore, A. Aloisi, R. Chandar, M. Cignoni, D. Cook, D. A. Dale, B. G. Elmegreen, D. M. Elmegreen, A. S. Evans, M. Fumagalli, D. A. Gouliermis, K. Grasha, E. K. Grebel, M. R. Krumholz, R. Walterbos, A. Wofford, T. M. Brown, C. Christian, C. Dobbs, A. Herrero, L. Kahre, M. Messa, P. Nair, A. Nota, G. Östlin, A. Pellerin, E. Sacchi, D. Schaerer, and M. Tosi (2015). "The Brightest Young Star Clusters in NGC 5253." In: *ApJ* 811.2, 75, p. 75. DOI: 10.1088/0004-637X/811/2/75. arXiv: 1508.04476 [astro-ph.GA].

Sanyal, D., L. Grassitelli, N. Langer, and J. M. Bestenlehner (2015). "Massive main-sequence stars evolving at the Eddington limit". In: *A&A* 580, A20, A20. DOI: 10.1051/0004-6361/201525945. arXiv: 1506.02997 [astro-ph.SR].

El-Badry, Kareem, Hans-Walter Rix, Haijun Tian, Gaspard Duchêne, and Maxwell Moe (2019). "Discovery of an equal-mass 'twin' binary population reaching 1000 + au separations". In: *MNRAS* 489.4, pp. 5822–5857. DOI: 10.1093/mnras/stz2480. arXiv: 1906.10128 [astro-ph.SR].

Leitherer, Claus, Daniel Schaerer, Jeffrey D. Goldader, Rosa M. González Delgado, Carmelle Robert, Denis Foo Kune, Duília F. de Mello, Daniel Devost, and Timothy M. Heckman (1999). "Starburst99: Synthesis Models for Galaxies with Active Star Formation". In: *ApJS* 123.1, pp. 3–40. DOI: 10.1086/313233. arXiv: astro-ph/9902334 [astro-ph].

Kroupa, Pavel (2001). "On the variation of the initial mass function". In: *MNRAS* 322.2, pp. 231–246. DOI: 10.1046/j.1365-8711.2001.04022.x. arXiv: astro-ph/0009005 [astro-ph].

da Silva, Robert L., Michele Fumagalli, and Mark Krumholz (2012). "SLUG—Stochastically Lighting Up Galaxies. I. Methods and Validating Tests". In: *ApJ* 745.2, 145, p. 145. DOI: 10.1088/0004-637X/745/2/145. arXiv: 1106.3072 [astro-ph.IM].

Krumholz, Mark R., Michele Fumagalli, Robert L. da Silva, Theodore Rendahl, and Jonathan Parra (2015). "SLUG - stochastically lighting up galaxies - III. A suite of tools for simulated photometry, spectroscopy, and Bayesian inference with stochastic stellar populations". In: *MNRAS* 452.2, pp. 1447–1467. DOI: 10.1093/mnras/stv1374. arXiv: 1502.05408 [astro-ph.GA].

Madau, Piero and Mark Dickinson (2014). "Cosmic Star-Formation History". In: *ARA&A* 52, pp. 415–486. DOI: 10.1146/annurev-astro-081811-125615. arXiv: 1403.0007 [astro-ph.CO].

Kehrig, C., J. M. Vílchez, M. A. Guerrero, J. Iglesias-Páramo, L. K. Hunt, S. Duarte-Puertas, and G. Ramos-Larios (2018). "The extended He II λ4686 emission in the extremely metal-poor galaxy SBS 0335 - 052E seen with MUSE". In: *MNRAS* 480.1, pp. 1081–1095. DOI: 10.1093/mnras/sty1920. arXiv: 1807.09307 [astro-ph.GA].

Sarmento, Richard, Evan Scannapieco, and Seth Cohen (2018). "Following the Cosmic Evolution of Pristine Gas. II. The Search for Pop III-bright Galaxies". In: *ApJ* 854.1, 75, p. 75. DOI: 10.3847/1538-4357/aa989a. arXiv: 1710.09878 [astro-ph.GA].

Sarmento, Richard, Evan Scannapieco, and Benoit Côté (2019). "Following the Cosmic Evolution of Pristine Gas. III. The Observational Consequences of the Unknown Properties of Population III Stars". In: *ApJ* 871.2, 206, p. 206. DOI: 10.3847/1538-4357/aafa1a. arXiv: 1901.03727 [astro-ph.GA].

Trenti, Michele, Massimo Stiavelli, and J. Michael Shull (2009). "Metal-free Gas Supply at the Edge of Reionization: Late-epoch Population III Star Formation". In: *ApJ* 700.2, pp. 1672–1679. DOI: 10.1088/0004-637X/700/2/1672. arXiv: 0905.4504 [astro-ph.CO].

Vanzella, E., M. Meneghetti, G. B. Caminha, M. Castellano, F. Calura, P. Rosati, C. Grillo, M. Dijkstra, M. Gronke, E. Sani, A. Mercurio, P. Tozzi, M. Nonino, S. Cristiani, M. Mignoli, L. Pentericci, R. Gilli, T. Treu, K. Caputi, G. Cupani, A. Fontana, A. Grazian, and I. Balestra (2020). "Candidate Population III stellar complex at z = 6.629 in the MUSE Deep Lensed Field". In: *MNRAS*

494.1, pp. L81–L85. DOI: 10.1093/mnrasl/slaa041. arXiv: 2001.03619 [astro-ph.GA].

Abbott, R. et al. (2020). "GW190521: A Binary Black Hole Merger with a Total Mass of 150 $M_\odot$". In: *Phys. Rev. Lett.* 125 (10), p. 101102. DOI: 10.1103/PhysRevLett.125.101102. URL: https://link.aps.org/doi/10.1103/PhysRevLett.125.101102.

Farrell, Eoin, Jose H Groh, Raphael Hirschi, Laura Murphy, Etienne Kaiser, Sylvia Ekström, Cyril Georgy, and Georges Meynet (2020). "Is GW190521 the merger of black holes from the first stellar generations?" In: *Monthly Notices of the Royal Astronomical Society: Letters* 502.1, pp. L40–L44. ISSN: 1745-3925. DOI: 10.1093/mnrasl/slaa196. eprint: https://academic.oup.com/mnrasl/article-pdf/502/1/L40/35930611/slaa196.pdf. URL: https://doi.org/10.1093/mnrasl/slaa196.

Kinugawa, Tomoya, Takashi Nakamura, and Hiroyuki Nakano (2020). "Formation of binary black holes similar to GW190521 with a total mass of 150 M from Population III binary star evolution". In: *Monthly Notices of the Royal Astronomical Society: Letters* 501.1, pp. L49–L53. ISSN: 1745-3925. DOI: 10.1093/mnrasl/slaa191. eprint: https://academic.oup.com/mnrasl/article-pdf/501/1/L49/35065121/slaa191.pdf. URL: https://doi.org/10.1093/mnrasl/slaa191.

Zdziarski, Andrzej A. and Marek Gierliński (2004). "Radiative Processes, Spectral States and Variability of Black-Hole Binaries". In: *Progress of Theoretical Physics Supplement* 155, pp. 99–119. ISSN: 0375-9687. DOI: 10.1143/PTPS.155.99. eprint: https://academic.oup.com/ptps/article-pdf/doi/10.1143/PTPS.155.99/5353498/155-99.pdf. URL: https://doi.org/10.1143/PTPS.155.99.

Holwerda, B. W., M. Trenti, W. Clarkson, K. Sahu, L. Bradley, M. Stiavelli, N. Pirzkal, G. De Marchi, M. Andersen, R. Bouwens, and R. Ryan (2014). "Milky Way Red Dwarfs in the BoRG Survey; Galactic Scale-height and the Distribution of Dwarf Stars in WFC3 Imaging". In: *ApJ* 788.1, 77, p. 77. DOI: 10.1088/0004-637X/788/1/77. arXiv: 1402.4117 [astro-ph.GA].

Burgasser, A. J. and Splat Development Team (2017). "The SpeX Prism Library Analysis Toolkit (SPLAT): A Data Curation Model". In: *Astronomical Society of India Conference Series*. Vol. 14. Astronomical Society of India Conference Series, pp. 7–12. arXiv: 1707.00062 [astro-ph.SR].

Hainline, Kevin N., Alice E. Shapley, Jenny E. Greene, and Charles C. Steidel (2011). "The Rest-frame Ultraviolet Spectra of UV-selected Active Galactic

Nuclei at z ∼2-3". In: *ApJ* 733.1, 31, p. 31. DOI: 10.1088/0004-637X/733/1/31. arXiv: 1012.0075 [astro-ph.CO].

Chapter 4

RELICS: Small-scale Star Formation in Lensed Galaxies at Redshift 6 – 10

4.1 Introduction

Deep field observations with the Hubble Space Telescope (HST) have revealed that galaxies at high redshift tend to be smaller (Shibuya, Ouchi, and Harikane, 2015; Shibuya et al., 2019; Mowla et al., 2019; Neufeld et al., 2021) exhibit clumpier structures (Shibuya et al., 2016) than local galaxies. In field galaxies, these clump structures were found to have typical radii of $\sim$ 1 kpc (e.g., Elmegreen and Elmegreen, 2005; Elmegreen et al., 2007; Elmegreen et al., 2009; Guo et al., 2011; Genzel et al., 2011; Förster Schreiber et al., 2011; Guo et al., 2015; Guo et al., 2018). These observations were largely limited by the resolution of HST, which can not observe smaller scales at high redshift without assistance. The magnifying effect of gravitational lensing has opened a new window into small scale star formation in distant galaxies. Using HST and strong lensing, many studies have been able to push to scales of $\sim$ 100 pc across a broad range of redshifts (e.g., Jones et al., 2010; Livermore et al., 2012;

Wuyts et al., 2014; Livermore et al., 2015). In certain cases, smaller structures can be observed when galaxies reach particularly high magnifications, leading to detections of clumps measuring tens of pc in radius (Vanzella et al., 2017a; Vanzella et al., 2017b; Johnson et al., 2017a; Zick et al., 2020).

These observations of smaller structures has put pressure on the dominant explanation of clump formation in the high-redshift universe. Recent studies have found evidence of bias towards larger clump radii and masses at low spatial resolution (Dessauges-Zavadsky et al., 2017; Cava et al., 2018). Furthermore, while lower-resolution simulations tended to favor larger, more massive ($\sim 10^9 M_\odot$) clumps (Mandelker et al., 2014), more recent higher-resolution simulations have found broader mass ranges, and tend to favor smaller ($\sim 10^7 M_\odot$) clumps (Tamburello et al., 2015; Mandelker et al., 2017; Oklopčić et al., 2017). Thus continued study of strongly magnified galaxies at high redshifts are critical to our understanding of early galaxy structures.

Recently, the study of highly magnified clumps has been pushed to even higher redshift, with Vanzella et al., 2019 reporting a clump measuring 13 pc at $z \sim 6$. These highly magnified clumps allow exploration of spatial scales otherwise unreachable with current telescopes. In particular, they enable studies of clumps on the same scale as local young massive star clusters (YMCs, Portegies Zwart, McMillan, and Gieles, 2010). Recent studies of YMCs in local galaxies have found peaks in the distribution of radii around 2-3 pc, with some examples reaching 10 pc in radius (Bastian et al., 2012; Ryon et al., 2017). Local observations of globular clusters have found similar distributions of radii (Puzia et al., 2014). Thus YMCs have been proposed as candidate

proto-globular clusters, although this remains uncertain (e.g., Bastian and Lardo, 2018; Kim et al., 2018; Terlevich et al., 2018). Highly magnified objects in the distant universe present an opportunity to directly study these possible globular cluster progenitors.

In this paper, we present HST observations of three highly magnified lensed galaxies at $6 < z \lesssim 10$. These galaxies all exhibit clumpy morphologies, and the high magnifications allow us to study them in detail.

In Section 4.2 we present the HST data used in this study. Section 4.3 presents the lens models used, while Section 4.4 discusses our measurements of clump radii. SED fitting is presented in Section 4.5. We present our results in Section 4.6, and we contextualize these results in the subsequent Section 4.7. Finally, we summarize our conclusions in Section 4.8. We assume a flat cosmology with $\Omega_m = 0.3$, $\Omega_\Lambda = 0.7$, and $H_0 = 70$ km s^{-1} Mpc^{-1} throughout.

4.2 Data

The high-redshift galaxies considered here were discovered in the Reionization Lensing Cluster Survey (RELICS; Coe et al. 2019). RELICS observed a total of 41 galaxy clusters with HST, obtaining single-orbit depth in each of the ACS F435W, F606W, and F814W bands along with a total of two orbits split between the WFC3/IR filters F105W, F125W, F140W, and F160W. The RELICS clusters were also observed with the Spitzer Space Telescope through the Spitzer-RELICS program (S-RELICS, PI Bradač).

Salmon et al., 2018 discovered a $\sim 2.5''$ lensed arc of a galaxy with a photometric redshift of $z_{phot} = 9.9^{+0.8}_{-0.6}$ magnified by the galaxy cluster SPT-CL

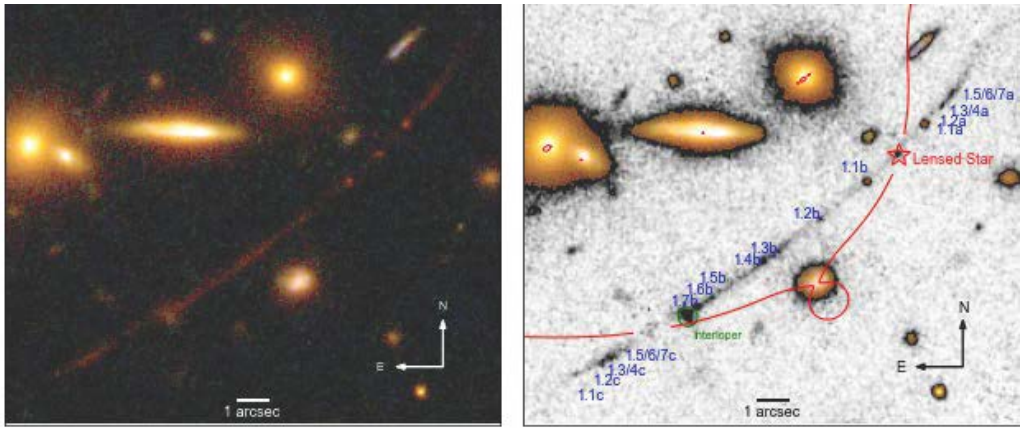

Figure 4.1: The 15″ long Sunrise Arc at $z_{phot} = 6.2 \pm 0.1$ is the longest lensed arc at $z > 6$. The left panel shows a color composite of the arc, with the HST F435W band represented in the blue channel, a combination of F606W and F814W in the green channel, and the full WFC3/IR stack (F105W + F110W + F125W + F140W + F160W) shown in the red channel. The right panel shows a hybrid F110W/color image, with the F110W image shown in pixels with flux below 0.05 e^- sec^{-1} $\sim$ 3.4 nJy, while pixels above that threshold show the same color image as in the left panel. The arc contains seven total clump features labeled in blue in the right panel, with multiple images identified by the letters a/b/c. The lensing critical curve is shown in red, broken where it crosses the arc for clarity. One lower-redshift interloper appears along the arc, and is circled in green. This arc also contains an extremely magnified star, highlighted with a red star, which is discussed in detail in Welch er al. 2022. Each of the seven lensed clumps have measured radii less than 10 parsecs, providing a detailed look into the substructure of this galaxy.

J0615–5746 (hearafter SPT0615–57). The lensed arc is dubbed SPT0615-JD1, and it consists of a total of 5 clumps labeled in Figure 4.3. The cluster was discovered independently by the South Pole Telescope survey (SPT; Williamson et al. 2011) and the Planck Collaboration et al., 2011, and it was determined to have a high mass ($M_{500} = 7 \times 10^{14} M_{\odot}$) and high redshift ($z = 0.972$). SPT0615–57 was followed up with additional HST imaging (GO 15920, P.I. Salmon), which obtained an additional one orbit each in F105W and F125W, and two orbits each in F140W and F160W. Because of the promising $z \sim 10$ arc in this field, this cluster received additional Spitzer observations, for a total of 30 hours of exposure time in each of the IRAC bands ($3.6\mu m$ and $4.5\mu m$).

The galaxy cluster MACS J0308+2645 (henceforth MACS0308) was presented as part of the Massive Cluster Survey (MACS; Ebeling, Edge, and Henry 2001). It is at redshift $z = 0.356$ and has an SZ mass of $M_{500} = 10.8 \times 10^{14} M_{\odot}$, making it the 12th most massive cluster in the Planck PSZ2 cluster catalog (Planck Collaboration et al., 2016). This cluster lenses an exceptionally bright galaxy dubbed MACS0308-904, which is the brightest lensed arc in the RELICS sample with an AB magnitude of 23.4 in the F160W filter (Salmon et al., 2020). This arc is shown in Figure 4.2, which identifies the brightest clump (1.1) as well as an additional faint clump further along the arc (1.2). The cluster MACS0308 was observed for a total of 5 hours in each Spitzer IRAC band.

WHL0137–08 was discovered in SDSS imaging as an overdensity of red galaxies by Wen, Han, and Liu, 2012, and its redshift was subsequently confirmed at $z = 0.566$ by Wen and Han, 2015. This cluster was ranked as the 31st most massive cluster in the Planck PSZ2 catalog with a mass

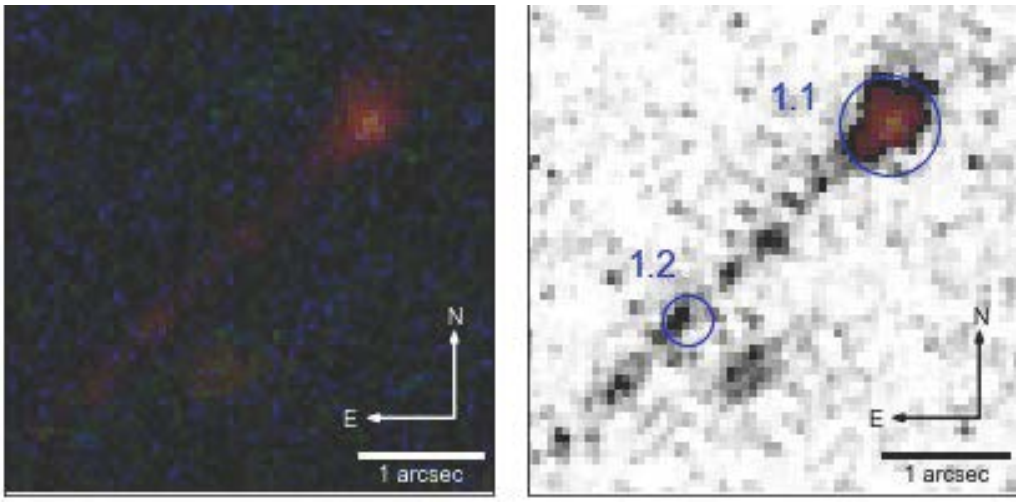

Figure 4.2: The lensed arc MACS0308-zD1 at $z_{phot} = 6.3 \pm 0.1$ is the brightest known lensed galaxy at $z > 6$. As in Figure 4.1, the left panel shows an HST color composite, where the blue channel shows F435W, green is F606W + F814W, and red is the WFC3/IR stack of F105W + F125W + F140W + F160W. The right panel shows the hybrid F105W/color image, with a transition threshold of 0.05 e^{-} sec^{-1} $\sim$ 7.6 nJy, similar to Figure 4.1. The clump structures input into our forward model are labeled in blue in the right panel. The brightest clump at the head of the arc (labeled 1.1) has an observed AB magnitude of $\sim$ 23. The arc contains at least one other clump (1.2) located near the center of the arc. Additional substructures may appear with deeper follow-up imaging.

of $M_{500} = 9 \times 10^{14} M_{\odot}$. Salmon et al., 2020 discovered at 15″ long arc at $z_{phot} = 6.2$ lensed by this cluster and dubbed it the Sunrise Arc, prompting follow-up observations with HST (GO 15842, P.I. Coe). These follow-up images included 5 additional orbits of ACS F814W imaging, and two orbits each of ACS F475W and WFC3/IR F110W imaging. These follow up images are presented in detail in Welch et al. 2022. The Sunrise Arc is shown in Figure 4.1, and each of its 7 small clump structures are identified. Additionally, this arc contains an extremely magnified lensed star presented in Welch et al. 2022. WHL0137–08 received a total of 7 hours of observations in the IRAC 3.6 μm band, and 5 hours in the 4.5μm band.

HST photometry for all sources was measured using Source Extractor v2.19.5 (Bertin and Arnouts, 1996) following the method detailed in Coe et al., 2019. Initial redshifts were measured for all RELICS objects using BPZ (Benítez, 2000; Coe et al., 2006). Further SED modeling was done for SPT0615-JD1 in Salmon et al., 2018 and again in Strait et al., 2020 to further explore its photometric redshift, along with other physical properties. Each method yields a $z \sim 10$ solution ($z_{phot} = 9.9^{+0.8}_{-0.6}$ for Salmon et al. 2018, and $z_{phot} = 10.2^{+1.1}_{-0.5}$ for Strait et al. 2020). We assume a redshift of $z = 9.9$ for relevant calculations in this analysis. Spitzer flux measurements are detailed in Strait et al., 2020; Strait et al., 2021. While Strait et al., 2021 performed many SED fits to high-redshift RELICS galaxies, that paper did not fit the Sunrise Arc or MACS0308-zD1 due to poor constraints on IR fluxes from Spitzer data.

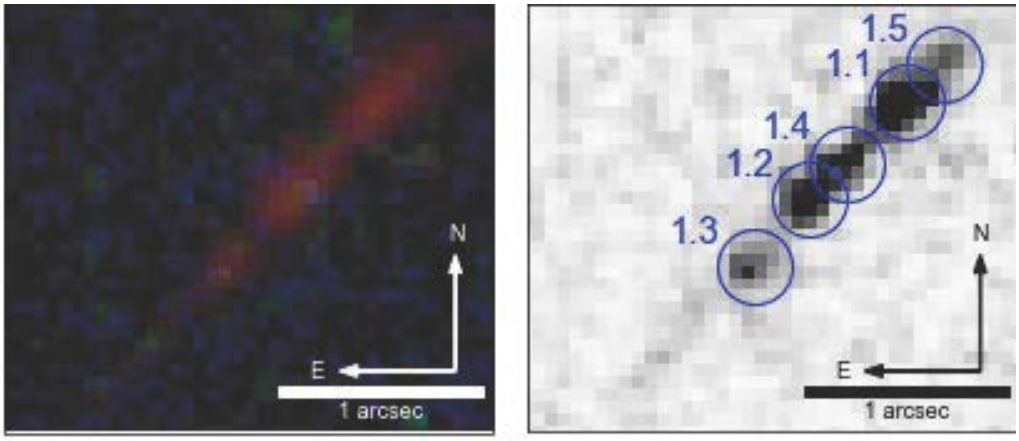

Figure 4.3: The $\sim 2.5''$ long arc SPT0615-JD is the most distant resolved arc observed so far, with multiple photometric redshift estimates putting it solidly at $z \sim 10$. The left panel shows a color composite from HST data, as in previous figures. The right panel shows the F160W band, with each substructure circled and labeled in blue. We identify a total of five clump features within this arc, labeled 1.1 thru 1.5. Clumps 1.1 and 1.5, as well as clumps 1.2 and 1.4, appear blended in our HST images, due to their proximity and resolution limits. Future observations with the higher-resolution JWST will better resolve these structures.

4.3 Lens Models

Proper interpretation of gravitationally lensed galaxies relies on accurate models of the lensing clusters. For our present analysis, we utilize published lens models for each lensing cluster, made using the Lenstool (Jullo et al., 2007; Jullo and Kneib, 2009) and Light-Traces-Mass (LTM; Broadhurst et al. 2005; Zitrin et al. 2009; Zitrin et al. 2015) lens modeling softwares.

4.3.1 WHL0137

WHL0137 has a total of five published lens models made using four different lens modeling tools: Lenstool, LTM, Glafic (Oguri, 2010) and WSLAP+ (Diego et al., 2005; Diego et al., 2007), the details of which can be found in Welch

et al. 2022. For the present analysis, we focus on the LTM model which produces the most accurate reproduction of the full length of the Sunrise Arc. While all models produce a reasonably faithful reproduction of the arc, only LTM simultaneously matches the positions and relative brightnesses of all components. Notably, the Lenstool and Glafic models produce much higher magnifications for clump 1.1b than for clump 1.1a, inconsistent with the observed relative fluxes which are consistent within 1σ uncertainties in each WFC3/IR band. The lens models for WHL0137 are constrained by two photometrically identified multiple image systems: the Sunrise arc at $z \sim 6.2$ as well as a triply-imaged $z \sim 3$ galaxy.

The LTM model predicts magnifications of $\mu \sim 60 - 250$ for individual clumps along the arc. The rapidly changing magnification in the vicinity of lensing critical curves is the cause of this wide range of magnification predictions, and makes setting a fiducial value of magnification for the full arc difficult. Where necessary, we adopt a total magnification of $\mu = 300$ for the full arc (inclusive of all three multiple images) and a magnification of $\mu = 150$ for the most highly stretched central image.

4.3.2 MACS0308

MACS0308 was modeled by Acebron et al., 2018 using the LTM software. The lens model is constrained by three multiple image systems, each photometrically measured at $z \sim 2 - 3$. The bright lensed arc MACS0308-904 is not included as a constraint in the lens modeling due to uncertainties in the validity of its predicted counterimages. Future spectroscopic observations are

needed to confirm these counterimages.

This lens model predicts a lensing magnification of $\mu \sim 20$ for the bright $z \sim 6$ arc. We adopt $\mu = 20$ as our fiducial magnification for analysis of this arc, however given its extended morphology that magnification will change across the length of the arc. Particularly, magnification decreases to the southeast of the brightest clump, meaning the fainter tail of the arc is at lower magnification than the bright clump. While the brightest clump is magnified by a factor 22, the furthest tail of the arc is only magnified by a factor 15. Its potential counterimage has a model predicted magnification of $\mu \sim 2$.

4.3.3 SPT0615

The lens model for SPT0615 was presented in Paterno-Mahler et al., 2018 and utilizes the Lenstool modeling software. This model is constrained by three multiple image families, two of which include spectroscopic redshifts. This lens model predicts a magnification for SPT0615-JD1 of $\mu \sim 4 - 7$, varying along the length of the arc. We adopt a conservative fiducial magnification for the full arc of $\mu = 5$ where necessary. The lens model of Paterno-Mahler et al., 2018 predicts that two additional multiple images of SPT0615-JD1 should be visible. These multiple images have yet to be identified in the HST imaging.

4.4 Clump Modelling

Gravitational lensing can provide a significant boost in resolution, allowing us to probe much smaller physical scales than would be possible in field galaxies. In order to derive the greatest benefit from this increase in resolution, we use a

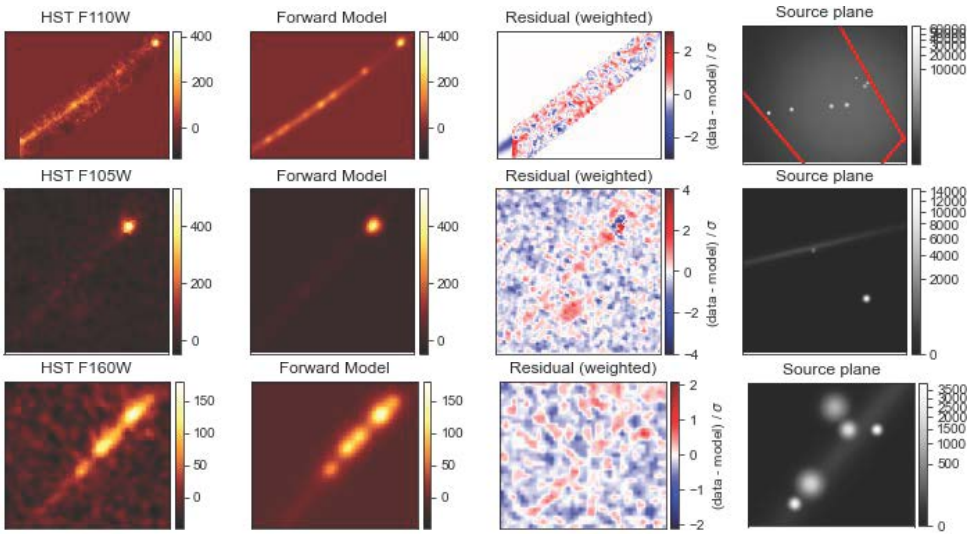

Figure 4.4: Forward model fitting allows detailed study of the substructure of lensed galaxies. Here we show HST images of our lensed arcs (left) along with forward model image plane reconstructions of each arc (left middle). The weighted residuals, calculated by subtracting the model from the data and dividing by pixel-level uncertainty, are shown in the middle right column. The residuals are consistent with noise in each fit, indicating that our forward model is successfully capturing the full arc in each case. The source plane models for each galaxy are shown in the right-hand column. In the top row, the caustic curves are shown in red.

forward modeling technique similar to that described in Johnson et al., 2017b.

In this section, we describe the forward modeling code, as well as the star formation rate estimate we make using its outputs. We then detail the modeling decisions made for each arc individually.

4.4.1 Forward Model

The forward model begins with the creation of a source plane model. This model includes a number of predefined clump structures, along with a larger background structure to represent the diffuse light of the host galaxy. For this analysis, we model each structure with a two-dimensional Gaussian profile,

following Johnson et al., 2017b. Many of the substructures examined here are unresolved or barely resolved, so the simpler Gaussian profile proves sufficient for their characterization. One additional parameter that does noticeably improve the fitting result is the inclusion of ellipticity in the Gaussian profile. In particular for the larger galaxy structure, the elliptical Gaussian is used to best match the shape of the source plane galaxy.

Once a source plane model has been defined, we can create an image plane reconstruction using the lens model deflection maps. This image plane model can then be convolved with an estimated instrument PSF to match the actual HST data. We estimate the PSF using stars observed within our observations. We create a PSF convolution kernel by averaging several stars to account for variations in subpixel position variations. We intentionally avoid particularly bright stars when generating the PSF kernel, as the diffraction spikes around bright stars would overwhelm the instrument PSF and introduce unnecessary noise in our model.

To determine the best model parameters, we perform an initial parameter optimization using a downhill simplex algorithm (using Scipy minimize). This optimization provides an estimate of the parameter values, but no estimate of the variance of each parameter. We therefore next use an MCMC to probe the range of possible solutions and estimate the variance on each model parameter. The MCMC is done using the python package emcee (Foreman-Mackey et al., 2013).

Before fitting, we set flat priors on the amplitude, width, and ellipticity (where necessary) of each Gaussian. The primary function of the priors is

to prevent unphysical solutions. For example, in the case of unresolved structures, the code can produce arbitrarily small point sources that still reproduce the unresolved image. To prevent this behavior, we set a lower limit on the Gaussian width based on the magnification and resolution of the HST images. This cutoff improves our estimates of the upper limits on the radii of unresolved objects.

4.4.2 Star Formation Rate Calculation

The forward model provides a pathway to measure star formation rates for clumps via their UV luminosity. This is particularly useful for faint clumps for which SED fitting does not produce well-constrained results.

We first use the output of the forward model to calculate the delensed flux density from each clump by integrating over the clump profile. In the case of a Gaussian profile, the flux can be calculated as

$$F = 2\pi A \sigma_x \sigma_y \tag{4.1}$$

where A is the Gaussian amplitude, and $\sigma_{x,y}$ are the width in either direction. For symmetric Gaussian profiles, $\sigma_x = \sigma_y$. We then divide this integrated flux by a factor $(1+z)$ to correct for bandwidth compression. From here, we calculate SFRs for each clump using the far-UV luminosity – SFR conversion from Madau and Dickinson, 2014a, namely

$$\mathrm{SFR} = 1.15 \times 10^{-28} L_\nu \tag{4.2}$$

where SFR is in units of $M_\odot$ yr^{-1} and L_ν is in units of ergs s^{-1} Hz^{-1}. This relation assumes a Salpeter IMF, however Madau and Dickinson, 2014a calculate a conversion to Chabrier or Kroupa IMFs can be made by multiplying by a factor $\sim 2/3$.

Calculating SFR from UV light can be significantly impacted by any amount of dust absorption. For these calculations, we assume no dust absorption. SED fitting of each galaxy yields fairly low dust attenuation $A_V < 0.1$ mag, indicating that this assumption is reasonable. Future observations with JWST can improve these estimates by accurately measuring and correcting for the effects of dust absorption.

4.4.3 Individual Arc Modeling

4.4.3.1 Sunrise Arc

The Sunrise Arc consists of three multiple images crossing the lensing critical curve in two places. The central image has the highest overall magnification as it runs roughly parallel to the critical curve. Thus, we use this central image for our forward modeling. This arc is best detected in the deep F110W imaging, so we use this band in our forward model fitting.

We identify a total of seven clump structures within this arc segment, labeled 1.1 through 1.7 (see Figure 4.1). Each clump appears unresolved in the WFC3/IR imaging, showing no deviation from a PSF-like point source when examined independent of the background arc. Thus our radius constraints are upper limits only. The arc contains a measurable diffuse component, which we model as a symmetric Gaussian. The high lensing shear in this region means

that any asymmetry is lost, so the symmetric Gaussian profile is sufficient and reduces the total number of parameters needed for the model.

The length of the arc, coupled with the crowded field in which it is located, lead us to cut out a rectangular region around the arc for fitting purposes. This region removes contamination from nearby cluster galaxies, which can overwhelm the fitting code and produce poor results. We also choose to cut out the lower-redshift interloper that appears at the southeast end of the central image of the arc (see Fig. 4.1). This interloper would bias the size and brightness measurements for clump 7, causing it to favor a larger and brighter model.

The resulting best fit for this arc produces a residual that is consistent with background noise (Figure 4.4).

4.4.3.2 MACS0308-zD1

We identify two clump features in MACS0308-zD1, the bright clump at the head of the arc as well as a small clump in the middle of the diffuse tail. We note that the tail exhibits hints of additional clump structures, however the relatively shallow HST imaging prevents reliable detections and reconstructions of these features. Attempts to fit these structures with our modeling code resulted in null fits, wherein the best fit was a clump too faint to appear in the image. Future deeper imaging with HST or JWST will likely reveal additional structure in the tail of this arc.

We model the diffuse tail as an asymmetric Gaussian. Due to the faintness of the tail, the diffuse component has high uncertainties compared to the

better-constrained clumps.

We note that the bright clump at the head of the arc appears to have additional structure beyond the Gaussian we use for fitting, particularly a protrusion off the north edge of the clump. We did attempt to model this protrusion, however we found it to be highly degenerate with the main clump, leading to increased uncertainties on both clump parameters without a noticeable decrease in residuals. We thus choose to only include one component to describe the bright clump, however future work may include additional detail in this object.

4.4.3.3 SPT0615-JD1

We identify a total of five clump structures within the SPT0615-JD1 arc using the WFC3/IR F160W image. The arc includes three clear features, however the brightest two of these three features appear asymmetrically bright in the HST images. We thus determine that these asymmetric clumps are likely blended images of multiple smaller structures. Previous studies of highly lensed galaxies have found that many small clumps will appear as such asymmetric larger structures when simulated at lower lensing magnification, supporting our determination to model the arc as multiple smaller clumps (Rigby et al., 2017). Including the two additional clumps to describe this arc does introduce some degeneracy between clumps, increasing uncertainties in clump properties. However, the inclusion of these additional structures leads to noticeable improvement in the residuals, indicating that the added complexity and degeneracy does improve the final fit.

Filter	Sunrise Arc Flux (nJy)	MACS0308-zD1 Flux (nJy)	MACS-1.1 Flux (nJy)	SPT0615-JD1 Flux (nJy)
F435W	-69 ± 56	184 ± 64	88 ± 50	-27 ± 20
F475W	16 ± 27			
F606W	-51 ± 33	-19 ± 34	-44 ± 27	32 ± 12
F814W	312 ± 21	426 ± 50	325 ± 39	-13 ± 10
F105W	1321 ± 74	2250 ± 61	1740 ± 49	21 ± 16
F110W	1187 ± 21			
F125W	1351 ± 137	2483 ± 104	1901 ± 81	70 ± 15
F140W	1197 ± 109	2116 ± 83	1625 ± 65	233 ± 10
F160W	1088 ± 74	2102 ± 56	1646 ± 45	352 ± 13
IRAC Ch.1				29 ± 9
IRAC Ch.2				50 ± 15

Table 4.1: Photometry from HST and Spitzer for each arc and the bright clump of MACS0308-zD1 used for SED fitting.

There is a diffuse component to this arc, however it is very faint. We included this in our model, however it is poorly constrained due to its faintness. Deeper imaging of this galaxy with either HST of JWST will better measure the full extent of the arc and allow for an improved model of its structure.

4.5 SED Fitting

To better understand the properties of the arcs presented here, we perform SED fitting based on available HST and Spitzer photometry. We use the SED fitting code BAGPIPES (Carnall et al., 2018) to fit our photometric data, leaving redshift as a free parameter. Because each of these objects has a solid photometric redshift estimate in place, we set redshift range in our fitting of $4 < z < 15$. Previous works (Welch et al. 2022; Strait et al. 2020; Salmon et al. 2018) have investigated and ruled out lower redshift solutions, justifying our restricted redshift range.

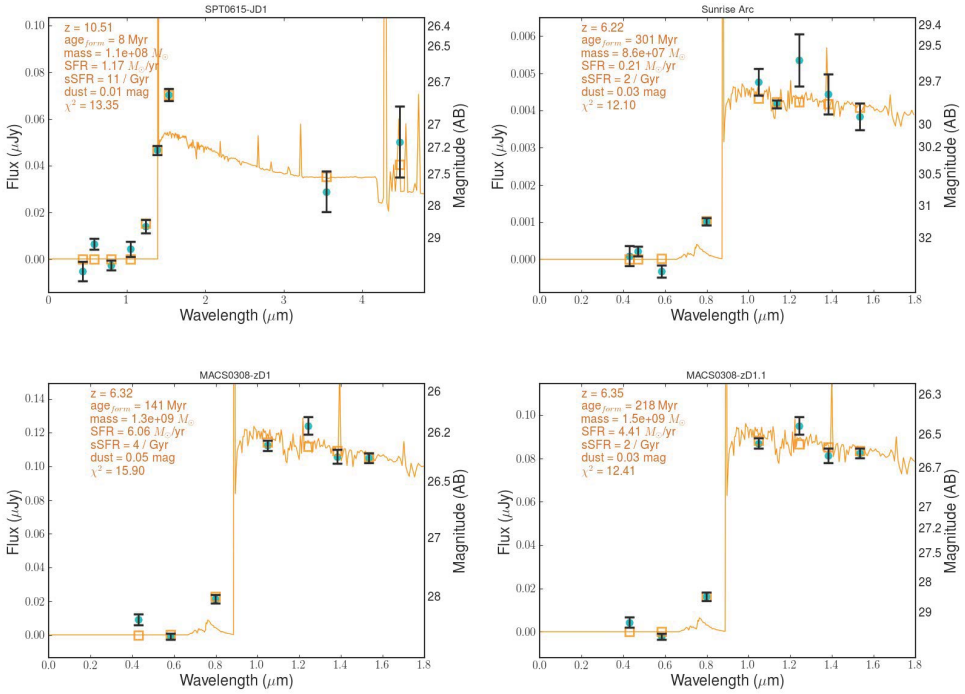

Figure 4.5: SED fits for each galaxy considered are shown. We additionally show the SED fit to the bright clump of MACS0308-zD1 independently in the lower right panel. With current data, the SFR for each full galaxy can be fairly well constrained. Parameters such as age require additional wavelength coverage to yield strong constraints.

We use the BAGPIPES default stellar population models from Bruzual and Charlot, 2003, coupled with nebular reprocessing implemented by the photoionization code CLOUDY (Ferland et al., 2017). We model each galaxy with an exponential star formation history of the form $SFR \propto e^{-t/\tau}$, allowing τ to vary from 100 Myr to 10 Gyr. Metallicity is allowed to vary from 0 to $2.5Z_{\odot}$, while stellar mass is left with a wide parameter space of $1 < \log(M_*/M_{\odot}) < 15$. Age is varied from 1 Myr to the age of the universe, and ionization parameter is varied over the range $-4 < \log(U) < -2$. Dust extinction is implemented using the Calzetti et al., 2000 law with $A_V < 3$, and we assume that dust extinction is twice as high around HII regions in the first 10 Myr of their lifetimes.

Each of these lensed arcs was detected as a series of multiple source segments in Source Extractor, so to perform SED fitting of the full arcs we sum the flux from these segments, as well as summing the uncertainties in quadrature. To estimate the intrinsic (delensed) properties of each galaxy, we divide by a fiducial magnification for each arc. The fiducial magnifications are discussed in Section 4.3. The actual magnifications will vary across the length of each arc. For MACS0308-zD1 and SPT0615-JD1, the changes are moderate from one end of the arc to the other, varying from $\mu = 15 - 22$ for MACS0308-zD1, and from $\mu = 5 - 6$ for SPT0615-JD1. For the Sunrise Arc, the proximity of the arc to the critical curve creates significant differences in magnification from one end to the other. Particularly, for the central image used in forward modeling, the magnification varies from over 200 near the ends of the image to around 60 in the center. Adopting a total magnification for this central image based on

the average magnification of clumps within the arc (giving our fiducial magnification of 150) attempts to correct for this effect. However the magnitude of the differential magnification in this arc leads to some discrepancies between the forward model results and the full arc results, explaining the difference seen in Table 4.2.

To get physical parameter estimates for each clump, we scale SED fitting results from the full arc down based on flux ratios. For example, if a clump provides 10% of the flux of a given arc, the resulting clump SFR and stellar mass will be 10% of the total. We did attempt to fit clumps individually, however we were only able to get a reliable fit for the bright clump of MACS0308-zD. The clumps of the Sunrise Arc, as well as the fainter clump of MACS0308-zD, were too faint to effectively constrain physical parameter values. While the code produced output values for each, fractional uncertainties reached near 100%. Additionally, the $z \sim 10$ arc SPT0615-JD cannot effectively constrain physical parameters (besides redshift) with HST data alone, and Spitzer fluxes could not be reliably extracted for each individual clump. Future, deeper observations with HST of JWST will enable more detailed study of each individual substructure in these galaxies.

4.6 Results

4.6.1 Forward Model Radii and SFRs

Our forward modeling analysis produces direct constraints on clump radii in the source plane, which are presented in Table 4.2. For the Sunrise Arc, each clump appears unresolved in the image plane (PSF-like), so we can only set

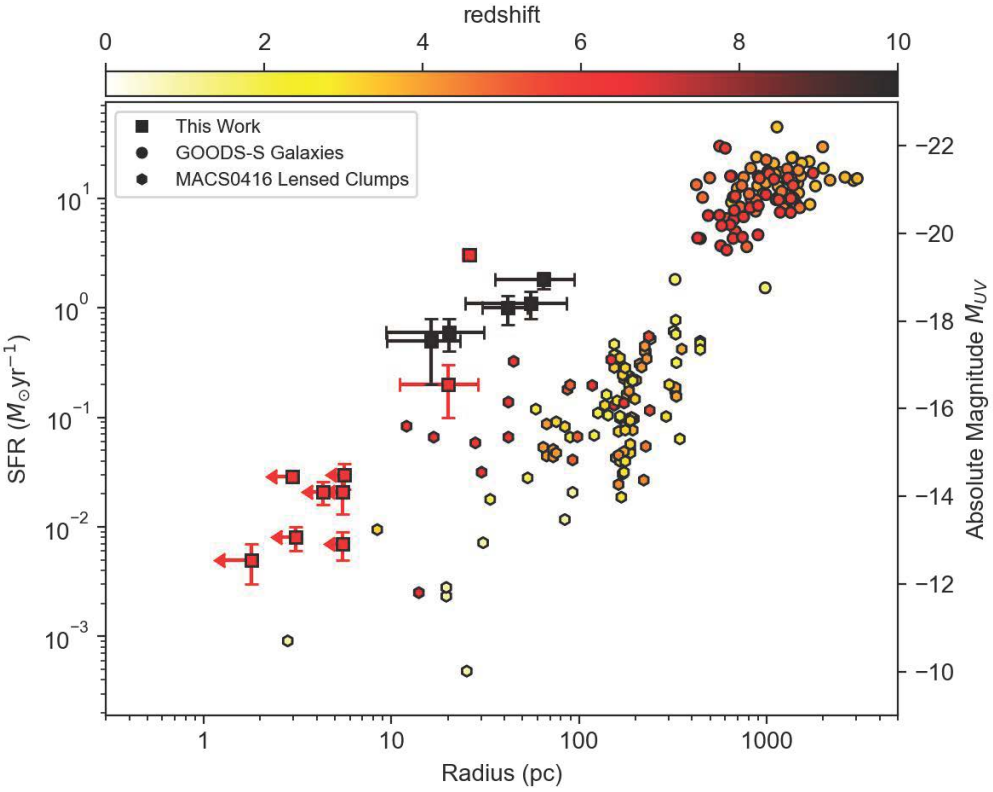

Figure 4.6: Star formation rates and radii of galaxy substructures from this work (plotted as squares with error bars) and Vanzella et al., 2021 (plotted as hexagons). Additionally, full galaxies from GOODS-S are shown as (plotted as circles, Vanzella et al., 2009; Giavalisco et al., 2004). The clumps presented here probe the smallest physical scales yet examined at $z > 6$ and $z \sim 10$. Additionally, many of the clumps have particularly high star formation rates given their sizes. These properties are similar to what is seen in local young massive star clusters.

upper limits on their sizes. The upper limits indicate that these are some of the most compact structures thus far observed at $z \sim 6$, as most have 68% confidence radius limits less than 5 pc, and 95% confidence limits less than 10 pc. Previously, Vanzella et al., 2019 reported a cluster with upper limit $r < 13$ pc, meanwhile smaller clumps at scales of a few parsecs have been found in low-redshift galaxies (Portegies Zwart, McMillan, and Gieles, 2010). Radii for clumps in the other arcs are not so compact, they are at scales of a few tens of parsecs each. These galaxies are not as highly magnified, meaning they may host smaller star clusters but those structures cannot be resolved with HST imaging. In particular, the $z \sim 10$ arc SPT0615-JD1 may include more, smaller clump structures which are blended together to form the larger clumps measured. Future higher resolution imaging, for example with JWST, would better resolve these clumps and improve constraints on their radii.

Our forward model provides a useful estimate of star formation rates for each clump based on best-fit intrinsic UV brightness. The SFRs for each clump are listed in Table 4.2, along with their intrinsic UV absolute magnitudes. The SFR is shown plotted against clump radius in Figure 4.6, along with a selection of clumps and full galaxies from previous literature, representing typical high-redshift galaxies in both lensed and blank fields (Vanzella et al., 2020; Vanzella et al., 2009; Giavalisco et al., 2004). The clumps presented here stand out as some of the smallest clumps known at high redshift, as well as having the highest star formation rates for their size. From the combination of SFR and clump radius, we can calculate the surface density of star formation for each clump as $\Sigma_{\rm SFR} = (0.68 * {\rm SFR})/(\pi r^2)$, where the factor 0.68 accounts

for the fact that the radius is given by the σ of a Gaussian profile, yet the full profile integrated to infinity is used to calculate the SFR. From this calculation, we see that the Σ_{SFR} is highest in the bright clump of MACS0308-zD1.1, followed by the brightest clump of the Sunrise Arc (1.1). Each of these show SFR densities greater than 1000 $M_{\odot}$ yr^{-1} kpc^{-2}, notably higher than other clumps analyzed here, indicating that these are particularly dense star forming systems. The remainder of the clumps have SFR densities of order a few hundred $M_{\odot}$ yr^{-1} kpc^{-2}. It is worth noting that the values of Σ_{SFR} for the Sunrise Arc clumps are best interpreted as lower limits, as the clumps are unresolved in HST imaging. If the true radii of these clumps turn out to be smaller than the constraints presented here, they will in turn show higher SFR surface densities.

4.6.2 BAGPIPES Results

We can further assess physical parameters of these galaxies using SED fits. We fit the combined flux of each arc using BAGPIPES, and the resulting parameters are presented in Table 4.3. We attempted to fit each clump individually, however this only worked for MACS0308-zD 1.1, as it is a very bright object. The rest of the clumps proved too faint to yield reliable results from SED fitting.

The SED fitting provides estimates of stellar mass, which the forward modeling cannot. The mass measurement for MACS0308-zD1.1 suggests this clump is particularly dense, with a high stellar mass packed into a small region. Using the combination of stellar mass and radius, we can calculate

a crossing time for each clump following Equation 1 of Gieles and Portegies Zwart, 2011. These results are also shown in Table 4.3. The crossing time for MACS0308-zD1.1 is less than 1 Myr, potentially indicating that they could be gravitationally bound as its age is likely greater than 1 Myr at $z \sim 6$. However, this is speculation until proper ages can be measured with JWST. Stellar population ages are poorly constrained with only the rest-frame UV available to constrain our SED fits. We do report best-fit ages for each galaxy, however we note that the uncertainties on these values are large given the limited wavelength coverage of our current observations.

4.7 Discussion

4.7.1 Compact Star Formation at High-z

The star forming clumps presented in this paper are notably compact, particularly within the Sunrise Arc. These clumps each have upper limit radii of below 12 pc, which makes them the smallest limits on clump sizes thus far observed at $z > 6$, smaller than the previous record of $r < 13$ pc presented in Vanzella et al., 2019. These small radii put the clumps of the Sunrise Arc squarely in the regime of Young Massive Clusters (YMCs), which have been measured with radii as small as $\sim$ 1 pc (Portegies Zwart, McMillan, and Gieles, 2010; Ryon et al., 2017). YMCs in turn are thought to be precursors to globular clusters (e.g., Terlevich et al., 2018), however there is some debate on this topic as local YMCs have not been found to contain multiple stellar populations indicative of globular clusters (Bastian and Lardo, 2018). Either way, the presence of seven highly magnified YMCs in a galaxy at $z > 6$ present

Clump	Magnif. μ	Radius pc	M_{UV}	SFR $M_\odot$ yr^{-1}	$\Sigma_{\rm SFR}$ $M_\odot$ yr^{-1} kpc^{-2}
WHL*			-16.95 ± 0.03	0.287 ± 0.007	
1.1	215 ± 40	$\leq 3.0(3.1)$	-14.5 ± 0.1	0.029 ± 0.003	753 ± 13
1.2	97 ± 9	$\leq 4.3(5.3)$	-14.1 ± 0.3	0.021 ± 0.005	280 ± 30
1.3	63 ± 6	$\leq 5.5(8.4)$	-14.1 ± 0.4	0.021 ± 0.008	200 ± 50
1.4	79 ± 8	$\leq 5.6(9.6)$	-14.5 ± 0.3	0.03 ± 0.008	240 ± 80
1.5	160 ± 30	$\leq 1.8(2.4)$	-12.4 ± 0.4	0.005 ± 0.002	380 ± 50
1.6	180 ± 50	$\leq 5.5(11.6)$	-12.9 ± 0.5	0.007 ± 0.003	80 ± 30
1.7	250 ± 160	$\leq 3.1(3.8)$	-13.1 ± 0.3	0.008 ± 0.002	210 ± 40
Diffuse		204 ± 26	-17.3 ± 0.1	0.41 ± 0.04	2.0 ± 0.4
MACS			-20.55 ± 0.03	7.9 ± 0.2	
1.1	22	26 ± 2	-19.51 ± 0.05	3.05 ± 0.13	1000^{+150}_{-110}
1.2	16	20 ± 9	-16.7 ± 0.6	0.2 ± 0.1	110^{+100}_{-50}
Diffuse		900^{+5700}_{-300}	$-19.3^{+0.3}_{-1.8}$		
SPT			-20.73 ± 0.03	9.35 ± 0.34	
1.1	5.1	65 ± 6	-19.0 ± 0.2	1.9 ± 0.3	102^{+2}_{-14}
1.2	5.4	40 ± 7	-18.3 ± 0.3	1.0 ± 0.3	131^{+13}_{-3}
1.3	5.5	23 ± 6	-17.7 ± 0.6	0.6 ± 0.3	232^{+8}_{-2}
1.4	5.3	73 ± 23	-18.6 ± 0.3	1.3 ± 0.3	58^{+7}_{-32}
1.5	5.0	30 ± 6	-18.0 ± 0.4	0.8 ± 0.3	198^{+10}_{-26}
Diffuse		450^{+700}_{-390}	-18.0 ± 0.4		

Table 4.2: Forward model results are presented for each clump, as well as the diffuse background arc where applicable. Arc names are abbreviated: WHL is WHL0137-zD1, MACS is MACS0308-zD1, and SPT is SPT0615-JD1. For the Sunrise Arc, radius upper limits are quoted at the 68% (95%) confidence interval. All other uncertainties are quoted at the 1σ level. SFR presented in this table is calculated from the delensed UV luminosity, as discussed in the text. Quantities presented here were derived assuming a fixed lens model magnification.

* Quantities for the Sunrise Arc are shown for the central lensed image only, for consistency with forward modeling results.

Clump	Flux nJy	Fraction	SFR $M_\odot$ yr^{-1}	$\log(M_*)$ Myr	Age
Sunrise Arc*	626 ± 15		$0.27^{+0.11}_{-0.05}$	$7.9^{+0.2}_{-0.3}$	400^{+300}_{-200}
MACS0308-zD	2250 ± 60		$6.3^{+1.6}_{-0.7}$	$9.2^{+0.2}_{-0.3}$	370^{+280}_{-220}
1.1	1740 ± 50		$4.9^{+1.2}_{-0.6}$	$9.1^{+0.2}_{-0.3}$	350^{+310}_{-200}
SPT0615-JD1	352 ± 13		$4.9^{+1.9}_{-2.3}$	8.6 ± 0.3	70^{+120}_{-40}

Table 4.3: SED fitting results for each arc are shown, along with quantities inferred for each clump. SFR and stellar mass are scaled based on relative fluxes, which are shown for the bandpass used in forward model fitting (F110W, F105W, and F160W respectively for the Sunrise Arc, MACS0308-zD, and SPT0615-JD). As in Table 4.2, values for the Sunrise Arc are shown for the central image only for ease of comparison with forward model results.
* Quantities for the Sunrise Arc are shown for the central lensed image only, for consistency with forward modeling results.

a great opportunity to study high redshift star clusters in detail with future JWST observations.

The star clusters measured in MACS0308-zD and SPT0615-JD1 are somewhat larger than those in the Sunrise Arc, with radii measuring tens of parsecs. This puts these clumps on the larger end of the YMC scale based solely on radius (Portegies Zwart, McMillan, and Gieles, 2010). It is worth noting that the clumps in SPT0615-JD1 may intrinsically be smaller than what is measured here. This arc is at a lower magnification ($\mu \sim 5$) than the other two, and its morphology shows fewer clearly distinguished features. This is indicative of multiple smaller clumps blending together to form the structures we observe (as in e.g., Rigby et al., 2017). We attempt to model this blending using multiple smaller structures to model the clumps in this arc, but ultimately higher resolution imaging will be needed to better constrain the clump sizes.

Our forward modeling provides a measure of intrinsic luminosity, which

can be used to calculate SFR via the scaling relation in Madau and Dickinson, 2014b. The resulting SFRs are rather high for each clump given their radii, indicating that these clumps host intense star formation. To quantify this, we calculate the SFR surface density (SFRSD) using the measured radius and SFR, finding generally high SFRSDs in each clump. In particular, clump 1.1 of MACS0308-zD has $\Sigma_{SFR} = 10^3 M_\odot$ yr^{-1} kpc^{-2}, nearing the upper edge of the Kennicutt-Schmidt relation (Kennicutt, 1998), and the regime of maximal Eddington-limited star formation rate calculated by Crocker et al., 2018. The clumps of the Sunrise Arc generally have SFRSDs of a few hundred $M_\odot$ yr^{-1} kpc^{-2}, which is still quite high. Clump 1.1 in the Sunrise Arc in particular has $\Sigma_{SFR} = 750$, similar to that measured for the clump D1(core) discussed in Vanzella et al., 2019. These SFRSDs are also consistent with dense star clusters observed locally (e.g., Adamo et al., 2017; Ryon et al., 2017). We note however that the $L_{UV}-$SFR relation of Madau and Dickinson, 2014b may break down for the clumps of the Sunrise Arc. These clumps show particularly low SFRs, which means that stochastic star formation effects become a greater source of uncertainty, resulting in larger scatter in the $L_{UV}-$SFR relation (da Silva, Fumagalli, and Krumholz, 2012; da Silva, Fumagalli, and Krumholz, 2014; Vikaeus, Zackrisson, and Binggeli, 2020).

One particularly interesting question for these YMCs in the early universe is whether they remain bound, going on to form globular clusters, or if they disperse either through tidal disruption or stellar feedback. Simulations of larger (100-1000 pc) clumps in galaxies at $z \sim 2$ have found that these structures tend to be disrupted either by stellar feedback or gravitational

interactions within a few hundred Myr at most (Oklopčić et al., 2017; Meng and Gnedin, 2020). However, other simulations have found that more massive gravitationally bound clumps can survive long-term, forming bound globular clusters (Mandelker et al., 2017). The best way to determine if a cluster is bound is to compare its crossing time t_{cross} to its age. The ratio of these quantities can provide a useful metric for the boundedness of star clusters, as if a cluster has survived for many crossing times, it is likely gravitationally bound. (Gieles and Portegies Zwart, 2011; Bastian et al., 2012). Our current data can only provide an estimate of the crossing time for the brightest clump in MACS0308-zD1, which has a crossing time of $0.6^{+0.3}_{-0.2}$ Myr. Other clumps are too faint to get individual SED fits, meaning that we cannot estimate their stellar masses and ages. We also note that our SED fits are constrained by the limited IR wavelength coverage of HST, which leaves considerable uncertainty on the galaxy and clump ages. Despite this limitation, we find that MACS0308-zD1 has a crossing time less than 1 Myr, potentially suggesting it may turn out to be gravitationally bound. This short crossing time is due to both the small radius and the fairly high inferred stellar mass of this clump.

4.8 Conclusions

We present observations of three superlative arcs from the RELICS survey. These include the longest $z \sim 6$ arc (Sunrise), the brightest $z \sim 6$ arc (MACS0308-zD1), and the most distant resolved arc at $z \sim 10$ (SPT0615-JD1). Each of these arcs shows clear substructure on scales ranging from tens of parsecs down to a few parsecs. Most of the clumps are likely YMCs, and they all exhibit high star

formation rates compared to their small sizes. Future observations with JWST will provide greater detail on the inner workings of these superlative lensed galaxies, including determinations of clump ages which in turn determine whether or not a clump is gravitationally bound. In particular, an accepted JWST Cycle 1 program (GO-2282) will obtain spectra of many star clusters within the Sunrise Arc, allowing more accurate measures of star formation rates and ages. Beyond that, these observations will measure metallicities, and could constrain ionization parameters for each star cluster. Together, these observations will better constrain the formation and environment within this $z \sim 6$ galaxy. Similar spectroscopic observations of the other galaxies mentioned herein will be similarly beneficial, providing better constraints on all parameters presented here as well as new measurements of other physical parameters. These galaxies will be excellent targets for future observations with JWST as well as other observatories.

References

Shibuya, Takatoshi, Masami Ouchi, and Yuichi Harikane (2015). "Morphologies of ∼190,000 Galaxies at z = 0-10 Revealed with HST Legacy Data. I. Size Evolution". In: *ApJS* 219.2, 15, p. 15. DOI: 10.1088/0067-0049/219/2/15. arXiv: 1503.07481 [astro-ph.GA].

Shibuya, Takatoshi, Masami Ouchi, Yuichi Harikane, and Kimihiko Nakajima (2019). "Morphologies of ∼190,000 Galaxies at z = 0-10 Revealed with HST Legacy Data. III. Continuum Profile and Size Evolution of Lyα Emitters". In: *ApJ* 871.2, 164, p. 164. DOI: 10.3847/1538-4357/aaf64b. arXiv: 1809.00765 [astro-ph.GA].

Mowla, Lamiya A., Pieter van Dokkum, Gabriel B. Brammer, Ivelina Momcheva, Arjen van der Wel, Katherine Whitaker, Erica Nelson, Rachel Bezanson, Adam Muzzin, Marijn Franx, John MacKenty, Joel Leja, Mariska Kriek, and Danilo Marchesini (2019). "COSMOS-DASH: The Evolution of the Galaxy Size-Mass Relation since z $\sim$ 3 from New Wide-field WFC3 Imaging Combined with CANDELS/3D-HST". In: *ApJ* 880.1, 57, p. 57. DOI: 10.3847/1538-4357/ab290a. arXiv: 1808.04379 [astro-ph.GA].

Neufeld, Chloe, Victoria Strait, Maruša Bradač, Brian C. Lemaux, Dan Coe, Lilan Yang, Tommaso Treu, Adi Zitrin, Mario Nonino, Larry Bradley, and Keren Sharon (2021). "RELICS: Small Lensed $z \geq 5.5$ Galaxies Selected as Potential Lyman Continuum Leakers". In: *arXiv e-prints*, arXiv:2111.14882, arXiv:2111.14882. arXiv: 2111.14882 [astro-ph.GA].

Shibuya, Takatoshi, Masami Ouchi, Mariko Kubo, and Yuichi Harikane (2016). "Morphologies of ∼190,000 Galaxies at z = 0-10 Revealed with HST Legacy Data. II. Evolution of Clumpy Galaxies". In: *ApJ* 821.2, 72, p. 72. DOI: 10.3847/0004-637X/821/2/72. arXiv: 1511.07054 [astro-ph.GA].

Elmegreen, Bruce G. and Debra Meloy Elmegreen (2005). "Stellar Populations in 10 Clump-Cluster Galaxies of the Hubble Ultra Deep Field". In: *ApJ* 627.2, pp. 632–646. DOI: 10.1086/430514. arXiv: astro-ph/0504032 [astro-ph].

Elmegreen, Debra Meloy, Bruce G. Elmegreen, Swara Ravindranath, and Daniel A. Coe (2007). "Resolved Galaxies in the Hubble Ultra Deep Field: Star Formation in Disks at High Redshift". In: *ApJ* 658.2, pp. 763–777. DOI: 10.1086/511667. arXiv: astro-ph/0701121 [astro-ph].

Elmegreen, Bruce G., Debra Meloy Elmegreen, Maria Ximena Fernandez, and Jenna Jo Lemonias (2009). "Bulge and Clump Evolution in Hubble Ultra Deep Field Clump Clusters, Chains and Spiral Galaxies". In: *ApJ* 692.1, pp. 12–31. DOI: 10.1088/0004-637X/692/1/12. arXiv: 0810.5404 [astro-ph].

Guo, Yicheng, Mauro Giavalisco, Paolo Cassata, Henry C. Ferguson, Mark Dickinson, Alvio Renzini, Anton Koekemoer, Norman A. Grogin, Casey Papovich, Elena Tundo, Adriano Fontana, Jennifer M. Lotz, and Sara Salimbeni (2011). "Color and Stellar Population Gradients in Passively Evolving Galaxies at z ∼2 from HST/WFC3 Deep Imaging in the Hubble Ultra Deep Field". In: *ApJ* 735.1, 18, p. 18. DOI: 10.1088/0004-637X/735/1/18. arXiv: 1101.0843 [astro-ph.CO].

Genzel, R., S. Newman, T. Jones, N. M. Förster Schreiber, K. Shapiro, S. Genel, S. J. Lilly, A. Renzini, L. J. Tacconi, N. Bouché, A. Burkert, G. Cresci, P. Buschkamp, C. M. Carollo, D. Ceverino, R. Davies, A. Dekel, F. Eisenhauer, E. Hicks, J. Kurk, D. Lutz, C. Mancini, T. Naab, Y. Peng, A. Sternberg, D. Vergani, and G. Zamorani (2011). "The Sins Survey of z ∼2 Galaxy Kinematics: Properties of the Giant Star-forming Clumps". In: *ApJ* 733.2, 101, p. 101. DOI: 10.1088/0004-637X/733/2/101. arXiv: 1011.5360 [astro-ph.CO].

Förster Schreiber, N. M., A. E. Shapley, R. Genzel, N. Bouché, G. Cresci, R. Davies, D. K. Erb, S. Genel, D. Lutz, S. Newman, K. L. Shapiro, C. C. Steidel, A. Sternberg, and L. J. Tacconi (2011). "Constraints on the Assembly and Dynamics of Galaxies. II. Properties of Kiloparsec-scale Clumps in Rest-frame Optical Emission of z ∼2 Star-forming Galaxies". In: *ApJ* 739.1, 45, p. 45. DOI: 10.1088/0004-637X/739/1/45. arXiv: 1104.0248 [astro-ph.CO].

Guo, Yicheng, Henry C. Ferguson, Eric F. Bell, David C. Koo, Christopher J. Conselice, Mauro Giavalisco, Susan Kassin, Yu Lu, Ray Lucas, Nir Mandelker, Daniel M. McIntosh, Joel R. Primack, Swara Ravindranath, Guillermo Barro, Daniel Ceverino, Avishai Dekel, Sandra M. Faber, Jerome J. Fang, Anton M. Koekemoer, Kai Noeske, Marc Rafelski, and Amber Straughn (2015). "Clumpy Galaxies in CANDELS. I. The Definition of UV Clumps and the Fraction of Clumpy Galaxies at $0.5 < z < 3$". In: *ApJ*

800.1, 39, p. 39. DOI: 10.1088/0004-637X/800/1/39. arXiv: 1410.7398 [astro-ph.GA].

Guo, Yicheng, Marc Rafelski, Eric F. Bell, Christopher J. Conselice, Avishai Dekel, S. M. Faber, Mauro Giavalisco, Anton M. Koekemoer, David C. Koo, Yu Lu, Nir Mandelker, Joel R. Primack, Daniel Ceverino, Duilia F. de Mello, Henry C. Ferguson, Nimish Hathi, Dale Kocevski, Ray A. Lucas, Pablo G. Pérez-González, Swara Ravindranath, Emmaris Soto, Amber Straughn, and Weichen Wang (2018). "Clumpy Galaxies in CANDELS. II. Physical Properties of UV-bright Clumps at $0.5 \leq z < 3$". In: *ApJ* 853.2, 108, p. 108. DOI: 10.3847/1538-4357/aaa018. arXiv: 1712.01858 [astro-ph.GA].

Jones, T. A., A. M. Swinbank, R. S. Ellis, J. Richard, and D. P. Stark (2010). "Resolved spectroscopy of gravitationally lensed galaxies: recovering coherent velocity fields in subluminous z ∼2-3 galaxies". In: *MNRAS* 404.3, pp. 1247–1262. DOI: 10.1111/j.1365-2966.2010.16378.x. arXiv: 0910.4488 [astro-ph.CO].

Livermore, R. C., T. Jones, J. Richard, R. G. Bower, R. S. Ellis, A. M. Swinbank, J. R. Rigby, Ian Smail, S. Arribas, J. Rodriguez Zaurin, L. Colina, H. Ebeling, and R. A. Crain (2012). "Hubble Space Telescope Hα imaging of star-forming galaxies at z 1-1.5: evolution in the size and luminosity of giant H II regions". In: *MNRAS* 427.1, pp. 688–702. DOI: 10.1111/j.1365-2966.2012.21900.x. arXiv: 1209.5741 [astro-ph.CO].

Wuyts, Eva, Jane R. Rigby, Michael D. Gladders, and Keren Sharon (2014). "A Magnified View of the Kinematics and Morphology of RCSGA 032727-132609: Zooming in on a Merger at z = 1.7". In: *ApJ* 781.2, 61, p. 61. DOI: 10.1088/0004-637X/781/2/61. arXiv: 1312.1564 [astro-ph.GA].

Livermore, R. C., T. A. Jones, J. Richard, R. G. Bower, A. M. Swinbank, T. T. Yuan, A. C. Edge, R. S. Ellis, L. J. Kewley, Ian Smail, K. E. K. Coppin, and H. Ebeling (2015). "Resolved spectroscopy of gravitationally lensed galaxies: global dynamics and star-forming clumps on ∼100 pc scales at $1 < z < 4$". In: *MNRAS* 450.2, pp. 1812–1835. DOI: 10.1093/mnras/stv686. arXiv: 1503.07873 [astro-ph.GA].

Vanzella, E., F. Calura, M. Meneghetti, A. Mercurio, M. Castellano, G. B. Caminha, I. Balestra, P. Rosati, P. Tozzi, S. De Barros, A. Grazian, A. D'Ercole, L. Ciotti, K. Caputi, C. Grillo, E. Merlin, L. Pentericci, A. Fontana, S. Cristiani, and D. Coe (2017a). "Paving the way for the JWST: witnessing globular cluster formation at $z > 3$". In: *MNRAS* 467.4, pp. 4304–4321. DOI: 10.1093/mnras/stx351. arXiv: 1612.01526 [astro-ph.GA].

Vanzella, E., M. Castellano, M. Meneghetti, A. Mercurio, G. B. Caminha, G. Cupani, F. Calura, L. Christensen, E. Merlin, P. Rosati, M. Gronke, M. Dijkstra, M. Mignoli, R. Gilli, S. De Barros, K. Caputi, C. Grillo, I. Balestra, S. Cristiani, M. Nonino, E. Giallongo, A. Grazian, L. Pentericci, A. Fontana, A. Comastri, C. Vignali, G. Zamorani, M. Brusa, P. Bergamini, and P. Tozzi (2017b). "Magnifying the Early Episodes of Star Formation: Super Star Clusters at Cosmological Distances". In: *ApJ* 842.1, 47, p. 47. DOI: 10.3847/1538-4357/aa74ae. arXiv: 1703.02044 [astro-ph.GA].

Johnson, Traci L., Jane R. Rigby, Keren Sharon, Michael D. Gladders, Michael Florian, Matthew B. Bayliss, Eva Wuyts, Katherine E. Whitaker, Rachael Livermore, and Katherine T. Murray (2017a). "Star Formation at z = 2.481 in the Lensed Galaxy SDSS J1110+6459: Star Formation Down to 30 pc Scales". In: *ApJL* 843.2, L21, p. L21. DOI: 10.3847/2041-8213/aa7516. arXiv: 1707.00706 [astro-ph.GA].

Zick, Tom O., Daniel R. Weisz, Bruno Ribeiro, Mariska T. Kriek, Benjamin D. Johnson, Xiangcheng Ma, and Rychard Bouwens (2020). "Towards studying hierarchical assembly in real time: a Milky Way progenitor galaxy at z = 2.36 under the microscope". In: *MNRAS* 493.4, pp. 5653–5661. DOI: 10.1093/mnras/staa543. arXiv: 2002.07822 [astro-ph.GA].

Dessauges-Zavadsky, Miroslava, Daniel Schaerer, Antonio Cava, Lucio Mayer, and Valentina Tamburello (2017). "On the Stellar Masses of Giant Clumps in Distant Star-forming Galaxies". In: *ApJL* 836.2, L22, p. L22. DOI: 10.3847/2041-8213/aa5d52. arXiv: 1702.00055 [astro-ph.GA].

Cava, Antonio, Daniel Schaerer, Johan Richard, Pablo G. Pérez-González, Miroslava Dessauges-Zavadsky, Lucio Mayer, and Valentina Tamburello (2018). "The nature of giant clumps in distant galaxies probed by the anatomy of the cosmic snake". In: *Nature Astronomy* 2, pp. 76–82. DOI: 10.1038/s41550-017-0295-x. arXiv: 1711.03977 [astro-ph.GA].

Mandelker, Nir, Avishai Dekel, Daniel Ceverino, Dylan Tweed, Christopher E. Moody, and Joel Primack (2014). "The population of giant clumps in simulated high-z galaxies: in situ and ex situ migration and survival". In: *MNRAS* 443.4, pp. 3675–3702. DOI: 10.1093/mnras/stu1340. arXiv: 1311.0013 [astro-ph.CO].

Tamburello, Valentina, Lucio Mayer, Sijing Shen, and James Wadsley (2015). "A lower fragmentation mass scale in high-redshift galaxies and its implications on giant clumps: a systematic numerical study". In: *MNRAS* 453.3, pp. 2490–2514. DOI: 10.1093/mnras/stv1695. arXiv: 1412.3319 [astro-ph.GA].

Mandelker, Nir, Avishai Dekel, Daniel Ceverino, Colin DeGraf, Yicheng Guo, and Joel Primack (2017). "Giant clumps in simulated high- z Galaxies: properties, evolution and dependence on feedback". In: *MNRAS* 464.1, pp. 635–665. DOI: 10.1093/mnras/stw2358. arXiv: 1512.08791 [astro-ph.GA].

Oklopčić, Antonija, Philip F. Hopkins, Robert Feldmann, Dušan Kereš, Claude-André Faucher-Giguère, and Norman Murray (2017). "Giant clumps in the FIRE simulations: a case study of a massive high-redshift galaxy". In: *MNRAS* 465.1, pp. 952–969. DOI: 10.1093/mnras/stw2754. arXiv: 1603.03778 [astro-ph.GA].

Vanzella, E., F. Calura, M. Meneghetti, M. Castellano, G. B. Caminha, A. Mercurio, G. Cupani, P. Rosati, C. Grillo, R. Gilli, M. Mignoli, G. Fiorentino, C. Arcidiacono, M. Lombini, and F. Cortecchia (2019). "Massive star cluster formation under the microscope at z = 6". In: *MNRAS* 483.3, pp. 3618–3635. DOI: 10.1093/mnras/sty3311. arXiv: 1809.02617 [astro-ph.GA].

Portegies Zwart, Simon F., Stephen L. W. McMillan, and Mark Gieles (2010). "Young Massive Star Clusters". In: *ARA&A* 48, pp. 431–493. DOI: 10.1146/annurev-astro-081309-130834. arXiv: 1002.1961 [astro-ph.GA].

Bastian, N., A. Adamo, M. Gieles, E. Silva-Villa, H. J. G. L. M. Lamers, S. S. Larsen, L. J. Smith, I. S. Konstantopoulos, and E. Zackrisson (2012). "Stellar clusters in M83: formation, evolution, disruption and the influence of the environment". In: *MNRAS* 419.3, pp. 2606–2622. DOI: 10.1111/j.1365-2966.2011.19909.x. arXiv: 1109.6015 [astro-ph.CO].

Ryon, J. E., J. S. Gallagher, L. J. Smith, A. Adamo, D. Calzetti, S. N. Bright, M. Cignoni, D. O. Cook, D. A. Dale, B. E. Elmegreen, M. Fumagalli, D. A. Gouliermis, K. Grasha, E. K. Grebel, H. Kim, M. Messa, D. Thilker, and L. Ubeda (2017). "Effective Radii of Young, Massive Star Clusters in Two LEGUS Galaxies". In: *ApJ* 841.2, 92, p. 92. DOI: 10.3847/1538-4357/aa719e. arXiv: 1705.02692 [astro-ph.GA].

Puzia, Thomas H., Maurizio Paolillo, Paul Goudfrooij, Thomas J. Maccarone, Giuseppina Fabbiano, and Lorella Angelini (2014). "Wide-field Hubble Space Telescope Observations of the Globular Cluster System in NGC 1399". In: *ApJ* 786.2, 78, p. 78. DOI: 10.1088/0004-637X/786/2/78. arXiv: 1402.6714 [astro-ph.GA].

Bastian, Nate and Carmela Lardo (2018). "Multiple Stellar Populations in Globular Clusters". In: *ARA&A* 56, pp. 83–136. DOI: 10.1146/annurev-astro-081817-051839. arXiv: 1712.01286 [astro-ph.SR].

Kim, Ji-hoon, Xiangcheng Ma, Michael Y. Grudić, Philip F. Hopkins, Christopher C. Hayward, Andrew Wetzel, Claude-André Faucher-Giguère, Dušan

Kereš, Shea Garrison-Kimmel, and Norman Murray (2018). "Formation of globular cluster candidates in merging proto-galaxies at high redshift: a view from the FIRE cosmological simulations". In: *MNRAS* 474.3, pp. 4232–4244. DOI: 10.1093/mnras/stx2994. arXiv: 1704.02988 [astro-ph.GA].

Terlevich, Elena, David Fernández-Arenas, Roberto Terlevich, Mark Gieles, Ricardo Chávez, and Ana Luisa González-Morán (2018). "From Giant H II regions and H II galaxies to globular clusters and compact dwarf ellipticals". In: *MNRAS* 481.1, pp. 268–276. DOI: 10.1093/mnras/sty2325. arXiv: 1808.07186 [astro-ph.GA].

Coe, Dan, Brett Salmon, Maruša Bradač, Larry D. Bradley, Keren Sharon, Adi Zitrin, Ana Acebron, Catherine Cerny, Nathália Cibirka, Victoria Strait, Rachel Paterno-Mahler, Guillaume Mahler, Roberto J. Avila, Sara Ogaz, Kuang-Han Huang, Debora Pelliccia, Daniel P. Stark, Ramesh Mainali, Pascal A. Oesch, Michele Trenti, Daniela Carrasco, William A. Dawson, Steven A. Rodney, Louis-Gregory Strolger, Adam G. Riess, Christine Jones, Brenda L. Frye, Nicole G. Czakon, Keiichi Umetsu, Benedetta Vulcani, Or Graur, Saurabh W. Jha, Melissa L. Graham, Alberto Molino, Mario Nonino, Jens Hjorth, Jonatan Selsing, Lise Christensen, Shotaro Kikuchihara, Masami Ouchi, Masamune Oguri, Brian Welch, Brian C. Lemaux, Felipe Andrade-Santos, Austin T. Hoag, Traci L. Johnson, Avery Peterson, Matthew Past, Carter Fox, Irene Agulli, Rachael Livermore, Russell E. Ryan, Daniel Lam, Irene Sendra-Server, Sune Toft, Lorenzo Lovisari, and Yuanyuan Su (2019). "RELICS: Reionization Lensing Cluster Survey". In: *ApJ* 884.1, 85, p. 85. DOI: 10.3847/1538-4357/ab412b. arXiv: 1903.02002 [astro-ph.GA].

Salmon, Brett, Dan Coe, Larry Bradley, Marusa Bradač, Victoria Strait, Rachel Paterno-Mahler, Kuang-Han Huang, Pascal A. Oesch, Adi Zitrin, Ana Acebron, Nathália Cibirka, Shotaro Kikuchihara, Masamune Oguri, Gabriel B. Brammer, Keren Sharon, Michele Trenti, Roberto J. Avila, Sara Ogaz, Felipe Andrade-Santos, Daniela Carrasco, Catherine Cerny, William Dawson, Brenda L. Frye, Austin Hoag, Christine Jones, Ramesh Mainali, Masami Ouchi, Steven A. Rodney, Daniel Stark, and Keiichi Umetsu (2018). "RELICS: A Candidate z $\sim$ 10 Galaxy Strongly Lensed into a Spatially Resolved Arc". In: *ApJL* 864.1, L22, p. L22. DOI: 10.3847/2041-8213/aadc10. arXiv: 1801.03103 [astro-ph.GA].

Williamson, R., B. A. Benson, F. W. High, K. Vanderlinde, P. A. R. Ade, K. A. Aird, K. Andersson, R. Armstrong, M. L. N. Ashby, M. Bautz, G. Bazin, E. Bertin, L. E. Bleem, M. Bonamente, M. Brodwin, J. E. Carlstrom, C. L. Chang, S. C. Chapman, A. Clocchiatti, T. M. Crawford, A. T. Crites, T. de

Haan, S. Desai, M. A. Dobbs, J. P. Dudley, G. G. Fazio, R. J. Foley, W. R. Forman, G. Garmire, E. M. George, M. D. Gladders, A. H. Gonzalez, N. W. Halverson, G. P. Holder, W. L. Holzapfel, S. Hoover, J. D. Hrubes, C. Jones, M. Joy, R. Keisler, L. Knox, A. T. Lee, E. M. Leitch, M. Lueker, D. Luong-Van, D. P. Marrone, J. J. McMahon, J. Mehl, S. S. Meyer, J. J. Mohr, T. E. Montroy, S. S. Murray, S. Padin, T. Plagge, C. Pryke, C. L. Reichardt, A. Rest, J. Ruel, J. E. Ruhl, B. R. Saliwanchik, A. Saro, K. K. Schaffer, L. Shaw, E. Shirokoff, J. Song, H. G. Spieler, B. Stalder, S. A. Stanford, Z. Staniszewski, A. A. Stark, K. Story, C. W. Stubbs, J. D. Vieira, A. Vikhlinin, and A. Zenteno (2011). "A Sunyaev-Zel'dovich-selected Sample of the Most Massive Galaxy Clusters in the 2500 deg^2 South Pole Telescope Survey". In: *ApJ* 738.2, 139, p. 139. DOI: 10.1088/0004-637X/738/2/139. arXiv: 1101.1290 [astro-ph.CO].

Planck Collaboration et al. (2011). "Planck early results. XXVI. Detection with Planck and confirmation by XMM-Newton of PLCK G266.6-27.3, an exceptionally X-ray luminous and massive galaxy cluster at z $\sim$1". In: *A&A* 536, A26, A26. DOI: 10.1051/0004-6361/201117430. arXiv: 1106.1376 [astro-ph.CO].

Ebeling, H., A. C. Edge, and J. P. Henry (2001). "MACS: A Quest for the Most Massive Galaxy Clusters in the Universe". In: *ApJ* 553.2, pp. 668–676. DOI: 10.1086/320958. arXiv: astro-ph/0009101 [astro-ph].

Planck Collaboration et al. (2016). "Planck 2015 results. XXVII. The second Planck catalogue of Sunyaev-Zeldovich sources". In: *A&A* 594, A27, A27. DOI: 10.1051/0004-6361/201525823. arXiv: 1502.01598 [astro-ph.CO].

Salmon, Brett, Dan Coe, Larry Bradley, Rychard Bouwens, Marusa Bradač, Kuang-Han Huang, Pascal A. Oesch, Daniel Stark, Keren Sharon, Michele Trenti, Roberto J. Avila, Sara Ogaz, Felipe Andrade-Santos, Daniela Carrasco, Catherine Cerny, William Dawson, Brenda L. Frye, Austin Hoag, Traci Lin Johnson, Christine Jones, Daniel Lam, Lorenzo Lovisari, Ramesh Mainali, Matt Past, Rachel Paterno-Mahler, Avery Peterson, Adam G. Riess, Steven A. Rodney, Russel E. Ryan, Irene Sendra-Server, Victoria Strait, Louis-Gregory Strolger, Keiichi Umetsu, Benedetta Vulcani, and Adi Zitrin (2020). "RELICS: The Reionization Lensing Cluster Survey and the Brightest High-z Galaxies". In: *ApJ* 889.2, 189, p. 189. DOI: 10.3847/1538-4357/ab5a8b. arXiv: 1710.08930 [astro-ph.GA].

Wen, Z. L., J. L. Han, and F. S. Liu (2012). "A Catalog of 132,684 Clusters of Galaxies Identified from Sloan Digital Sky Survey III". In: *ApJS* 199.2, 34, p. 34. DOI: 10.1088/0067-0049/199/2/34. arXiv: 1202.6424 [astro-ph.CO].

Wen, Z. L. and J. L. Han (2015). "Calibration of the Optical Mass Proxy for Clusters of Galaxies and an Update of the WHL12 Cluster Catalog". In: *ApJ* 807.2, 178, p. 178. DOI: 10.1088/0004-637X/807/2/178. arXiv: 1506.04503 [astro-ph.GA].

Bertin, E. and S. Arnouts (1996). "SExtractor: Software for source extraction." In: *A&AS* 117, pp. 393–404. DOI: 10.1051/aas:1996164.

Benítez, Narciso (2000). "Bayesian Photometric Redshift Estimation". In: *ApJ* 536.2, pp. 571–583. DOI: 10.1086/308947. arXiv: astro-ph/9811189 [astro-ph].

Coe, Dan, Narciso Benítez, Sebastián F. Sánchez, Myungkook Jee, Rychard Bouwens, and Holland Ford (2006). "Galaxies in the Hubble Ultra Deep Field. I. Detection, Multiband Photometry, Photometric Redshifts, and Morphology". In: *AJ* 132.2, pp. 926–959. DOI: 10.1086/505530. arXiv: astro-ph/0605262 [astro-ph].

Strait, Victoria, Maruša Bradač, Dan Coe, Larry Bradley, Brett Salmon, Brian C. Lemaux, Kuang-Han Huang, Adi Zitrin, Keren Sharon, Ana Acebron, Felipe Andrade-Santos, Roberto J. Avila, Brenda L. Frye, Austin Hoag, Guillaume Mahler, Mario Nonino, Sara Ogaz, Masamune Oguri, Masami Ouchi, Rachel Paterno-Mahler, and Debora Pelliccia (2020). "Stellar Properties of $z \gtrsim 8$ Galaxies in the Reionization Lensing Cluster Survey". In: *ApJ* 888.2, 124, p. 124. DOI: 10.3847/1538-4357/ab5daf. arXiv: 1905.09295 [astro-ph.GA].

Strait, Victoria, Maruša Bradač, Dan Coe, Brian C. Lemaux, Adam C. Carnall, Larry Bradley, Debora Pelliccia, Keren Sharon, Adi Zitrin, Ana Acebron, Chloe Neufeld, Felipe Andrade-Santos, Roberto J. Avila, Brenda L. Frye, Guillaume Mahler, Mario Nonino, Sara Ogaz, Masamune Oguri, Masami Ouchi, Rachel Paterno-Mahler, Daniel P. Stark, Ramesh Mainali, Pascal A. Oesch, Michele Trenti, Daniela Carrasco, William A. Dawson, Christine Jones, Keiichi Umetsu, and Benedetta Vulcani (2021). "RELICS: Properties of $z \geq 5.5$ Galaxies Inferred from Spitzer and Hubble Imaging, Including A Candidate $z \sim 6.8$ Strong [O III] emitter". In: *ApJ* 910.2, 135, p. 135. DOI: 10.3847/1538-4357/abe533. arXiv: 2009.00020 [astro-ph.GA].

Jullo, E., J. P. Kneib, M. Limousin, Á. Elíasdóttir, P. J. Marshall, and T. Verdugo (2007). "A Bayesian approach to strong lensing modelling of galaxy clusters". In: *New Journal of Physics* 9.12, p. 447. DOI: 10.1088/1367-2630/9/12/447. arXiv: 0706.0048 [astro-ph].

Jullo, E. and J. P. Kneib (2009). "Multiscale cluster lens mass mapping - I. Strong lensing modelling". In: *MNRAS* 395.3, pp. 1319–1332. DOI: 10.1111/j.1365-2966.2009.14654.x. arXiv: 0901.3792 [astro-ph.CO].

Broadhurst, Tom, Narciso Benítez, Dan Coe, Keren Sharon, Kerry Zekser, Rick White, Holland Ford, Rychard Bouwens, John Blakeslee, Marc Clampin, Nick Cross, Marijn Franx, Brenda Frye, George Hartig, Garth Illingworth, Leopoldo Infante, Felipe Menanteau, Gerhardt Meurer, Marc Postman, D. R. Ardila, F. Bartko, R. A. Brown, C. J. Burrows, E. S. Cheng, P. D. Feldman, D. A. Golimowski, T. Goto, C. Gronwall, D. Herranz, B. Holden, N. Homeier, J. E. Krist, M. P. Lesser, A. R. Martel, G. K. Miley, P. Rosati, M. Sirianni, W. B. Sparks, S. Steindling, H. D. Tran, Z. I. Tsvetanov, and W. Zheng (2005). "Strong-Lensing Analysis of A1689 from Deep Advanced Camera Images". In: *ApJ* 621.1, pp. 53–88. DOI: 10.1086/426494. arXiv: astro-ph/0409132 [astro-ph].

Zitrin, Adi, Tom Broadhurst, Keiichi Umetsu, Dan Coe, Narciso Benítez, Begoña Ascaso, Larry Bradley, Holland Ford, James Jee, Elinor Medezinski, Yoel Rephaeli, and Wei Zheng (2009). "New multiply-lensed galaxies identified in ACS/NIC3 observations of Cl0024+1654 using an improved mass model". In: *MNRAS* 396.4, pp. 1985–2002. DOI: 10.1111/j.1365-2966.2009.14899.x. arXiv: 0902.3971 [astro-ph.CO].

Zitrin, Adi, Agnese Fabris, Julian Merten, Peter Melchior, Massimo Meneghetti, Anton Koekemoer, Dan Coe, Matteo Maturi, Matthias Bartelmann, Marc Postman, Keiichi Umetsu, Gregor Seidel, Irene Sendra, Tom Broadhurst, Italo Balestra, Andrea Biviano, Claudio Grillo, Amata Mercurio, Mario Nonino, Piero Rosati, Larry Bradley, Mauricio Carrasco, Megan Donahue, Holland Ford, Brenda L. Frye, and John Moustakas (2015). "Hubble Space Telescope Combined Strong and Weak Lensing Analysis of the CLASH Sample: Mass and Magnification Models and Systematic Uncertainties". In: *ApJ* 801.1, 44, p. 44. DOI: 10.1088/0004-637X/801/1/44. arXiv: 1411.1414 [astro-ph.CO].

Oguri, Masamune (2010). "The Mass Distribution of SDSS J1004+4112 Revisited". In: *PASJ* 62, p. 1017. DOI: 10.1093/pasj/62.4.1017. arXiv: 1005.3103 [astro-ph.CO].

Diego, J. M., P. Protopapas, H. B. Sandvik, and M. Tegmark (2005). "Non-parametric inversion of strong lensing systems". In: *MNRAS* 360.2, pp. 477–491. DOI: 10.1111/j.1365-2966.2005.09021.x. arXiv: astro-ph/0408418 [astro-ph].

Diego, J. M., M. Tegmark, P. Protopapas, and H. B. Sandvik (2007). "Combined reconstruction of weak and strong lensing data with WSLAP". In: *MNRAS* 375.3, pp. 958–970. DOI: 10.1111/j.1365-2966.2007.11380.x. arXiv: astro-ph/0509103 [astro-ph].

Acebron, Ana, Nathália Cibirka, Adi Zitrin, Dan Coe, Irene Agulli, Keren Sharon, Maruša Bradač, Brenda Frye, Rachael C. Livermore, Guillaume Mahler, Brett Salmon, Keiichi Umetsu, Larry Bradley, Felipe Andrade-Santos, Roberto Avila, Daniela Carrasco, Catherine Cerny, Nicole G. Czakon, William A. Dawson, Austin T. Hoag, Kuang-Han Huang, Traci L. Johnson, Christine Jones, Shotaro Kikuchihara, Daniel Lam, Lorenzo Lovisari, Ramesh Mainali, Pascal A. Oesch, Sara Ogaz, Masami Ouchi, Matthew Past, Rachel Paterno-Mahler, Avery Peterson, Russell E. Ryan, Irene Sendra-Server, Daniel P. Stark, Victoria Strait, Sune Toft, Michele Trenti, and Benedetta Vulcani (2018). "RELICS: Strong-lensing Analysis of the Massive Clusters MACS J0308.9+2645 and PLCK G171.9-40.7". In: *ApJ* 858.1, 42, p. 42. DOI: 10.3847/1538-4357/aabe29. arXiv: 1803.00560 [astro-ph.CO].

Paterno-Mahler, Rachel, Keren Sharon, Dan Coe, Guillaume Mahler, Catherine Cerny, Traci L. Johnson, Tim Schrabback, Felipe Andrade-Santos, Roberto J. Avila, Maruša Bradač, Larry D. Bradley, Daniela Carrasco, Nicole G. Czakon, William A. Dawson, Brenda L. Frye, Austin T. Hoag, Kuang-Han Huang, Christine Jones, Daniel Lam, Rachael Livermore, Lorenzo Lovisari, Ramesh Mainali, Pascal A. Oesch, Sara Ogaz, Matthew Past, Avery Peterson, Russell E. Ryan, Brett Salmon, Irene Sendra-Server, Daniel P. Stark, Keiichi Umetsu, Benedetta Vulcani, and Adi Zitrin (2018). "RELICS: A Strong Lens Model for SPT-CLJ0615-5746, a z = 0.972 Cluster". In: *ApJ* 863.2, 154, p. 154. DOI: 10.3847/1538-4357/aad239. arXiv: 1805.09834 [astro-ph.GA].

Johnson, Traci L., Keren Sharon, Michael D. Gladders, Jane R. Rigby, Matthew B. Bayliss, Eva Wuyts, Katherine E. Whitaker, Michael Florian, and Katherine T. Murray (2017b). "Star Formation at z = 2.481 in the Lensed Galaxy SDSS J1110 = 6459. I. Lens Modeling and Source Reconstruction". In: *ApJ* 843.2, 78, p. 78. DOI: 10.3847/1538-4357/aa7756. arXiv: 1707.00707 [astro-ph.GA].

Foreman-Mackey, Daniel, David W. Hogg, Dustin Lang, and Jonathan Goodman (2013). "emcee: The MCMC Hammer". In: *PASP* 125.925, p. 306. DOI: 10.1086/670067. arXiv: 1202.3665 [astro-ph.IM].

Madau, Piero and Mark Dickinson (2014a). "Cosmic Star-Formation History". In: *ARA&A* 52, pp. 415–486. DOI: 10.1146/annurev-astro-081811-125615. arXiv: 1403.0007 [astro-ph.CO].

Rigby, J. R., T. L. Johnson, K. Sharon, K. Whitaker, M. D. Gladders, M. Florian, J. Lotz, M. Bayliss, and E. Wuyts (2017). "Star Formation at z = 2.481 in the Lensed Galaxy SDSS J1110+6459. II. What is Missed at the Normal Resolution of the Hubble Space Telescope?" In: *ApJ* 843.2, 79, p. 79. DOI: 10.3847/1538-4357/aa775e. arXiv: 1707.00704 [astro-ph.GA].

Carnall, A. C., R. J. McLure, J. S. Dunlop, and R. Davé (2018). "Inferring the star formation histories of massive quiescent galaxies with BAGPIPES: evidence for multiple quenching mechanisms". In: *MNRAS* 480.4, pp. 4379–4401. DOI: 10.1093/mnras/sty2169. arXiv: 1712.04452 [astro-ph.GA].

Bruzual, G. and S. Charlot (2003). "Stellar population synthesis at the resolution of 2003". In: *MNRAS* 344.4, pp. 1000–1028. DOI: 10.1046/j.1365-8711.2003.06897.x. arXiv: astro-ph/0309134 [astro-ph].

Ferland, G. J., M. Chatzikos, F. Guzmán, M. L. Lykins, P. A. M. van Hoof, R. J. R. Williams, N. P. Abel, N. R. Badnell, F. P. Keenan, R. L. Porter, and P. C. Stancil (2017). "The 2017 Release Cloudy". In: *RMxAA* 53, pp. 385–438. arXiv: 1705.10877 [astro-ph.GA].

Calzetti, Daniela, Lee Armus, Ralph C. Bohlin, Anne L. Kinney, Jan Koornneef, and Thaisa Storchi-Bergmann (2000). "The Dust Content and Opacity of Actively Star-forming Galaxies". In: *ApJ* 533.2, pp. 682–695. DOI: 10.1086/308692. arXiv: astro-ph/9911459 [astro-ph].

Vanzella, E., G. B. Caminha, P. Rosati, A. Mercurio, M. Castellano, M. Meneghetti, C. Grillo, E. Sani, P. Bergamini, F. Calura, K. Caputi, S. Cristiani, G. Cupani, A. Fontana, R. Gilli, A. Grazian, M. Gronke, M. Mignoli, M. Nonino, L. Pentericci, P. Tozzi, T. Treu, I. Balestra, and M. Dijkstra (2021). "The MUSE Deep Lensed Field on the Hubble Frontier Field MACS J0416. Star-forming complexes at cosmological distances". In: *A&A* 646, A57, A57. DOI: 10.1051/0004-6361/202039466. arXiv: 2009.08458 [astro-ph.GA].

Vanzella, E., M. Giavalisco, M. Dickinson, S. Cristiani, M. Nonino, H. Kuntschner, P. Popesso, P. Rosati, A. Renzini, D. Stern, C. Cesarsky, H. C. Ferguson, and R. A. E. Fosbury (2009). "Spectroscopic Observations of Lyman Break Galaxies at Redshifts ~4, 5, and 6 in the Goods-South Field". In: *ApJ* 695.2, pp. 1163–1182. DOI: 10.1088/0004-637X/695/2/1163. arXiv: 0901.4364 [astro-ph.CO].

Giavalisco, M., H. C. Ferguson, A. M. Koekemoer, M. Dickinson, D. M. Alexander, F. E. Bauer, J. Bergeron, C. Biagetti, W. N. Brandt, S. Casertano, C. Cesarsky, E. Chatzichristou, C. Conselice, S. Cristiani, L. Da Costa, T. Dahlen, D. de Mello, P. Eisenhardt, T. Erben, S. M. Fall, C. Fassnacht, R. Fosbury, A. Fruchter, J. P. Gardner, N. Grogin, R. N. Hook, A. E. Hornschemeier, R. Idzi, S. Jogee, C. Kretchmer, V. Laidler, K. S. Lee, M. Livio, R. Lucas, P. Madau, B. Mobasher, L. A. Moustakas, M. Nonino, P. Padovani, C. Papovich, Y. Park, S. Ravindranath, A. Renzini, M. Richardson, A. Riess, P. Rosati, M. Schirmer, E. Schreier, R. S. Somerville, H. Spinrad, D. Stern, M. Stiavelli, L. Strolger, C. M. Urry, B. Vandame, R. Williams, and C. Wolf (2004). "The Great Observatories Origins Deep Survey: Initial Results from Optical and Near-Infrared Imaging". In: *ApJL* 600.2, pp. L93–L98. DOI: 10.1086/379232. arXiv: astro-ph/0309105 [astro-ph].

Vanzella, E., M. Meneghetti, G. B. Caminha, M. Castellano, F. Calura, P. Rosati, C. Grillo, M. Dijkstra, M. Gronke, E. Sani, A. Mercurio, P. Tozzi, M. Nonino, S. Cristiani, M. Mignoli, L. Pentericci, R. Gilli, T. Treu, K. Caputi, G. Cupani, A. Fontana, A. Grazian, and I. Balestra (2020). "Candidate Population III stellar complex at z = 6.629 in the MUSE Deep Lensed Field". In: *MNRAS* 494.1, pp. L81–L85. DOI: 10.1093/mnrasl/slaa041. arXiv: 2001.03619 [astro-ph.GA].

Gieles, Mark and Simon F. Portegies Zwart (2011). "The distinction between star clusters and associations". In: *MNRAS* 410.1, pp. L6–L7. DOI: 10.1111/j.1745-3933.2010.00967.x. arXiv: 1010.1720 [astro-ph.GA].

Madau, Piero and Mark Dickinson (2014b). "Cosmic Star-Formation History". In: *ARA&A* 52, pp. 415–486. DOI: 10.1146/annurev-astro-081811-125615. arXiv: 1403.0007 [astro-ph.CO].

Kennicutt Robert C., Jr. (1998). "The Global Schmidt Law in Star-forming Galaxies". In: *ApJ* 498.2, pp. 541–552. DOI: 10.1086/305588. arXiv: astro-ph/9712213 [astro-ph].

Crocker, Roland M., Mark R. Krumholz, Todd A. Thompson, and Julie Clutterbuck (2018). "The maximum flux of star-forming galaxies". In: *MNRAS* 478.1, pp. 81–94. DOI: 10.1093/mnras/sty989. arXiv: 1802.03117 [astro-ph.GA].

Adamo, A., J. E. Ryon, M. Messa, H. Kim, K. Grasha, D. O. Cook, D. Calzetti, J. C. Lee, B. C. Whitmore, B. G. Elmegreen, L. Ubeda, L. J. Smith, S. N. Bright, A. Runnholm, J. E. Andrews, M. Fumagalli, D. A. Gouliermis, L. Kahre, P. Nair, D. Thilker, R. Walterbos, A. Wofford, A. Aloisi, G. Ashworth, T. M. Brown, R. Chandar, C. Christian, M. Cignoni, G. C. Clayton, D. A. Dale,

S. E. de Mink, C. Dobbs, D. M. Elmegreen, A. S. Evans, III Gallagher J. S., E. K. Grebel, A. Herrero, D. A. Hunter, K. E. Johnson, R. C. Kennicutt, M. R. Krumholz, D. Lennon, K. Levay, C. Martin, A. Nota, G. Östlin, A. Pellerin, J. Prieto, M. W. Regan, E. Sabbi, E. Sacchi, D. Schaerer, D. Schiminovich, F. Shabani, M. Tosi, S. D. Van Dyk, and E. Zackrisson (2017). "Legacy ExtraGalactic UV Survey with The Hubble Space Telescope: Stellar Cluster Catalogs and First Insights Into Cluster Formation and Evolution in NGC 628". In: *ApJ* 841.2, 131, p. 131. DOI: 10.3847/1538-4357/aa7132. arXiv: 1705.01588 [astro-ph.GA].

da Silva, Robert L., Michele Fumagalli, and Mark Krumholz (2012). "SLUG—Stochastically Lighting Up Galaxies. I. Methods and Validating Tests". In: *ApJ* 745.2, 145, p. 145. DOI: 10.1088/0004-637X/745/2/145. arXiv: 1106.3072 [astro-ph.IM].

da Silva, Robert L., Michele Fumagalli, and Mark R. Krumholz (2014). "SLUG - Stochastically Lighting Up Galaxies - II. Quantifying the effects of stochasticity on star formation rate indicators". In: *MNRAS* 444.4, pp. 3275–3287. DOI: 10.1093/mnras/stu1688. arXiv: 1403.4605 [astro-ph.GA].

Vikaeus, Anton, Erik Zackrisson, and Christian Binggeli (2020). "The impact of star formation sampling effects on the spectra of lensed z > 6 galaxies detectable with JWST". In: *MNRAS* 492.2, pp. 1706–1712. DOI: 10.1093/mnras/stz3523. arXiv: 1912.02201 [astro-ph.GA].

Meng, Xi and Oleg Y. Gnedin (2020). "Origin of giant stellar clumps in high-redshift galaxies". In: *MNRAS* 494.1, pp. 1263–1275. DOI: 10.1093/mnras/staa776. arXiv: 1910.03443 [astro-ph.GA].

Chapter 5

Conclusions and Future Prospects

The work presented herein represents a collection of studies over a broad range of physical scales and times through the evolution of the universe. However, they all seek to answer related questions on the evolution of star formation and the production of ultraviolet photons across cosmic time. I will thus conclude with a summary of the key points of each chapter, and place each into its broader context related to the evolution of star formation and the contribution of various sources to the production of ultraviolet and ionizing photons. Finally, I will discuss ways that future research can continue to examine these topics.

5.1 Star Formation

In the nearby universe, we can examine galaxies on many scales, from the kiloparsec scales of the full galaxy down to individual stars within the Milky Way and our nearest neighbors. In order to establish a complete understanding of the structure of distant galaxies, we need a way to study them across

similarly diverse scales. My research has sought to do just that, examining the smallest visible objects in a collection of distant galaxies. In reaching such small scales, we can more directly compare the ways in which stars are formed in local and distant galaxies.

Generally, distant galaxies appear too small to resolve their smallest substructures. However, massive foreground gravitational lenses can magnify some distant galaxies, enabling detection of these small scale features that would otherwise be missed. I studied three gravitationally lensed galaxies in the distant universe, at redshifts of $6 \lesssim z \lesssim 10$. I found that these highly magnified galaxies contain substructures ranging from a few tens of parsecs down to less than three parsecs. These sizes are similar to the smallest star clusters in the local universe (Portegies Zwart, McMillan, and Gieles, 2010), which allows direct comparison between these objects at high redshift and in nearby galaxies. In particular, we evaluated the star formation rates (SFRs) of the clumps in these lensed galaxies and compared to what we find in nearby and low-redshift galaxies. We found that star formation rates may be slightly elevated in our distant galaxy sample compared to similar sized star clusters in low-redshift and local galaxies. However, additional data will be needed to conclusively determine whether the SFRs in these distant star clusters is significantly above that of similarly sized local star clusters. Additionally, we find that the surface density of star formation in our distant star clusters is generally consistent with the densest local star clusters, potentially indicating that these objects are on par with the high-SFR end of local star clusters. Elevated SFRs for a given size of star cluster would imply that star formation is

more efficient and intense in the distant universe.

On even smaller scales, within the Milky Way and its nearest neighbors we can study individual stars. Generally in distant galaxies, this is not possible, as the light from many stars blends together. However, in certain cases, gravitational lensing can reveal individual stars in distant galaxies. Previously, this included galaxies at $z \sim 1 - 1.5$ (Kelly et al., 2018; Rodney et al., 2018; Chen et al., 2019; Kaurov et al., 2019). Within one of the lensed galaxies in my high redshift sample, I found a lensed star at $z \sim 6$. This object allows for detailed study of the composition of a star in a time when the universe looked very different. As previously mentioned, distant galaxies appear to be forming stars more efficiently than nearby galaxies. It is also suggested that these distant galaxies may include a greater number of massive stars than local galaxies, possibly due to a lack of metal enrichment during the early stages of star formation in the universe. The lensed star presented here is likely massive ($M > 50 M_{\odot}$), which would be more likely to be found if high-z galaxies form a larger number of massive stars. However, it is still possible that this massive star could be observed with a stellar population similar to that of the Milky Way. Additional lensed stars will be needed at high-redshift to better constrain this question. The discovery of a lensed star within the first billion years of the universe presents a unique opportunity to directly compare the composition of early generations of stars with that of stars formed later in the history of the universe. Future observations will better constrain the properties of this star, and compare those with the properties of similarly massive stars in the local universe. This comparison will inform our understanding of how stars

form and evolve in the early universe.

Finally, at much larger scales, we have found that galaxy clusters play an important role in quenching star formation in galaxies. However, in some cases, stars can still form within these clusters. Generally, this is observed as star formation in infalling galaxies, or in cool-core clusters where a reservoir of cool gas can power star formation in the BCG. In some cases, stars can still form within the intracluster medium, though this can be hard to detect. In studying the diffuse UV background around galaxy clusters, I found an excess of UV emission. This excess could partially be attributed to ongoing star formation within the intracluster medium. While the study presented could not conclusively determine if star formation is the primary contributor to the UV background excess in clusters, it presents a new detection that can be further explored in future works.

5.2 Ultraviolet Photon Budget

After a period of time where the universe was made up primarily of neutral hydrogen, that gas was ionized by light from the first stars and galaxies. This time, known as the Epoch of Reionization, is thought to have begun with the formation of the first stars ($z \sim 30$) and reached a peak at $z \sim 8$ (Planck Collaboration et al., 2020). Then by $z \sim 6$, around a billion years after the Big Bang, the universe is thought to have become mostly ionized. It is generally thought that starlight from nascent galaxies is the primary contributor to the ionizing radiation that drove the process of reionization, with other sources such as active galactic nuclei (AGN) playing a minor role. However, the

exact mechanism for ionizing photon escape from galaxies remains uncertain. Studies of small star clusters in gravitationally lensed galaxies at $z > 6$ can inform our understanding of how photons travel from the young, massive stars that create them into the intergalactic medium (IGM), where they drive the reionization process.

My work studying these distant lensed galaxies at small scales can help to study the production and escape of ionizing UV photons. While the existing HST data presented here cannot well constrain these questions, future planned observations with JWST will be able to provide answers. The work presented here lays the groundwork for these future observations. With spectra from JWST, we will be able to estimate the amount of ionizing energy that is escaping from the small star clusters present in these galaxies. These future studies can improve our understanding of the reionization process.

Additionally, we know that the universe, once ionized, has yet to recombine into a neutral IGM. Similar to the reionization process, the IGM is kept in an ionized state by UV photons from star forming regions in galaxies and AGN. However, analysis of the metagalactic UV background light has found that these sources alone may not account for all of the diffuse UV light visible in the universe (e.g., Chiang, Ménard, and Schiminovich, 2019). To better understand the sources responsible for the UV background, I investigated galaxy clusters as a possible source. I found a notable excess of diffuse UV radiation in massive galaxy clusters. This excess UV light is likely from low levels of star formation in the cluster galaxies and intracluster light, or from relativistic electrons in the intracluster gas which have been accelerated by shocks from

past merger events. The excess found points to galaxy clusters as a small but notable contributor to UV background radiation in the low-redshift universe.

5.3 Future Prospects

Perhaps the most exciting direction that this research can go in the future is utilization of the newly-launched James Webb Space Telescope. JWST will be able to observe in the infrared, which will open up additional wavelength coverage in the distant universe. This additional range will allow improved constraints on star formation rates and ionizing photon production and escape in these distant galaxies, which will improve our understanding of both how the earliest galaxies formed and how they contributed to reionization. Additionally, JWST will be able to spectroscopically study the lensed star at $z \sim 6$, better constraining its mass and measuring its temperature. Future observations could also begin to constrain the composition of the star, enabling more detailed comparisons with nearby massive stars. Finally, JWST will be able to detect galaxies out to greater redshifts than previous observatories, enabling studies of the first galaxies and potentially detections of the first generation of stars.

I plan to use the wealth of JWST data that will soon be collected to examine galaxies at small scales across cosmic time. Using gravitational lensing, I will continue to study the parsec-scale structures in these distant objects, improving our understanding of the physics governing galaxy formation and evolution. At the highest redshifts, these studies will also improve our understanding of the process of reionization. I will also continue to study

the $z \sim 6$ lensed star with JWST, obtaining a spectrum and confirming its properties. I hope to continue searching for distant lensed stars with both HST and JWST, studying distant stars and comparing them to local stars to better understand the evolution of stars and star formation across the history of our universe.

The future with JWST looks bright, and I am excited to take advantage of this unique observatory in the coming decade.

References

Portegies Zwart, Simon F., Stephen L. W. McMillan, and Mark Gieles (2010). "Young Massive Star Clusters". In: *ARA&A* 48, pp. 431–493. DOI: 10.1146/annurev-astro-081309-130834. arXiv: 1002.1961 [astro-ph.GA].

Kelly, Patrick L., Jose M. Diego, Steven Rodney, Nick Kaiser, Tom Broadhurst, Adi Zitrin, Tommaso Treu, Pablo G. Pérez-González, Takahiro Morishita, Mathilde Jauzac, Jonatan Selsing, Masamune Oguri, Laurent Pueyo, Timothy W. Ross, Alexei V. Filippenko, Nathan Smith, Jens Hjorth, S. Bradley Cenko, Xin Wang, D. Andrew Howell, Johan Richard, Brenda L. Frye, Saurabh W. Jha, Ryan J. Foley, Colin Norman, Marusa Bradac, Weikang Zheng, Gabriel Brammer, Alberto Molino Benito, Antonio Cava, Lise Christensen, Selma E. de Mink, Or Graur, Claudio Grillo, Ryota Kawamata, Jean-Paul Kneib, Thomas Matheson, Curtis McCully, Mario Nonino, Ismael Pérez-Fournon, Adam G. Riess, Piero Rosati, Kasper Borello Schmidt, Keren Sharon, and Benjamin J. Weiner (2018). "Extreme magnification of an individual star at redshift 1.5 by a galaxy-cluster lens". In: *Nature Astronomy* 2, pp. 334–342. DOI: 10.1038/s41550-018-0430-3. arXiv: 1706.10279 [astro-ph.GA].

Rodney, S. A., I. Balestra, M. Bradac, G. Brammer, T. Broadhurst, G. B. Caminha, G. Chirivì, J. M. Diego, A. V. Filippenko, R. J. Foley, O. Graur, C. Grillo, S. Hemmati, J. Hjorth, A. Hoag, M. Jauzac, S. W. Jha, R. Kawamata, P. L. Kelly, C. McCully, B. Mobasher, A. Molino, M. Oguri, J. Richard, A. G. Riess, P. Rosati, K. B. Schmidt, J. Selsing, K. Sharon, L. G. Strolger, S. H. Suyu, T. Treu, B. J. Weiner, L. L. R. Williams, and A. Zitrin (2018). "Two peculiar fast transients in a strongly lensed host galaxy". In: *Nature Astronomy* 2, pp. 324–333. DOI: 10.1038/s41550-018-0405-4. arXiv: 1707.02434 [astro-ph.GA].

Chen, Wenlei, Patrick L. Kelly, Jose M. Diego, Masamune Oguri, Liliya L. R. Williams, Adi Zitrin, Tommaso L. Treu, Nathan Smith, Thomas J. Broadhurst, Nick Kaiser, Ryan J. Foley, Alexei V. Filippenko, Laura Salo, Jens

Hjorth, and Jonatan Selsing (2019). "Searching for Highly Magnified Stars at Cosmological Distances: Discovery of a Redshift 0.94 Blue Supergiant in Archival Images of the Galaxy Cluster MACS J0416.1-2403". In: *ApJ* 881.1, 8, p. 8. DOI: 10.3847/1538-4357/ab297d. arXiv: 1902.05510 [astro-ph.GA].

Kaurov, Alexander A., Liang Dai, Tejaswi Venumadhav, Jordi Miralda-Escudé, and Brenda Frye (2019). "Highly Magnified Stars in Lensing Clusters: New Evidence in a Galaxy Lensed by MACS J0416.1-2403". In: *ApJ* 880.1, 58, p. 58. DOI: 10.3847/1538-4357/ab2888. arXiv: 1902.10090 [astro-ph.GA].

Planck Collaboration et al. (2020). "Planck 2018 results. VI. Cosmological parameters". In: *A&A* 641, A6, A6. DOI: 10.1051/0004-6361/201833910. arXiv: 1807.06209 [astro-ph.CO].

Chiang, Yi-Kuan, Brice Ménard, and David Schiminovich (2019). "Broadband Intensity Tomography: Spectral Tagging of the Cosmic UV Background". In: *ApJ* 877.2, 150, p. 150. DOI: 10.3847/1538-4357/ab1b35. arXiv: 1810.00885 [astro-ph.CO].